**NREL** National Renewable Energy Laboratory

*Innovation for Our Energy Future*

# Studies of Basic Electronic Properties of CdTe-Based Solar Cells and Their Evolution During Processing and Stress

## Final Technical Report
## 16 October 2001—31 August 2005

V.I. Kaydanov and T.R. Ohno
*Colorado School of Mines*
*Golden, Colorado*

# Studies of Basic Electronic Properties of CdTe-Based Solar Cells and Their Evolution During Processing and Stress

## Final Technical Report
## 16 October 2001—31 August 2005

V.I. Kaydanov and T.R. Ohno
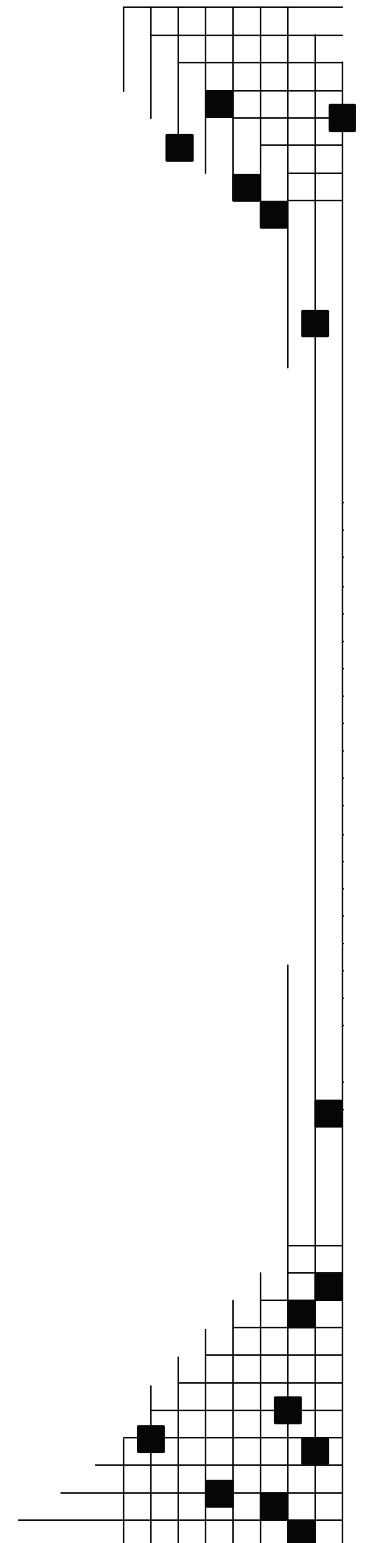*Colorado School of Mines*
*Golden, Colorado*

NREL Technical Monitor: Harin S. Ullal
Prepared under Subcontract No. ADJ-2-30630-05

**PREFACE**

  This project, "Studies of Basic Electronic Properties of CdTe-Based Solar Cells & Their Evolution during Processing & Stressing", which has been performed at the Colorado School of Mines (CSM), is a part of the NREL Thin-Film Partnership Program. There is a lack of knowledge and understanding of basic issues behind the CdTe/CdS cells performance and stability, such as the nature and electronic properties of impurities and defects that control the majority carrier concentration, mechanisms of the dopant compensation, recombination processes, their nature and properties, migration and transformation of defects under various processing, stress, and operating conditions, etc. We believe that better basic understanding of the specific influence of grain boundaries, especially for fine-grain materials like those making up CdTe-based cells, is now one of the most important issues we must address. We need to clarify the role of grain boundaries (GB) in forming the film electronic properties as well as those of the p-n junction. This report presents studies relevant to the problems formulated above that were carried out at CSM during this Project according to the Statement of Work and Tasks of the Subcontract.

  Section 1 presents the results of our studies of electroluminescence (EL) that demonstrate the high sensitivity of EL measurements to the cell processing/composition and stressing conditions. EL obtained in conjunction with photoluminescence (PL) and J-V characterization often showed that nonuniformity in transport through the cell back and front contacts are major sources of nonuniformity in injection level and EL intensity. This concept was confirmed experimentally by the study of cells with intentionally introduced lateral nonuniformity. New equipment allowed high spatial resolution two-dimensional imaging of spectrally integrated EL and PL intensity as well as one-dimensional scans of the spectrally-resolved luminescence. EL and PL images are obtained from the same area of a cell. Comparison of EL and PL spectra and spatial intensity distribution along with the LBIC images of the same cells obtained at CSU, provided new opportunities to study mechanisms of nonuniformity. In particular, luminescence spectra demonstrate several defect-related optical transitions lower than the band gap energy. The spatial distribution of intensity is energy dependent and is effected by nonuniform doping. Electroluminescence studies provided an independent proof of a strong photoconductivity in the CdS layer. They also revealed strong long-lasting (hours to days) changes in the EL pattern after laser irradiation.

  Section 2 presents analysis of admittance spectroscopy (AS) and admittance transient measurements for deep electronic states (DES) detection and studying. Important results were: (a) high concentrations of detected traps in thin film CdTe cells fabricated at different facilities, exceeding the "doping level" commonly determined with C-V profiling; (b) Changes in processing that diminish cell efficiency often are accompanied with reduced trap concentration. We discuss errors of common approaches to AS and DLTS data analysis due to high trap concentration. In particular, trap concentration is underestimated while the doping level derived from C-V measurements can be strongly overestimated. Other problems related to detection and studying deep states, especially very slow states, are discussed along with some new (at least for CdTe) approaches to their solution. A new measurement system was developed that allow us to measure frequency- and bias-dependent admittance in a wide temperature range. In addition, we can make measurements of the long transients (up to tens of hours) at a fixed temperature. We conclude with a brief description of the parameters and options provided by this new

measurement system, the first results of measurements, focused mostly on transients and information on deep/slow states already derived from them.

The methods analyzed in Sec. 2 were applied to studying deep traps and their evolution at various combinations of common processing steps: $CdCl_2$ treatment and doping with Cu. These studies are presented in Sec.3. Rather "fast" traps were detected and studied with AS in the temperature range of -190 $^O$C to above room temperature. "Slow" traps were detected and studied with the capacitance transient measurements. These combined methods revealed traps for majority carrier holes, as well as for minority electrons with activation energy varying form 0.13 eV to ~0.8 eV and apparent capture cross sections varying by four orders of magnitude. It was shown that Cu interstitial defects reduce the $V_{Cd}$ density, but not greatly effect the concentration of the $V_{Cd}$-$Cl_{Te}$ A-centers. The DES with Ea=0.47eV well pronounced in the cells subjected to N-P etch, become undetectable after Cu-doping. The deepest states of E~0.8 eV were detectable and demonstrated a density above $10^{15}cm^{-3}$ only in cells treated both with $CdCl_2$ and Cu. Preliminary, non-systematic stress experiments revealed influence of the treatments on behavior of different states under stress.

Studies of CdTe/ZnTe interface with scanning tunneling microscopy (STM) are presented in Sec.4. We have significantly modified techniques that provided new opportunities in mapping and studying of electrical properties of the back contact. A novel scanning technique, charge injection spectroscopy (CIS) provides detailed maps of carrier transport near the interface. The lateral resolution below 20 nm is about two orders of magnitude below the CdTe grain size. It has been shown that charge transfer between $p^+$-ZnTe and p-CdTe is highly nonuniform, demonstrating large areas with roughly constant high contact resistance coexistent with nanoscale high conductance pathways. A majority of the cell current flows along these pathways, which are often localized at grain boundaries. This may indicate a possible role of grain boundaries as efficient transport channels, at least for the ZnTe:Cu/metal back contact. Conducting paths found within a few of the grains suggest a specific intragrain defect also may cause lowering of the contact resistance.

We have also worked upon further development of the near-field scanning optical microscopy (NSOM) (Sec. 5). High-resolution maps of the photocurrent collection in plan-view were obtained from substrate configuration CdTe/CdS cells prepared by the University of Toledo. Considerable contrast is seen between the grain bulk and grain boundary regions. Photocurrent collection was higher in the intergrain regions than in the grain bulk indicated some possible beneficial effect of grain boundaries on cell performance. In addition to NSOM measurements in the photocurrent mode, the technique of NSOM mapping of photoluminescence (PL) was developed. High spatially resolved PL images were both in plan-view and cross-sectional. The PL pattern in the former obviously correlate with the topography image that allows distinguish the grain boundary and grain bulk regions.

Sec.6 presents results of development and/or improvement of the electrodeposition (ED) and gas jet deposition (GJD systems and CdTe deposition procedures. With a new ED system the CdTe growth rate was increased by an order of magnitude. The GJD technique provided deposition rate up to 20 μm/min, although typically we used a rate of ~ 3-5 μm/min. Comparative studies were performed on the cells grown on different types of single-layer TCO/glass and bi-layer TCO/glass substrates, and also differently $CdCl_2$-treatments. The best results with an efficiency of 12.4% were obtained for Corning glass/bi-layer substrate with increased duration of the $CdCl_2$ treatment. These studies indicated that there is a room for further optimization of processing procedures and significant increase of the cell efficiency.

**TABLE OF CONTENTS**

# LIST OF FIGURES

**LIST OF TABLES**

# 1. SPATIALLY AND SPECTRALLY RESOLVED ELECTRO- AND PHOTO-LUMINECENCE IN CdTe SOLAR CELLS

## 1.1. Introduction

Our previous studies [1] indicated that CdTe/CdS cells emitted light under forward bias in the photon energy range in the vicinity of the CdTe bandgap. Electroluminescence (EL) was observed at room temperature as well as at T~15 K. Though the excitation mechanism is different, EL is similar to the more commonly employed photoluminescence (PL). Instead of optical excitation (PL), excess electron-hole pairs are injected electrically in EL measurements. Their recombination produces luminescence. The intensity of EL emission is roughly proportional to the product of the electron and hole concentrations. If n-CdS is doped heavier than the p-CdTe absorber layer, the $n \times p$ product reaches a maximum in the CdTe near the junction and this is the region where EL originates. Our previous spectral studies of EL are consistent with this analysis [1]. Furthermore, EL spectra have been found to be similar to PL spectra in CdTe [1] and also for many other materials The same was found previously for many other materials such as SrS:Cu and SrS:Ag, Cu, Ga thin films [2], $Si^+$-implanted $SiO_2$ [3], CdS nanocrystals [4], and $Si_{1-x}Ge_x$ alloys [5]. However, few studies of EL in CdTe/CdS cells are known whereas studies of PL are numerous. Our intensive EL studies are not intended to replace PL. The similarity of the spectra observed along with difference in the mechanisms and techniques of excitation, lends further credence to the usefulness of EL and PL as complementary techniques and the ability to use information from one to explain effects in the other.

One inherent property solar cells based on polycrystalline thin films is nonuniformity of the photo-electronic properties in various spatial scales. It is obvious that macro-nonuniformities reduce the efficiency of solar modules. Recently it was shown (Karpov, Shvidka, Compaan, et.al, [6]) that a single micro-nonuniformity, e.g. small area region of reduced open circuit voltage, can significantly affect the performance of the whole cell. Standard characterization techniques such as current-voltage, capacitance-voltage, and quantum efficiency measurements average properties over the area of a solar cell and do not detect micro-nonuniformities. Contrasting these methods is a new wave of spatially resolved characterization tools such as cathodoluminescence (CL) [7], electron beam induced current (EBIC) [8,9], laser beam induced current (LBIC) [10], near-field scanning optical microscopy (NSOM) [11], PL mapping [12], and, finally, the spatially resolved electroluminescence.

There are several advantages making EL attractive as a characterization tool. Though our EL technique does not have the highest spatial resolution among the techniques listed above, the spatial dynamic range of resolved EL data may be the greatest, with a linear resolution of several microns to scans of over a centimeter. Also, unlike other methods that usually involve high injection rates, the minimum degree of excitation required to induce measurable EL could be on the order of $J_{sc}$ or even less. This moderate excitation level increases confidence that the observed EL patterns can be related to cell performance in normal operation. Low injection ensures that characterization will not degrade device performance, as verified by I-V data taken before and after EL imaging. EL gives insight into material quality because recombination centers degrade EL emission and cell efficiency alike. As a final point, EL is technically simple to perform as it can be observed at room temperature, and data acquisition is relatively quick.

Because it is simple to implement, EL may find use as a standard production monitoring tool in an industrial application.

## 1.2 Development and Application of Electroluminescence Imaging

### 1.2.1 Experimental setup and data analysis
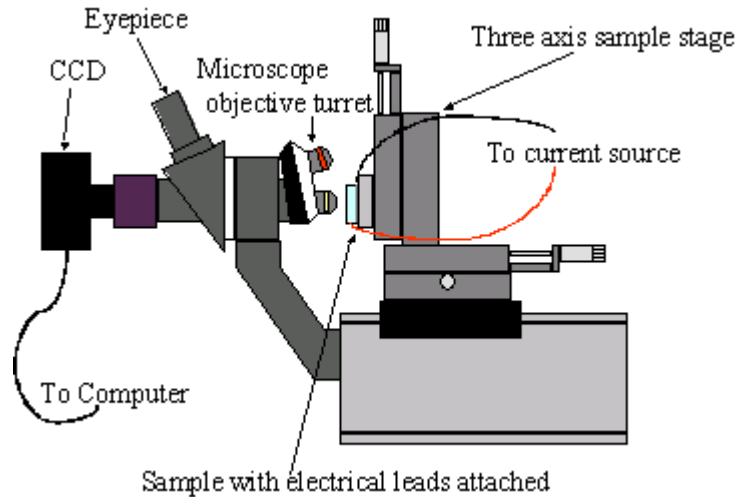


**Figure 1.1.** EL experimental setup.

The main experimental setup used in these studies is shown in Fig. 1.1. Biasing to induce EL was provided by a Keithley 2120 SourceMeter. This device also allowed I-V measurements without removing the cell from the EL apparatus. EL images of cells were acquired with a Santa Barbara Instrument Group ST-5C cooled CCD camera that had a $320 \times 240$ array of 10 by 10 $\mu m^2$ square pixels. The cell was mounted on a micrometer-controlled stage and imaged through either a 1.3x or 10x microscope objective.

The 10x objective allowed for resolution on the order of the optical limit for the infrared EL, namely several microns. The 1.3x lens imaged a $1.6 \times 1.2$ mm$^2$ rectangular area of a cell. Multiple images could then be stitched together graphically to form a composite of the entire cell. Cells to be compared were imaged at constant average current density as noted below, and standard CCD acquisition time is 60 seconds.

For large-area EL measurements of sub-modules, a Sony SSCM183 black and white security camera was employed. The camera had a manually adjustable 3.5-8 mm focal length wide-angle lens. These optics allowed for imaging a large area of the cell with the camera in close proximity. The large solid angle image increased sensitivity of the camera at the expense of some aberration of the image.

Often the EL emission is concentrated in small bright spots. The brightness and the number of spots increases with increasing injection current levels (Fig. 1.2). Irreversible changes in EL were observed with current density in excess of 1A/cm$^2$. Currents below this threshold applied for periods less than an hour did not appear to change the EL images.

$J = 20 \text{ mA/cm}^2$      $J = 90 \text{ mA/cm}^2$      $J = 190 \text{ mA/cm}^2$
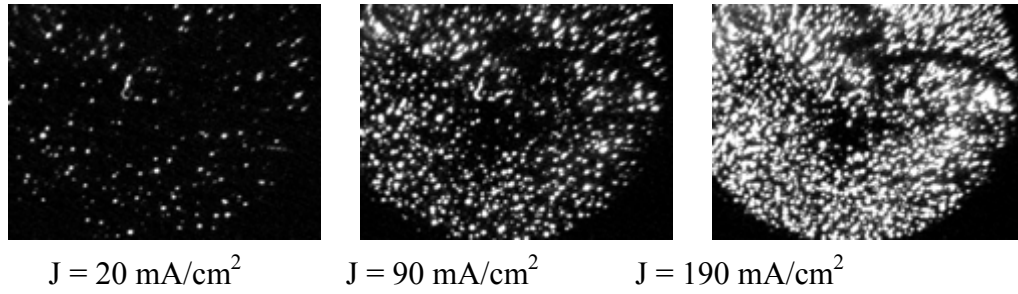
**Fig. 1.2.** EL changes with current

Fig. 1.3 shows stitched EL images of cells from a vapor transport deposition cell (VTD), a University of South Florida cell (USF), and a University of Toledo cell (UT), manufactured with different deposition techniques (vapor transport, close-space sublimation, and sputtering, respectively) and back contacts (proprietary, Ag paste, and Au, respectively).
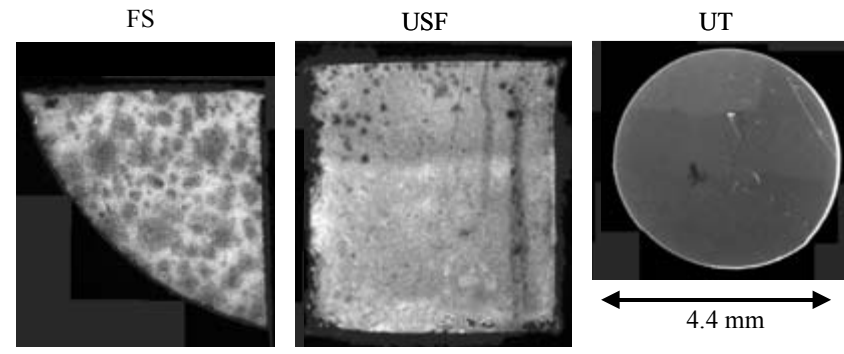


**Figure 1.3** Composite, low magnification EL images. All have the same scale in dimensions but not brightness. Differences in total EL intensity did not exceed ~30 %. Note, the VTD cell was scribed from a circle into a sector to approximate the area of the UT cell while still showing the edge of the original cell. Current density is 33mA/cm$^2$ for all images.

Though mean emission intensity was comparable, pattern and degree of non-uniformity varied greatly from institution to institution. To quantify nonuniformity we introduced a parameter called the "nonuniformity" (NU) and defined it as the standard deviation of EL intensity normalized by mean EL intensity. The calculated NU values for the cells were VTD: 0.22, USF: 0.15, and UT: 0.11.

Comparison of the low-resolution image of the UT cell in Fig.1.3 to the highly magnified image of the same cell in Fig. 1.4 reveals non-uniformity on different scales.
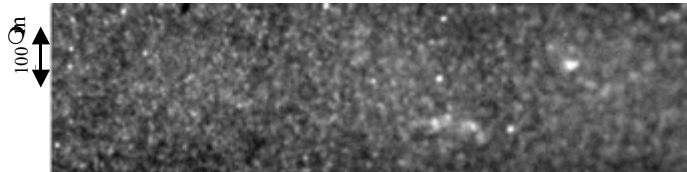


**Figure 1.4.** High magnification image of UT cell shown in Fig. 1.3. Current density is 33 mA/cm$^2$

Selected histograms in Fig.1.5 make differences in EL non-uniformity more visible. Note how the low magnification UT image has the narrowest histogram (indicating that it is the most uniform), whereas the FS histogram is significantly wider. The VTD histogram has a peak with a shoulder, indicating two separate populations.
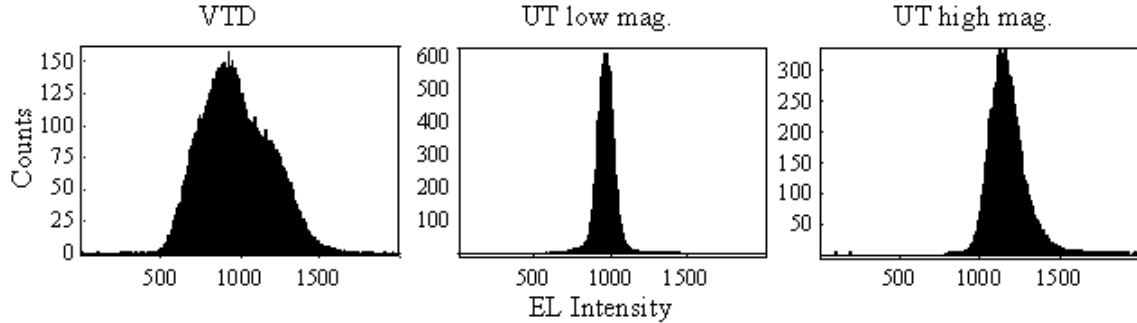


**Figure 1.5.** Selected histograms

The differences between the low- and high-magnification image histograms for the UT cell indicate that there coexist several characteristic non-uniformity spatial scales. To detect and study them we have used variogram analysis which is a geostatistical technique used to quantify the spatial correlation of data [13]. The extent of this spatial correlation helps to quantify the scale and possible anisotropy in the non-uniformity structures underlying electroluminescence. For example, correlation feature sizes of ~10 μm and ~60 μm were found in the UT cells.

## 1.2.2   Influence of processing and stressing on EL intensity and pattern

### *Cadmium chloride treatment*

A study was conducted using cells with VTD material deposited elsewhere whose back contacts (ZnTe:Cu/Au) were processed at CSM. EL from cells that underwent $CdCl_2$ treatment was compared to EL from nominally identical cells without $CdCl_2$ treatment. Both sets of cells showed isolated bright spots less than 20 microns in size with emission between the bright spots that was indistinguishable with the dark counts (Fig. 1.6). With this form of EL emission, which likely resulted from non-ideal back contact processing, non-uniformity was un-quantifiable because of the high contrast. The cells with $CdCl_2$ had more bright spots, and spot intensity was greater. Furthermore, the rate of increase of EL intensity with current was lower in the cells without $CdCl_2$. Drive level capacitance profiling (DLCP) was also used to estimate the deep level density in these cells [14]. It was found that the cells subjected to the $CdCl_2$ treatment possessed more traps than the cells without $CdCl_2$ treatment. This result was unexpected, as a greater trap concentration would imply less luminescent recombination, but is important nonetheless because it proves that effects of $CdCl_2$ treatment (a crucial step for producing efficient CdTe devices) can be observed with EL.
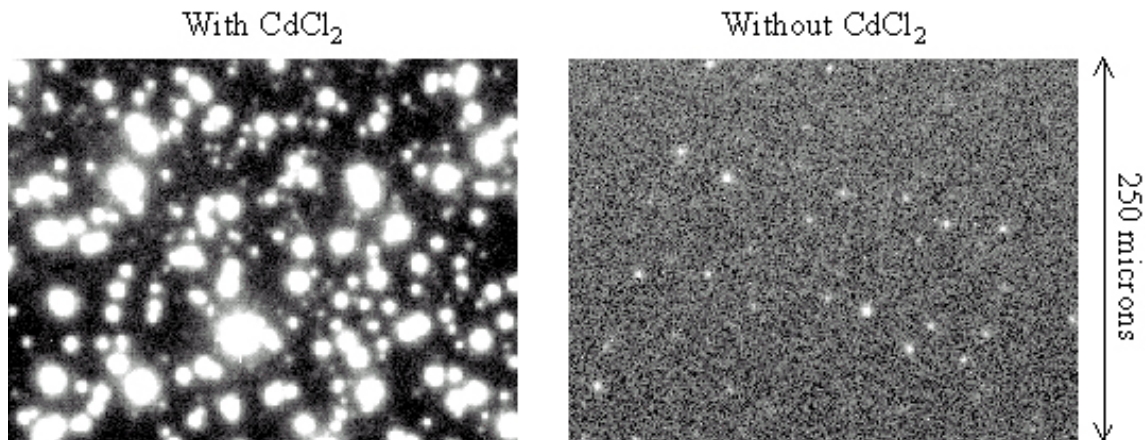
**Figure 1.6.** Effects of CdCl$_2$ treatment on EL. Current density = 50 mA/cm$^2$.

This experiment was later repeated with a set of cells that exhibited a more-uniform EL pattern in order to quantify non-uniformity (Fig. 1.7). Again, the CdCl$_2$ treated cell exhibited greatly enhanced emission with respect to the untreated cell. The untreated cell required an extreme injection rate of 1.5A/cm$^2$ in order to show measurable EL, as compared to a more modest 75 mA/cm$^2$ for the CdCl$_2$ treated cell. The NU was 0.22 for the treated cell and 0.63 for the untreated cell. Though the injection conditions varied greatly, non-uniformity generally decreases with increased injection, thus supporting the conclusion that the CdCl$_2$ improves EL uniformity. Also relevant is the pattern of the non-uniformity in the treated cell. The scale of the features is on the order of hundreds of microns. This pattern likely results from droplets present in a wet CdCl$_2$ treatment.
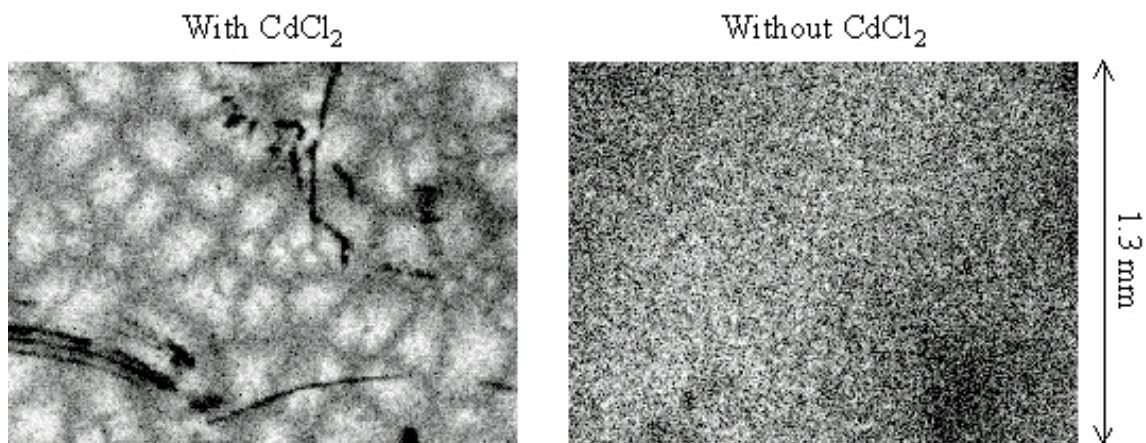


**Figure 1.7.** Effects of CdCl$_2$ treatment on EL II. Current density = 75 mA/cm$^2$ for the CdCl$_2$ treated cell and 1,500 mA/cm$^2$ for the untreated cell.

### *Doping with Cu*

EL in cells from Colorado State University (CSU) was found to be profoundly influenced by the concentration of Cu in the cell (not shown). There was a noticeable change in EL (both in intensity and pattern) due to the presence of Cu. The cells were processed with 0, ~0.75, ~1.5,

and ~6 monolayers (ML) of Cu through vapor deposition. Cell performance improved with increased Cu content. The most brightly emitting cells were those with the 0.75 and 1.5 ML of Cu. These cells also demonstrated the least-uniform EL intensity. Compared to these two processing conditions, 6 ML of Cu lead to a small decrease in emission intensity (less than a factor of 2) as well as an increase in uniformity. The cells with no Cu showed a ~4x decrease in emission intensity and slightly increased uniformity compared to those cells with Cu. Though spectrally resolved EL emission of these cells might yield information on the cause of the observed change in the intensity and non-uniformity with respect to Cu content, EL spectra could not be obtained due to low signal strength.

### *Response to stress*

In general, the observed response of EL to stress has been a dramatic drop in EL intensity with amounts of stress that did not degrade efficiency much at all. Compaan *et al.* have also observed a similar effect with EL and electrically biased PL [15]. This drop in emission intensity is usually accompanied by an increase in non-uniformity. These huge changes suggest that EL can perhaps be used as an early warning system for detecting cells that are likely to degrade quickly.

A more dramatic stress effect has been seen on VTD cells: the change from a mottled, but relatively uniform EL emission pattern to emission coming only from isolated spots (Fig. 1.8). This effect occurred in cells light soaked at open-circuit voltage ($V_{oc}$) for 56 days as well as in cells stressed in light for only 7 days at either $V_{oc}$ or –2 V reverse bias. Comparing I-V curves (not shown), one can see a large series resistance in the light curves as well as a high resistance at forward bias in the dark (the condition in which EL is measured). These high resistances suggest a degraded back contact [16]. Consistent with the high resistance is a model in which the back contact has degraded non-uniformly, such that some small areas still have low resistances through the cell. Since the metallized back contact is an equipotential surface, current would stream through these small areas, inducing EL only in isolated dots. The fact that the dots are mostly round in shape supports this model because current streaming through a microscopically small low resistance region of the back contact would spread in a radial fashion before it reached the main junction, resulting in circular EL emission.
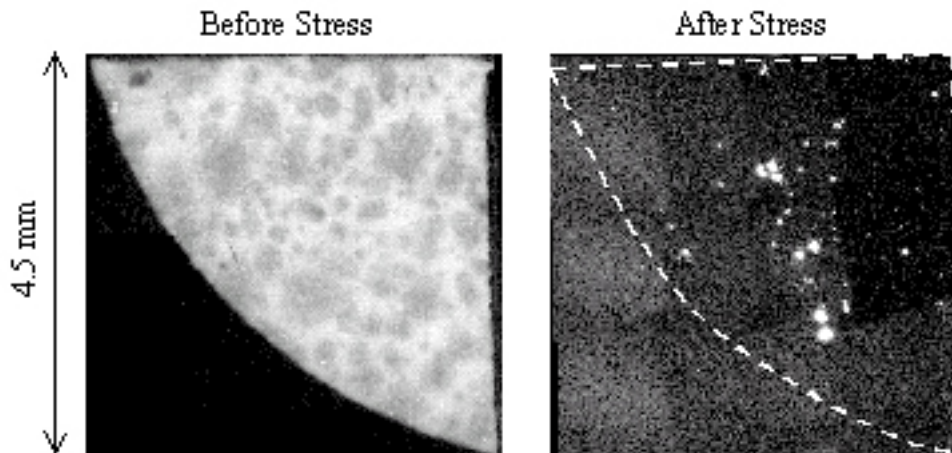


**Figure 1.8.** EL from stressed VTD cell. The dashed line in the stressed image indicates the edges of the cell. Current density = 33 mA/cm$^2$ for both.

***EL measured on the CdTe/CdS sub-module***

EL was also studied on the sub-module scale. Data was taken from CdTe sub-modules made from VTD material produced with a moving substrate. The sub-modules consisted of eight $1 \times 10$ cm$^2$ cells defined by scribes that were connected in series through an integrated process. A total current of 1 A, that corresponds to an average current density of ~125 mA/cm$^2$ per cell, was used to induce EL in these cells. An image is shown in Fig. 1.9. Two features of note exist in the EL image. First, there is a subtle variation in intensity parallel to the direction of the scribe lines. Moving from right to left, the EL changes from brighter to dimmer to brighter again. This variation occurs perpendicular to the direction in which the substrate is moved during deposition and therefore likely results from a systematic non-uniformity in the deposition process.
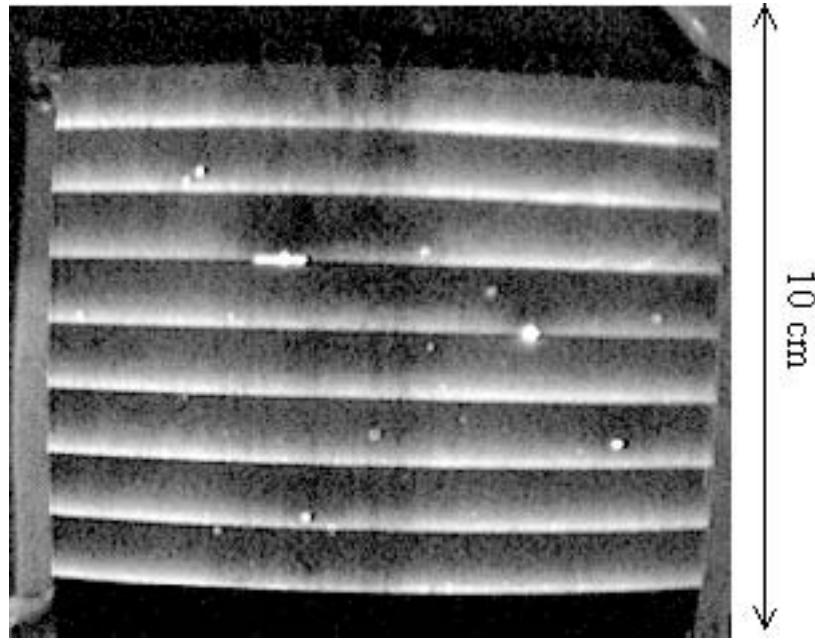


**Figure 1.9.** EL from a CdTe sub-module. Average current density = 125 mA/cm$^2$.

Secondly, the EL is concentrated in bright strips that fade in the direction perpendicular to the scribe lines. This feature dominated the EL emission and resulted from the non-negligible sheet resistance of the TCO front contact. Portions of the cells closest to the forward-biased scribe line exhibited greater EL intensity because they received the greatest current. This hypothesis was confirmed with modeling by using a program [17] that simulated the voltage drops and current through a series of micro-diodes and resistors (representing the main junction of the cell, back contact and TCO distributed resistance). EL intensity has been found to be proportional to current density, which varies between scribes. Fig. 1.10 shows a line-scan taken from the EL image data in comparison to the current flowing through each microdiode in the model. A good qualitative correlation between the model and the EL line scan corroborates the analysis above.
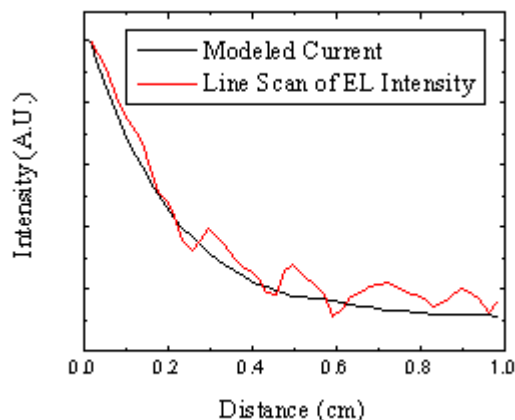
**Figure 1.10**  Line-scan of EL intensity and modeled current for sub-module.

### 1.2.3.  Summary

EL images have been obtained of CdTe solar cells at high (several μm) spatial resolution with low current injection levels (on the order of short-circuit current densities). Non-uniform patterns have been shown to occur at different scales on differently grown cells, suggesting that perhaps different physical models should be used when interpreting the data for different materials. EL is also affected by changes in important processing steps, namely $CdCl_2$ treatment and Cu doping before or along with application of the back contact. Accordingly, EL may be able to help unravel the effects of $CdCl_2$ treatment and may aid in finding how to stop Cu from leaving the back contact. Also, even gently stressed cells have shown drastically affected EL intensity. EL may prove useful in an industrial setting because of its possible ability to predict long-term stability based upon short term stress data. This non-destructive testing technique has met some success with GaP LEDs [18]. Changes in EL in some cells due to stressing imply highly non-uniform back contact degradation. Finally, EL was used to identify non-uniformities resulting specifically from the processing of sub-modules, suggesting that it may aid in scale-up from the laboratory to an industrial setting.

### 1.3.  Effects of Cu Studied with Patterned Doping and Spatially Resolved Luminescence Techniques

The application of Cu to improve CdTe performance, particularly to reduce back contact series resistance ($R_s$), is crucial to obtaining high efficiency devices as shown by its presence in record CdTe solar cells. At the same time, Cu is suspected of having some detrimental effects on stability in CdTe/CdS devices.

The defects Cu can form include Cu substitutions onto a Cd site ($Cu_{Cd}$), Cu interstitials ($Cu_i$), and various complexes with both native and non-native defects formed during processing. Previously, we have tried to isolate Cu effects by fabricating nominally identical devices with and without intentionally adding Cu. However, the interpretation of these experiments is complicated by the fact that Cu is present in most CdTe thin films, even when it is not intentionally added [19]. Furthermore, identically processed cells, even nearest neighbors from the same substrate, suffer from non-uniformity issues [6], resulting in different characteristics,

making it even more difficult to isolate the effects of Cu.  In this study, we avoid many of these problems by creating a well-defined array of Cu doped and undoped regions in a single cell. Spatially resolved electro-optical characterization techniques then allow Cu doped and undoped regions of the exact same cell to be studied.

### 1.3.1.    Experiment

A VTD material was used as the basis for the devices studied. Post-processing and back contact application was conducted at the CSM. The material was first etched for 30 seconds with a 0.015% Br: Methanol solution.  In a standard process, 30 Å of Cu is then evaporated over the entire surface of the substrate. After annealing in nitrogen at 200 °C for 7 minutes, excess Cu was removed with a 30s dip in a 0.005% Br: Methanol solution. Finally, 500 Å of Au is evaporated to complete the back contact. The Au pad, 1.6mm in diameter, defines the cell size.

To introduce a well-defined array of Cu rich regions into a cell for this study, one modification was made. Fig. 1.11 schematically demonstrates deposition of this array. Instead of depositing Cu over the entire back surface of the CdTe, Cu was evaporated through a shadow mask with circular holes ~150 μm in diameter. The result is a cell with an Au back contact and with many circular Cu rich regions (dots) underneath, occupying ~15% of the area of the cell.
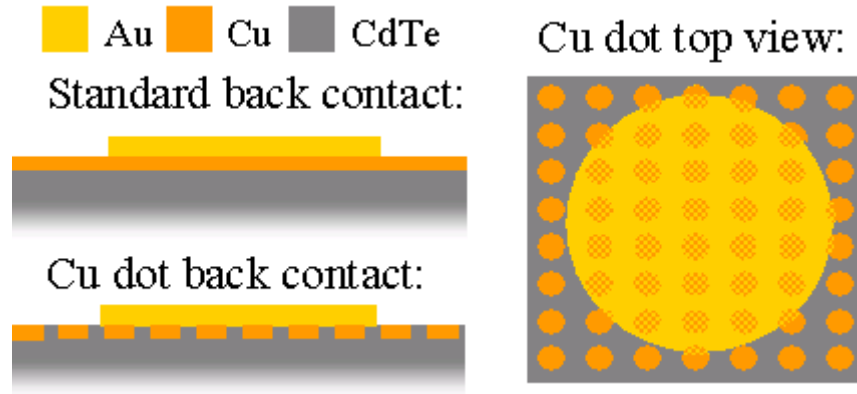


**Figure 1.11**   Schematic representation of patterned Cu doping.

Electroluminescence (EL) and photoluminescence (PL) were employed as probes of material properties. In the case of PL, carriers are injected optically (1.96 eV helium-neon laser was used) and are to first order unaffected by contact properties under the open circuit conditions used here. The absorption coefficient for CdTe for the light used is $\alpha = 4.8 \times 10^4$ cm$^{-1}$. All EL and PL measurements were performed from the glass side of the cell and under the Au back contact except for the lower right corner of the EL images.

To obtain spatial images of EL, the cell was forward-biased to obtain an average current density of 25 mA/cm$^2$ and the resultant EL was focused onto the entrance slit of an Acton 300i spectrometer with a Princeton Instruments Spec-10:100BR liquid nitrogen cooled CCD array detector.  The spectrometer had two gratings and a mirror mounted on a rotating turret.  Using the mirror, and opening the slit to 2 mm, spatial images of EL as in Fig. 1.12 were obtained. For spectral resolution, a grating is rotated into position and the slit width is reduced. The signal that passes through the spectrometer is dispersed onto the CCD detector. Because the detector is a 2-

dimensional array, spectrographic information is obtained along the horizontal axis of the CCD, while spatial information is obtained along the vertical axis. With PL, the laser beam was focused with a cylindrical lens such that the beam was roughly uniform (within a factor of 3) over the area of the cell imaged through the slit. The average laser power was ~20 mW/cm$^2$ (~0.2 suns), similar to normal operating conditions. PL data was normalized to the laser power.
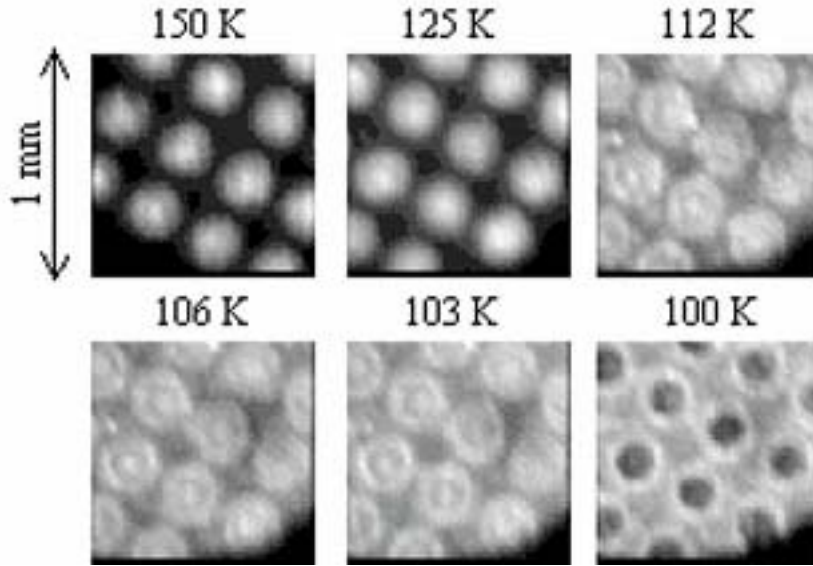


**Figure 1.12** EL Images of Cu dot cell as a function of temperature. Average injection level is 25 mA/cm$^2$.

### 1.3.2. Results and discussion

EL emission correlated well with the location of the Cu dots as shown by the images in Fig. 1.12. From room temperature down to T~100 K, EL intensity was up to an order of magnitude greater on the Cu dots. This result is consistent with Cu reducing the back contact resistance. Below 100 K, the EL pattern inverted, with the intensity from non-Cu (undoped) regions several times that of Cu-doped regions. This inversion occurred within a temperature range of approximately 25 K, as shown in Fig. 1.12. A possible explanation for this inversion involves changes in the nature of the defects responsible for transport. Assuming that Cu incorporates itself primarily as $Cu_{Cd}$ for these processing conditions, Cu regions should contain fewer $V_{Cd}$ defects as Cu occupies the vacant Cd sites. Theoretical work by Wei and Zang places $Cu_{Cd}$ as a deep acceptor at $E_v$ + 0.22 eV, whereas $V_{Cd}$ is shallower at $E_v$ + 0.13 eV [20]. (Numerous experimental studies provided $E(Cu_{Cd}) \approx E_v$+ 0.3 eV see, e.g., [21], but it was pointed out in [20] that the accuracy of calculated levels is ~0.1 eV). As the temperature drops below 100 K, the deeper $Cu_{Cd}$ levels freeze out, creating a higher $R_s$ in Cu doped regions than in undoped regions where shallower defects (such as $V_{Cd}$) are still electrically active. Undoped regions then have the lower $R_s$, draw more current, and therefore show brighter EL emission. Because the signal is greater at lower temperatures, all comparisons between EL and PL were made with the data taken at 70 K. It is important to note that cells processed with a different $CdCl_2$ treatment (namely very high purity $CdCl_2$ with vapor deposition) suppressed the inversion, suggesting that

CdCl$_2$ treatment can affect the defect structure of the material as well (as discussed in Sec. 3). However, inversion was present in all cells used in this study.

The data in Fig. 1.13 were obtained with a slit width of 100 μm and a 300 groove/mm grating resulting in both spatial and spectral information. First, data were integrated over all photon energies to produce the line scans shown. Though EL shows changes in intensity correlated spatially with the Cu dots, integrated PL intensity shows no correlation with Cu. In other words, EL emission is dominated by Cu doping while integrated PL (to lowest order) is unaffected by Cu. Because EL relies upon electrical injection whereas PL uses direct optical injection, one can conclude that Cu greatly affects conduction through the back contact to the main diode. At room temperature Cu increases conduction, while at low temperature Cu suppresses conduction, as discussed above.
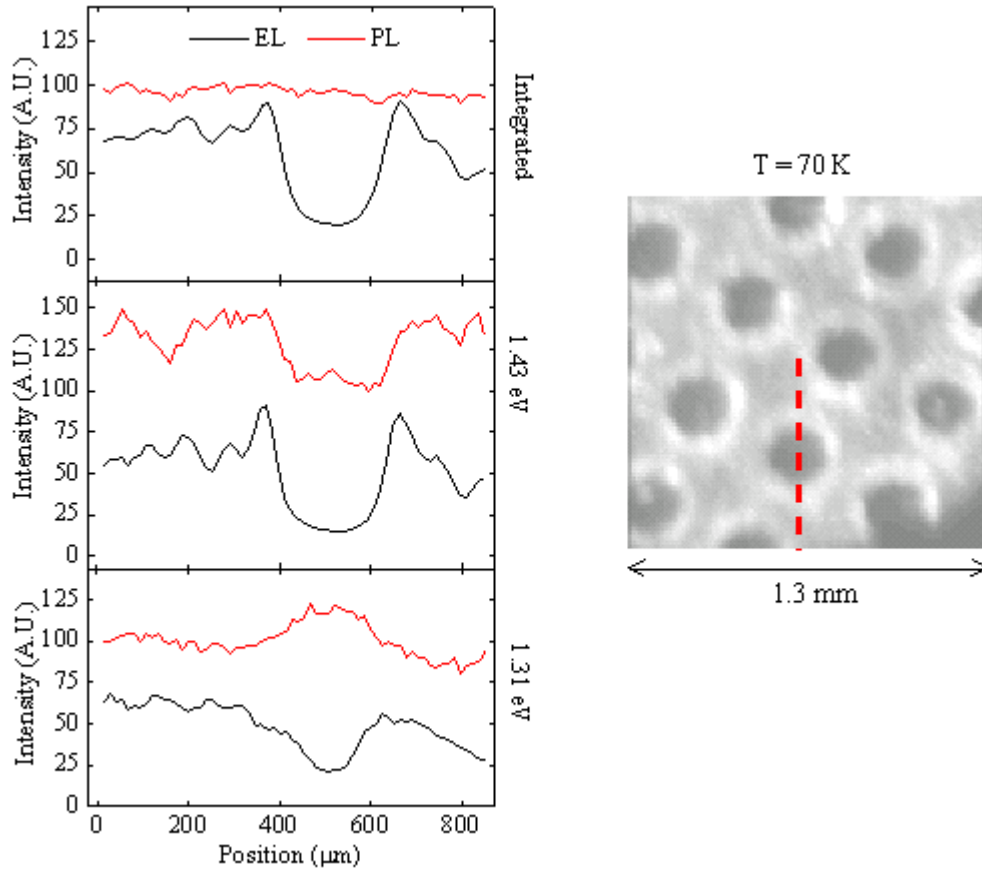


**Figure 1.13.** EL and PL line scans. The scans were taken in the region of the dashed line in T=70 K EL image to the right. The top scans are integrated over photon energy where EL is correlated with the location of Cu whereas PL is not. A line scan taken at 1.43 eV shows EL and PL patterns that are spatially correlated. A line scan taken at 1.31 eV shows EL and PL patterns that are anti-correlated.

When observing line scans from individual energies, one can see an effect of Cu on PL. At 1.43 eV, in the range of a shallow defect possibly related to $V_{Cd}$ ($E_g$ in CdTe is slightly above 1.6eV at this temperature), PL intensity is suppressed in the Cu doped regions, correlating with the EL pattern. Probing a deeper feature at 1.31 eV (possibly related to $Cu_{Cd}$) results in enhanced

PL and suppressed EL over the Cu dot; the PL and EL patterns are anti-correlated. However, the EL is suppressed by the Cu *less* at this energy than at 1.43 eV. This result indicates that the EL pattern is being dominated by transport, but is still influenced by the variations in recombination that cause the enhanced PL signal in the Cu region.

Although emission lines tend to be broad in polycrystalline materials, the spectra presented in Fig. 1.14 show visible structure.
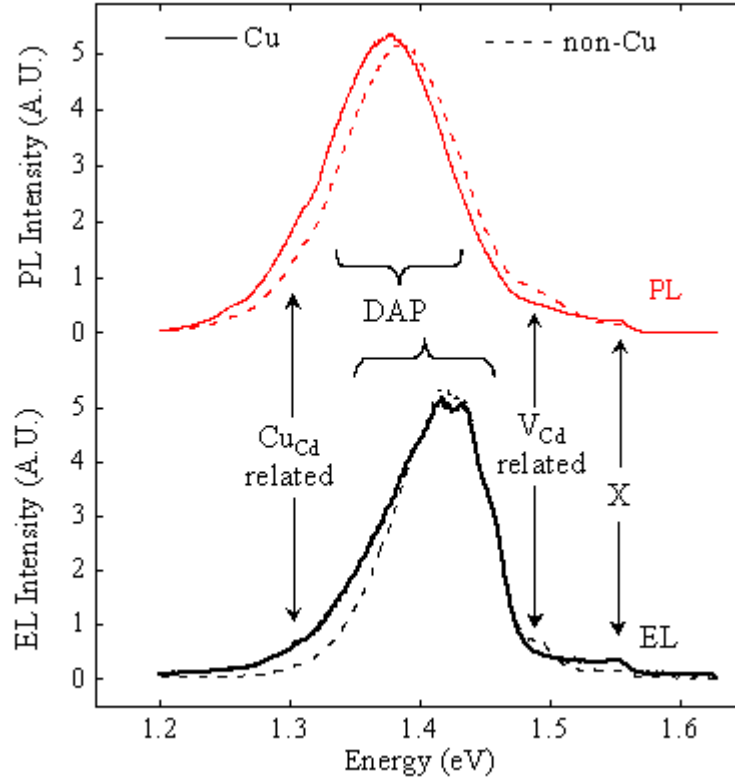


**Figure 1.14.** Spectra from Cu and non-Cu regions. Note separate arbitrary intensity scales for EL and PL. EL intensity from the Cu region was multiplied by 3. PL data is to scale. Features are tentatively identified as band edge excitonic structure (X), Cd vacancy ($V_{Cd}$), donor-acceptor-pair (DAP), and emission related to Cu substitutional defects ($Cu_{Cd}$). Slight differences between Cu regions and non-Cu regions are visible only because of the techniques used here. T = 70 K.

In contrast to the spectrally integrated data above, subtle differences exist in PL between Cu doped and undoped regions. These features are similar in EL and PL and are tentatively identified in the figure based on prior studies, noting that their attribution is not unambiguous. Excitonic structure (X) is observed near the band-edge. The most intense feature is a donor-acceptor pair (DAP) band that has been widely reported in other studies [7, 22, 23]. Both these features exist in spectra taken from both Cu and non-Cu (undoped) regions. The Cu regions of the cell show increased low-energy emission (towards 1.3 eV) in the donor-acceptor pairs (DAP) band, labeled as $Cu_{Cd}$ related.[7, 23]. The presence of some Cu related emission from the undoped region of the cell is not unexpected due to Cu impurities in the CdTe source material and CdCl$_2$ treatment. Comparison of the spectral region above the DAP band shows more PL near 1.5 eV in the undoped regions, labeled as $V_{Cd}$ related [23]. These small but real differences

between the Cu and non-Cu spectra could only be confidently identified using the Cu dot technique along with spatially resolved characterization methods. Seemingly, the presence of Cu affects the concentration of another defect (such as $V_{Cd}$ or related complex) in order to incorporate itself into the lattice (as opposed to $Cu_i$, which does not involve replacing another defect), agreeing with the identification of the deep and shallow features as $Cu_{Cd}$ and $V_{Cd}$ related, respectively.

### 1.3.3 Summary

By Cu doping CdTe cells in a patterned array, we were able to confirm through a combination of spatially resolved EL and PL measurements that Cu improves performance at least partially by increasing carrier injection (lowering $R_s$) through the back of the cell. The EL pattern was found to invert at low temperature suggesting that the presence of Cu must modify another defect in the material that is responsible for transport. Also, our technique allowed us to detect subtle differences in PL and EL spectra between Cu doped and non-Cu doped regions. The spectral differences along with the EL inversion at low temperature suggest that, for this process, electrically active Cu incorporates itself into the lattice in the form of $Cu_{Cd}$, displacing $V_{Cd}$ or a related complex.

### 1.4. Expanded Experimental Space for Luminescence Studies

In this section, we measure EL and PL with simultaneous spatial and spectral resolution. We utilize a large range of experimental variation including injection level, temperature, bias (light for EL, electrical for PL), and laser energy for PL.

The electrical injection of excess carriers makes EL very sensitive to the electron transport specifics of the material whereas PL induced by direct optical injection is less sensitive to electrical transport. Combining of the two allows one to isolate effects due to transport. In order to observe EL, one needs a complete device whereas PL is also applicable to films and single crystals. Since the PL measurements on CdTe crystals or films are not necessarily analogous to measurements of CdTe within a device because of additional processing steps such as $CdCl_2$ treatment and back contact application, the study of both EL and PL on the same complete device are more reasonable. Measurements of this kind are presented in this section.

In previous section, using intentionally engineered non-uniformities we have shown that inhomogeneity in EL intensity results mostly from variations in transport, rather than variations in recombination [24]. Indeed, PL intensity varied little with location. Subtle spectral changes were noted between Cu-rich and Cu-poor regions in both EL and PL. Not addressed was the difference in spectral structure between EL and PL. This difference is the focus of this section.

### 1.4.1 Technical

Light biased EL measurements were performed at room temperature. A VTD solar cell was forward biased to obtain an average current density of ~125 mA/cm$^2$. Monochromatic light bias was provided with a halogen lamp and narrow band-pass filters. A 1.91 eV low-pass filter placed in front of the objective allowed EL to pass while blocking reflected bias light.

The Acton 300i spectrometer and Spec-10:100BR CCD array detector was used for temperature variation, simultaneous spatial/spectral resolution, and combined EL/PL

measurements. The specifics of this setup can be found in Sec. 1.3.2. With PL, the path of the laser beam to the sample was several meters, resulting in a wide beam that was roughly uniform over the area of the cell imaged through the slit. Except where indicated, a 1.96 eV HeNe laser was used to induce PL. Apart from bias-dependent PL, PL was measured under open-circuit conditions ($V_{oc}$).

### 1.4.2    Results and discussion

Fig. 1.15 shows that mean EL intensity increases with light bias while non-uniformity decreases (NU = the standard deviation of EL intensity divided by the average EL intensity). Keeping light power approximately constant, the photon energy used for the bias had the greatest effect in the $2 - 2.25$ eV range, the highest that is not absorbed by the CdS, indicating that the effects seen were mostly due to changes in the CdTe with light (possibly photoconductivity of the CdTe). A no-current image was subtracted from the EL image to isolate EL from any PL that may have been generated by the bias light, fluorescence of the glass, or reflected light that was not completely filtered out. Fig.1.16 shows an example of EL images with and without light bias.
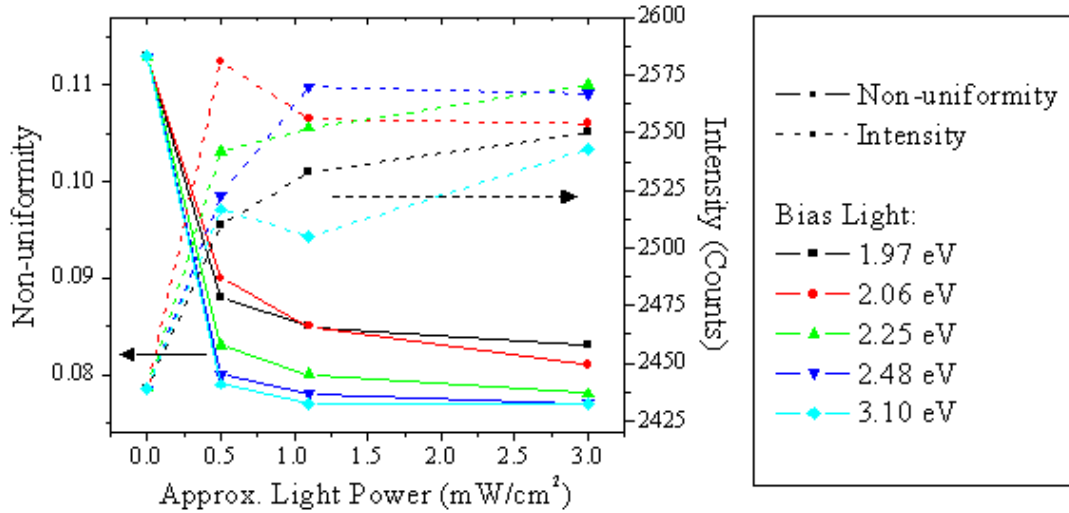


**Figure 1.15.**   EL non-uniformity and mean intensity versus light bias. EL non-uniformity (stand. dev. intensity/ avg. intensity) is indicated by the left axis and solid lines and relative EL intensity is indicated by the dashed lines. T = 300 K.

Both EL and PL spectra were found to have the greatest intensity and most amount of structure at lower temperatures, thus most of our effort was concentrated on low temperature measurements. As mentioned above, EL and PL spectra can differ significantly from each other. One way in which this effect manifests itself is a spectral variation by location that is present in EL but not in PL as can be seen in Fig. 1.17.

No light              ~3 mW/cm$^2$
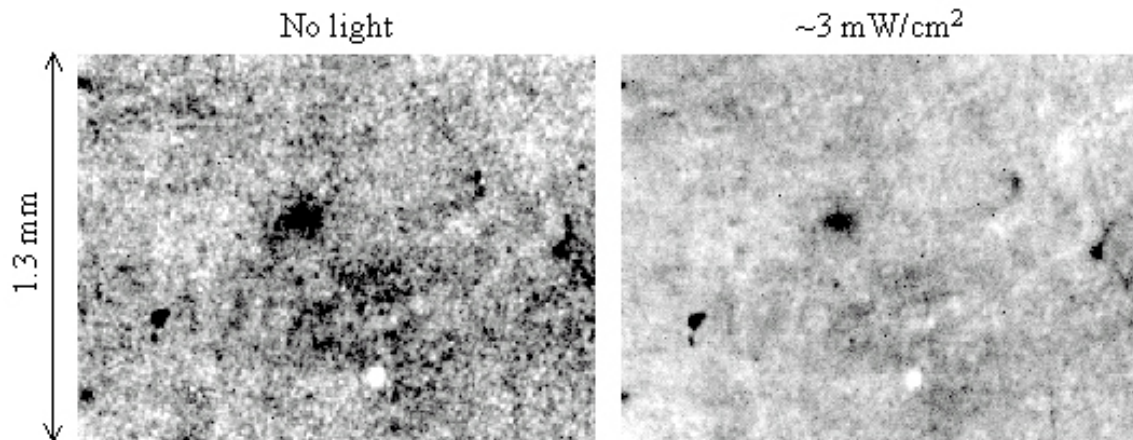


**Figure 1.16.** EL images with no light bias versus 3.1 eV light bias. T = 300 K.
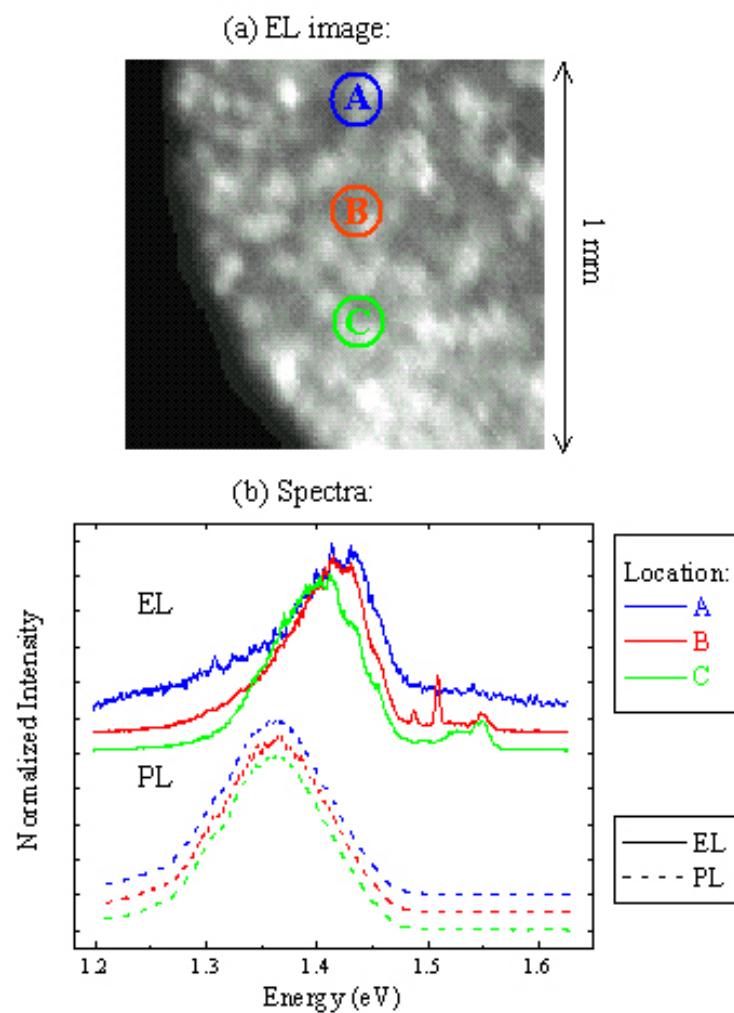
(a) EL image:



(b) Spectra:



**Figure 1.17**     EL image (a) and EL and PL spectra (b) taken from three different points on a cell. The EL spectrum varies by location but the PL spectrum does not. T = 83 K. EL injection level is of 0.13 mA/cm$^2$. PL injection is of 25 mW/cm$^2$

15

Injection level variation revealed some key differences between EL and PL, shown in Fig. 1.18.
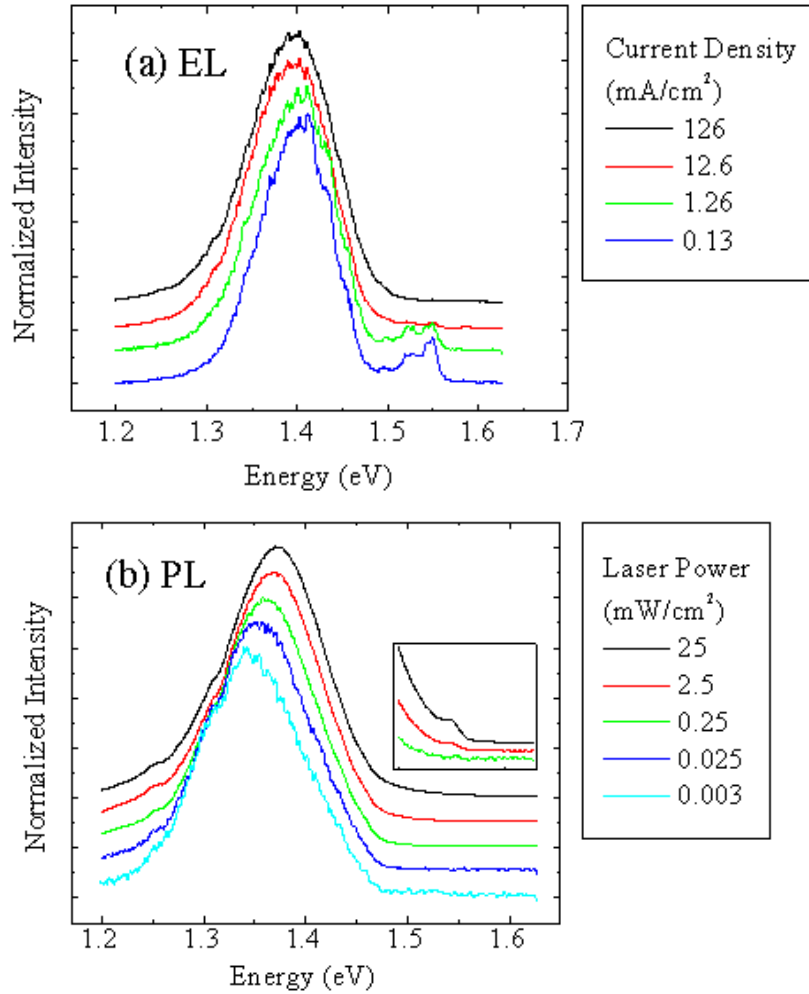


**Figure 1.18.** Normalized EL (a) and PL (b) spectra. EL shows changes in structure and increase in band-edge emission with decreasing injection. In contrast, PL shows no change in structure and an increase in band edge emission (detailed in the inset figure) with injection. T = 83 K.

As injection level increased, EL and PL intensity both increased linearly. We note that this observation is in contrast to Compaan *et al*. who have observed a super-quadratic increase in EL intensity with current density [15]. We believe this discrepancy may have resulted from the use of very low injection conditions and/or a detector with a cut-off at 1.1eV here as opposed to 1.4 eV in [15]. In EL, there are two major trends in the spectra as injection level increases: structure becomes less prevalent and the band edge features diminish. By contrast, PL spectra show no change in structure with varying injection and show increased band edge emission with increased injection.

To find the origin of these dissimilarities, the PL conditions were varied to better resemble the conditions under which EL is measured. These results are summarized in Fig.1.19.

16
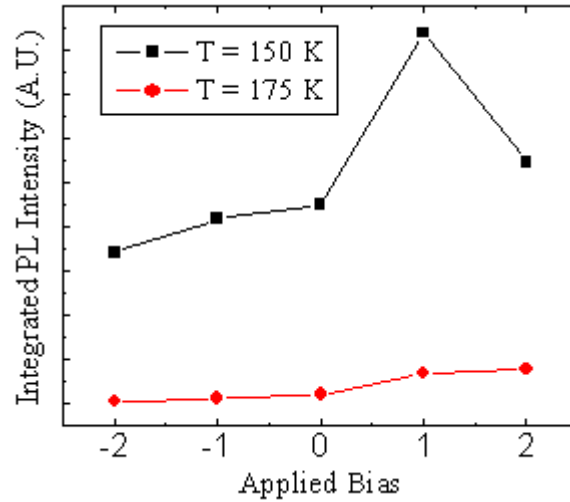
**Figure 1.19**     Integrated PL as a function of applied bias. There is non-monotonic behavior of PL intensity with bias at temperatures of ~100-150 K. Temperatures of 175 K and above show monotonic behavior. Injection level = 25 mW/cm$^2$.

One difference between EL and PL is the applied bias. Though some forward bias will result from the laser in PL measured at $V_{oc}$, EL is under much higher forward bias for even moderate injection. Furthermore, current is allowed to flow out of the cell with EL and non-$V_{oc}$ PL. At higher temperatures (175 K), forward bias (FB) increased PL intensity whereas reverse bias (RB) suppressed it with little change in spectrum. FB decreases the size of the depletion region, allowing injected carriers more time to recombine while RB increases the depletion region, sweeping carriers away before they can recombine. As the temperature is decreased to 150 K, the RB behavior remained qualitatively the same whereas FB behavior changed. +1 V FB greatly increased PL intensity with respect to $V_{oc}$ but +2 V FB yielded decreased emission with respect to +1 V (though still slightly greater than $V_{oc}$). Again, the spectrum changed little with applied bias. This non-monotonic dependence of PL intensity on voltage can possibly be explained by considering effects of the back contact Schottky barrier. When the size of the main junction is attenuated under FB, the Schottky barrier is under RB and therefore grows in size. There is no reason to expect the temperature dependence of the main junction and Schottky barrier to be identical. Perhaps at 150 K, the Schottky barrier width grows faster with bias than the main junction. At +2 V FB, the back barrier may be large enough to separate light-induced electron-hole pairs and suppress PL emission.

Below 100 K, PL intensity was nearly constant with applied bias. However, the spectrum changed. With greater than +1 V FB, the band edge emission was suppressed (Fig. 1.20), much like EL under higher injection conditions. Still, no change was observed in spectral structure of the main peak. Therefore, the opposite trend of the EL and PL band edge as injection level is varied can be attributed to the difference in bias conditions and/or current transport. Note, PL intensity was much greater than EL intensity at the biases used. Accordingly, EL contribution to the biased PL signal was negligible.
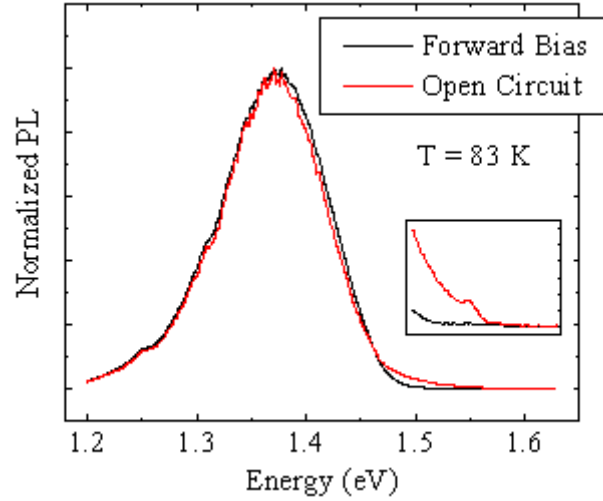
**Figure 1.20** PL spectrum versus bias. Note the decreased band edge emission in forward biased PL at temperatures below 100 K. The inset shows a detail of the band edge. Injection level = 25 mW/cm$^2$.

Besides voltage, EL measurement conditions could be dissimilar from PL because of the location of recombination. In addition to lateral variation as shown in Fig. 1.17, EL and PL could originate from different depths. PL should mainly originate from approximately the same depth at which the laser is absorbed, i.e. 99% within the first micron of CdTe for photons of 1.96 eV. The depth of EL recombination can be approximated by taking the product of free electron and hole concentrations, $n \times p$ [25]. As shown in Fig. 1,21, modeling with AMPS-1D places the peak in free carrier concentration, (and therefore EL emission) at the main junction, as in PL, but penetrating deeper into the CdTe than the PL.
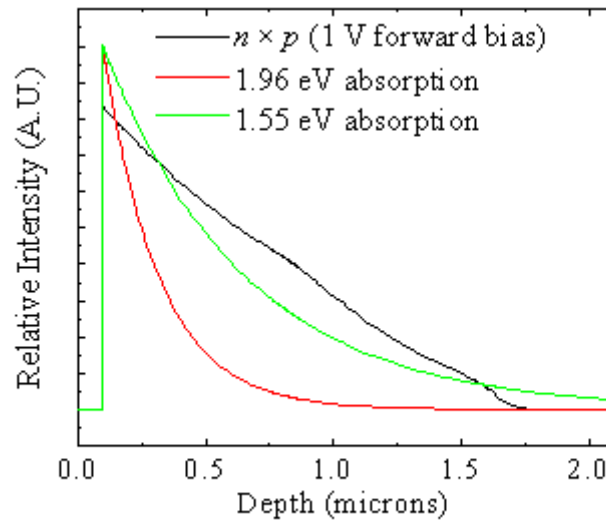


**Figure 1.21** Modeled depth distributions of EL versus PL intensities. The $n \times p$ product distribution indicates the depth of EL emission and the distribution of absorption of different laser wavelengths indicates the depth of PL emission.

18

By changing to a lower energy laser, however, the laser absorption depth (and therefore the PL emission) can be changed to more closely resemble the depth profile of the EL emission. A tunable Ti-sapphire laser was used for this purpose, providing a range of laser energies down to 1.57 eV. This energy was very close to the CdTe band gap at 83 K and thus should provide electron-hole pairs throughout the depth of the device. No change in the PL spectrum was observed with the change in laser energy indicating that the difference in EL and PL spectra is not due to a difference in the depth of recombination.

We could not achieve an increase in spectral structure by changing the bias conditions of PL or the laser excitation energy (and hence sampling depth of PL). We speculate that the increased structure in EL spectra likely results from recombination that is laterally separated from that of PL. This hypothesis is further supported by the EL spectral variations observed by altering location. The fact that PL spectra do not vary by location implies that the variations occur on a scale smaller than can be resolved with our equipment (less than 10 microns). This scale is approximately that of CdTe grains. There is much evidence for increased conduction along grain boundaries and/or certain grains. These results include increased current injected with a scanning tunneling microscope along grain boundaries and certain grains [26], depletion of grain boundaries as measured by scanning capacitance measurements [27], and increased photocurrent collection along grain boundaries [11, 28]. Because EL is selective of areas of lowest resistance, perhaps under low injection conditions it originates primarily from grain boundaries and/or certain grains. If these areas are more defective than the bulk, this reasoning explains the increased spectral structure EL possesses at small currents. The lack of spectral structure of PL is also explained because the injection is uniform across grain boundaries and the bulk. This large sample area results in spectra that are averaged over a larger region (many grains and grain boundaries).

### 1.4.3.  Summary

The differences between EL and PL spectra were explored at wide variation of conditions available for EL and PL measurements. The strongest spectral structure was obtained with low injection EL at low temperature. Band edge features in EL become weaker with increased injection while for PL the opposite behavior was observed. The enhanced spectral structure of EL may be attributed to the sensitivity of EL to current transport that may preferentially select defective areas of the device. For this reason, EL may have advantages relative to PL for defect studies of CdTe solar cells.

### 1.5   Interactions between Cu and CdCl$_2$

Two key processes that allow for production of high efficiency CdTe solar cells are the use of Cu doping at the back contact and employing an anneal in the presence of CdCl$_2$ following CdTe deposition. Except for special laboratory test cells, these processes are used by all known current producers of CdTe based devices. The effects of Cu were isolated in Sec.1.3 with the use of Cu dot cells. It was noted that some features attributed to Cu were visible even in non-Cu doped regions. The explanation of this observation was that some amount of Cu was present on the entirety of the cell due to Cu contamination of the CdTe source material and CdCl$_2$. Here, different CdCl$_2$ treatments (including the use of 99.999% pure CdCl$_2$) were

employed in hopes of enhancing the contrast between intentionally Cu doped and non-Cu regions. However, it was found that Cu related features were still present in all samples but that the type of $CdCl_2$ treatment profoundly influenced the spectral structure of EL emission.

## 1.5.1   Experiment

Cu-dot cells were processed using VTD material as described in Sec.1.3. The $CdCl_2$ treatment, however, was varied. In addition to the standard $CdCl_2$ treatment used for VTD material (the "wet" treatment), an anneal in the presence of $CdCl_2$ was conducted using a dry, vapor process. Two $CdCl_2$ bead sources were used: a standard grade of $CdCl_2$ ("impure, vapor"), as well as 99.999% pure $CdCl_2$, with 0 ppm Cu ("pure, vapor"). The $CdCl_2$ anneal was performed at NREL. The CdTe substrate was suspended above the $CdCl_2$ beads. The chamber was evacuated and the $CdCl_2$ heated to 200 ºC with a quartz lamp to outgas the $CdCl_2$. The chamber was then filled with 100 Torr $O_2$ and 400 Torr He. Both the CdTe and the $CdCl_2$ were radiantly heated to 400 ºC for 10 minutes, and then allowed to cool.

Both EL and PL were measured on the cells. The measurement temperature was in the range of 37-55 K as noted in the figures below. EL injection conditions were 25 mA/cm$^2$, except where noted. PL measurements were found to be largely insensitive to the type of $CdCl_2$ treatment, and showed little variation between Cu doped and non-Cu regions. As such, the data presented here will focus on EL measurements. The lack of contrast between different PL measurements as compared to EL measurements was discussed in Sec. 1.4.

## 1.5.2.   Results and discussion

Cells processed with the wet, impure $CdCl_2$ treatment showed consistent inversion of the EL pattern below 100 K. The EL spectra of these cells varied somewhat from cell to cell, but the general shape remained the same and they all resembled the spectra presented in Fig.1.13. In particular, the DAP peak remained the dominant feature. Depending upon temperature and injection conditions, Cu related features showed enhanced intensity relative to the main peak in Cu doped regions, consistent with previous experiments (Figs. 1.22 and 1.23). Excitonic features near the band edge were more prominent in cells with the wet treatment.

Inversion of the EL pattern as temperature decreased occurred inconsistently in cells with the vapor treatment. This result implies a different set of electrical transport dominating defects than $Cu_{Cd}$ and $V_{Cd}$ that were described in Sec.1.3. Four cells treated with the pure, vapor $CdCl_2$ and three cells treated with the impure, vapor $CdCl_2$ were characterized. In cells in which the inversion did occur (type A behavior), spectra were similar to that of the cells with the impure, wet $CdCl_2$ treatments (Figs 1.24 and 1.25).
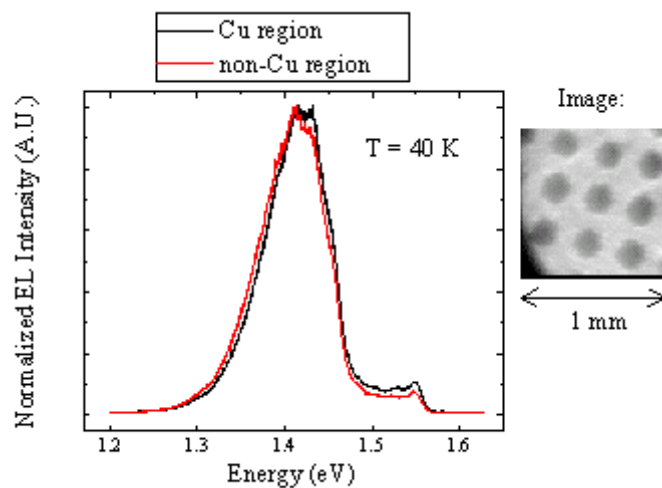
**Figure 1.22** EL from a Cu dot cell with the wet, impure $CdCl_2$ treatment. Average current density is of 25 mA/cm$^2$.
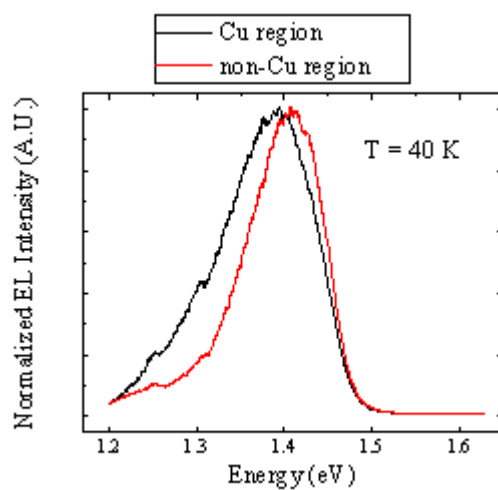


**Figure 1.23** EL from a Cu dot cell with the wet, impure $CdCl_2$ treatment. Average current density is of 125 mA/cm$^2$.
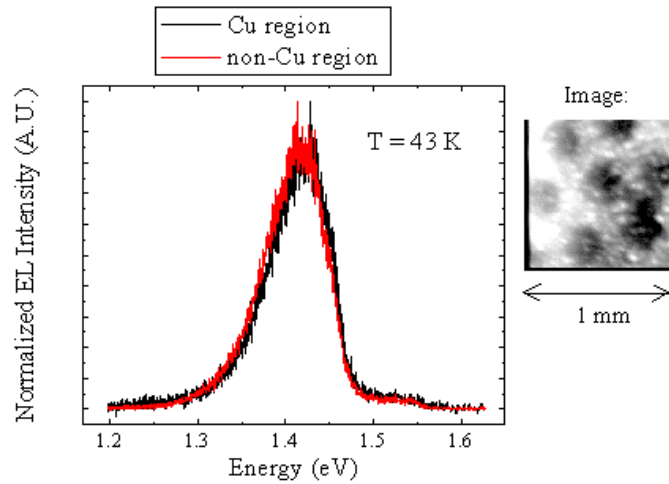
**Figure 1.24** EL from an inverting Cu dot cell with the vapor, impure CdCl$_2$ treatment.
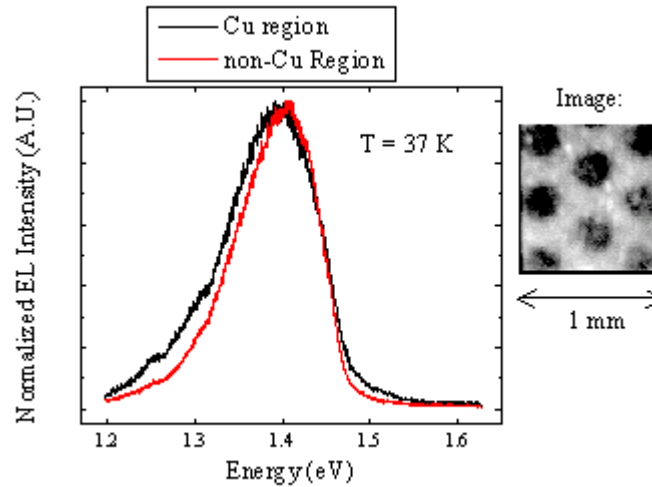


**Figure 1.25** EL from an inverting Cu dot cell with the vapor, pure CdCl$_2$ treatment.

Two of the "vapor, pure" cells, and one "vapor, impure" cell exhibited type A behavior. Where inversion did not occur (type B behavior), spectra from non-Cu regions resembled previous data, but spectra from Cu doped regions departed from previous measurements (Figs. 1.26 and 1.27). The spectral differences in type B cells were more pronounced in the cells treated with the pure CdCl$_2$. In both pure and impure CdCl$_2$ treated type B cells, the Cu regions showed greatly enhanced emission around 1.30 and 1.25 eV, attributed to Cu$_{Cd}$, in Sec1.3. Though a similar effect was seen in type A samples, the relative intensities of these features were much greater in type B cells.
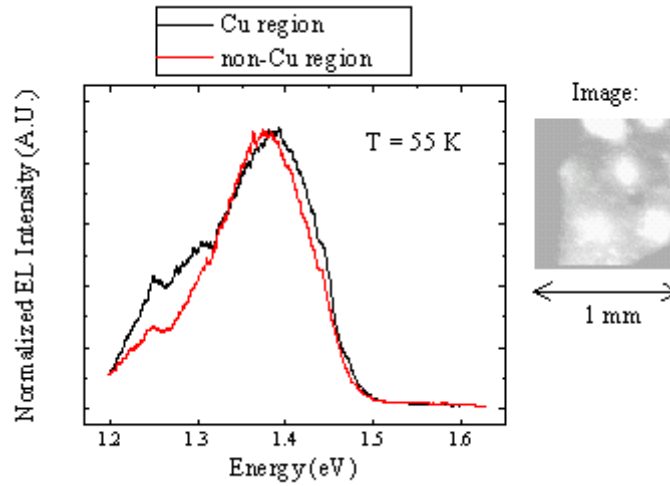
**Figure 1.26** EL from a non-inverting Cu dot cell with the vapor, impure CdCl$_2$ treatment.
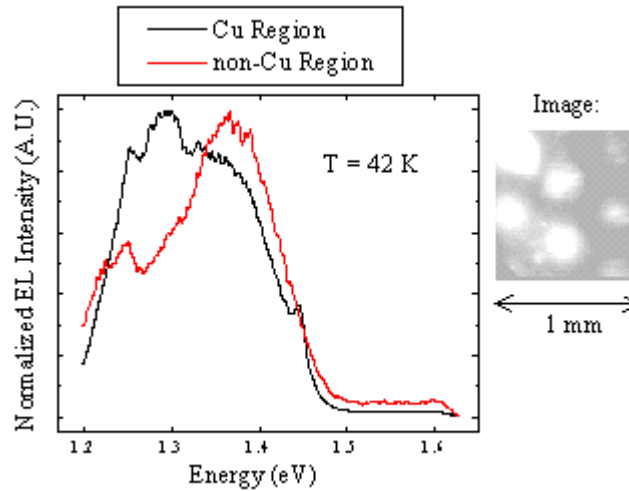


**Figure 1.27** EL from a non-inverting Cu dot cell with the vapor, pure CdCl$_2$ treatment.

In the type B, pure, vapor CdCl$_2$ treated cells, the intensities of these low energy peaks was equal to, or exceeded that of the DAP band, centered near 1.4 eV. It should be noted, however, that the exact peak location of the lower energy features in Figs. 1.26 and 1.27 is obscured because the detector loses sensitivity as the energy approaches its band gap of 1.1 eV. The Cu regions of the type B, pure, vapor treated cells also showed a very sharp feature at 1.45 eV. This feature is sometimes visible as a small shoulder on inverting cells, but not as a distinct peak. Due to the non-inverting nature of the type B EL pattern, it was considered that these differences in spectra were injection related. (That is, Cu doped regions in non-inverting, type B cells were receiving a disproportionately high amount of current compared to Cu dots in inverting, type A cells.) However, varying the average current density such that there were EL spectra of comparable intensity from both Cu doped and non-Cu regions resulted in qualitatively the same behavior, showing that injection level was not the only factor affecting the spectra in

type B cells. The large spectral differences in type B cells support the hypothesis that the electrically active defects vary from those of type A cells.

In summary, (a) all cells that exhibited an inverting EL pattern at low temperature (bright Cu dots → dim Cu dots), regardless of $CdCl_2$ treatment consistently showed similar spectral features; (b) inversion was always observed in cells with the impure, wet treatment; (c) when cell remained un-inverted at low temperature (Cu dots remained bright), a different spectrum was observed in Cu-doped regions.

### 1.5.3. Summary

It is shown that the variability of the $CdCl_2$ treatment is most prevalent in Cu-doped regions of the cell, which suggests that the incorporation of Cu into the CdTe is profoundly influenced by the $CdCl_2$ treatment. When studying CdTe devices, it may be impossible to totally decouple the effects of Cu doping from those of the $CdCl_2$ treatment. This would be consistent with the general observation that changing one step in device processing often necessitates re-optimization of many or all other steps.

Further defect studies involving variations of the $CdCl_2$ treatment and its interaction with Cu would help to clarify the results. Identification of the defects responsible for the peaks observed in the cell PL and EL spectra is not unambiguous. However, there were still patterns that can be identified within the inconsistencies:

- all cells showed similar spectra in non-Cu regions
- only cells treated with vapor $CdCl_2$ showed non-inverting behavior
- only non-inverting, pure, vapor treated cells showed spectral structure that greatly departed from that of cells measured previously, and only in Cu doped regions
- different spectral structure was consistent amongst the non-inverting, pure, vapor treated cells measured.
- the wet $CdCl_2$ treatment was probably more uniform than the vapor one because those cells produced consistent, inverting EL behavior at low temperatures.
- variations among cells processed with vapor, pure $CdCl_2$ treatment indicate greater process sensitivity to high purity $CdCl_2$ than to lower purity $CdCl_2$.

### 1.6 $CdCl_2$ Effects Studied with Non-Uniform Treatment and Spatially Resolved Luminescence Techniques

The intentionally non-uniformly processed cells (the approach used in Sec.1.3 for studying Cu), are used in this section for investigation of the effects of $CdCl_2$ treatment. As was the case with Cu the use of patterned $CdCl_2$ allows for built-in experiment and control conditions within each solar cell, eliminating cell-to-cell variations that contaminate data in studies that try to isolate a single processing condition (e.g., see Sec.1.5).

### 1.6.1. Experiment

Structures used for this experiment were of VTD CdS/CdTe material not treated with $CdCl_2$. Post CdTe deposition processing and contacting were performed at CSM. A modified CSM $CdCl_2$ misting process, followed by annealing, was used to apply $CdCl_2$ to the CdTe surface. Prior to application of $CdCl_2$, the cell was placed in a special mount shown in Fig. 1.28.

A stainless steel frame clamped a stainless steel shadow mask with 150 μm diameter holes and the cell down to the aluminum base. It was necessary to keep the shadow mask pressed to the cell during anneal to ensure that masked regions would remain untouched by $CdCl_2$ mist. Despite this precaution, some contamination of masked regions likely occurred. Use of the metal base and shadow mask was necessary to withstand the standard 400 ºC anneal temperature. An alternative might be to use photolithography to pattern the cell. However, photoresist, polymerizes and is difficult to remove at the high temperatures of the $CdCl_2$ treatment. A 1 *M* solution of $CdCl_2$ was atomized and misted onto the CdTe surface for 2 minutes. This method produced some cells with well-defined regions of brighter EL emission (and therefore well-defined $CdCl_2$ treated regions) but other cells showed vague non-uniformities. A superior method of producing $CdCl_2$ dots for the future might be to use the shadow mask with a vapor transport type $CdCl_2$ system, rather than the wet treatment used here. The back contacts were applied with the standard Cu/Au recipe as described in Sec. 1.3.1.
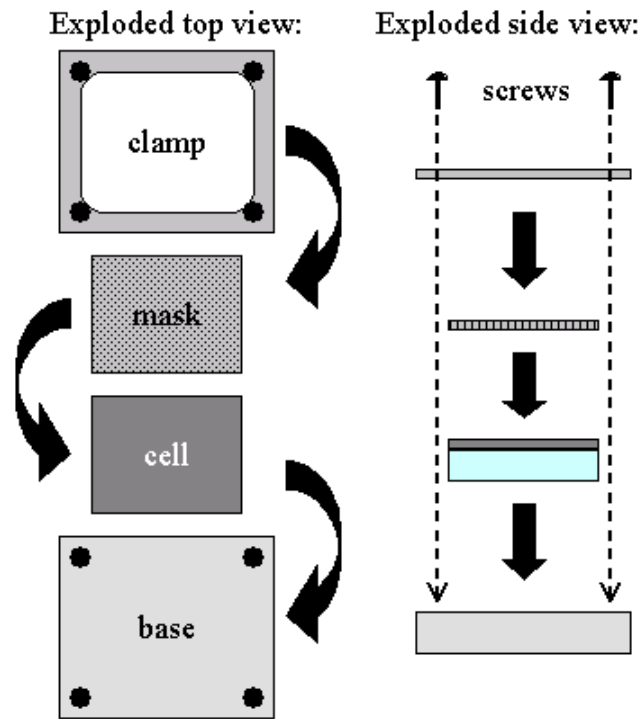


**Figure 1.28** Experimental setup for processing $CdCl_2$ dots.

To find $CdCl_2$ regions of the cell, the same type of technique that was employed with the Cu dots was used. EL images showed enhanced emission from $CdCl_2$ treated regions as detected with the spectroscopy system in imaging mode. However, this contrast between $CdCl_2$ treated regions and untreated regions disappeared at temperatures below 200 K, leaving an EL image with no regular pattern. Thus, to locate $CdCl_2$ regions at low temperature, images at higher temperatures were relied upon. This method was not without its faults, as the position of the cell would change slightly at lower temperatures due to thermal contraction of the cryostat arm. To mitigate this shift, the edge of the solar cell could be used as a reference point. Once the $CdCl_2$ regions were located with EL imaging at higher temperatures, the temperature was lowered to

increase spectral resolution. Spectra were obtained by closing the entrance slits to 100 μm and rotating a diffraction grating into position within the spectrometer.

### 1.6.2. Results and discussion

Fig. 1.29 shows a series of EL images acquired at different temperatures with an injection intensity of 125 mA/cm$^2$ to increase the EL contrast. The CdCl$_2$ treated regions (some of which are indicated with red arrows) are visible as bright dots at higher temperatures, but disappear below 200 K. The edge of the cell can be seen in the lower right corner of each image. Image brightness was set for each image individually to allow for maximum contrast. Mean EL intensity increased with decreasing temperature. Indeed, the image obtained at 50 K has several bright spots where the pixels are saturated.
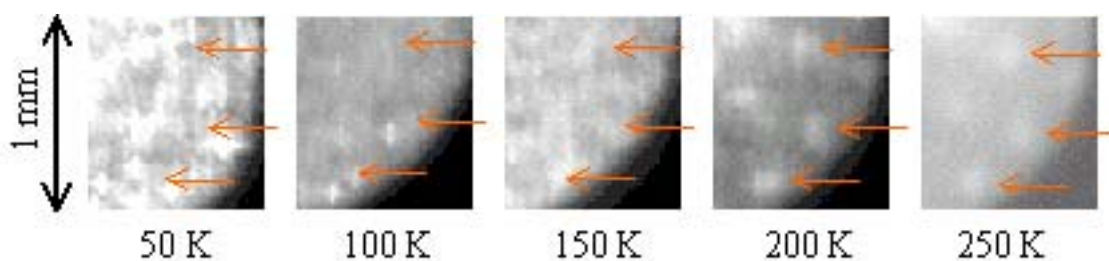


**Figure 1.29** EL images versus temperature for CdCl$_2$ dot cells. Average injection level is of 125 mA/cm$^2$. The red arrows indicate the locations of selected CdCl$_2$ treated regions.

The increased EL emission from CdCl$_2$ treated regions at higher temperatures implies increased conduction, likely resulting from doping of the CdTe during the CdCl$_2$ treatment, leading to reduced series resistance of the bulk CdTe and possibly reduced back contact resistance. One possible doping mechanism is the formation of the so-called "A-center," a complex consisting of $V_{Cd}$ and $Cl_{Te}$. This shallow acceptor has been identified with electrical transient measurements to exist at $E_V + 0.12$ eV [29]. The A-center may help to dope the CdTe by replacing the $V_{Cd}$ acceptors otherwise compensated with Cl, $Cu_i$, or other donor defects.

The disappearance of the CdCl$_2$ dots below 200 K might be attributed to the freeze-out effect as it was for Cu-dot cells. The fact that this freeze-out occurs at a relatively high temperature indicates the involvement of a deeper defect state than the A-center. Because the EL image transitions from bright CdCl$_2$ dots to a "flat" image, the CdCl$_2$-induced defect in question is likely not replacing another defect that aids conduction (albeit to a lesser extent than the CdCl$_2$-induced defect), as was the case with the $Cu_{Cd}$ versus $V_{Cd}$ in the inverting Cu dot cells

Because of the aforementioned difficulty with consistent CdCl$_2$ processing, EL spectral data fluctuated from cell-to-cell. By comparison, PL spectra varied little, both by location and between cells, as observed in Sections 1.4 and 1.5, respectively. Accordingly, EL spectra are focused on here.
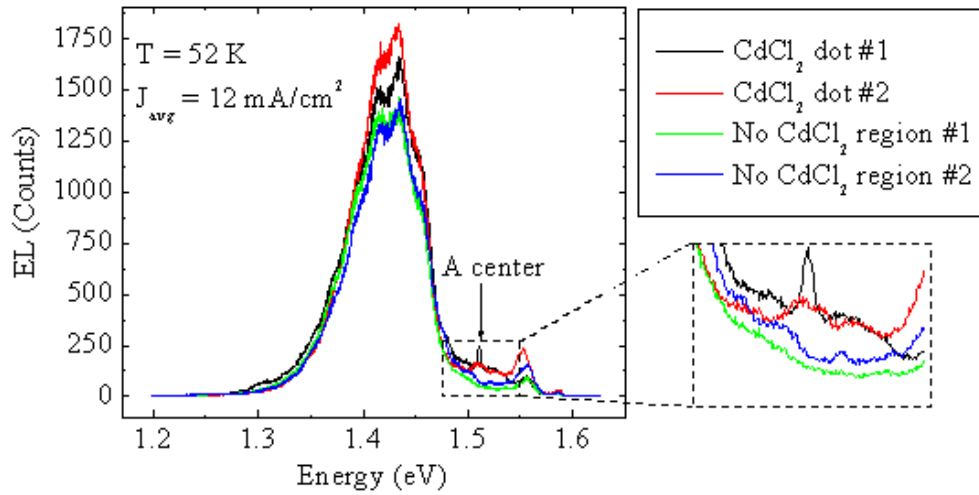
**Figure 1.30** EL spectra from CdCl$_2$ dots and untreated regions. The arrow indicates emission from CdCl$_2$ treated regions that could involve the A-center.

In order to ensure consistent results from areas that could be confidently identified as being CdCl$_2$ treated or not, spectra were acquired from regions of the cell that produced multiple areas of both CdCl$_2$ dots and untreated regions. Fig. 1.30 shows spectra from such a zone, two each from CdCl$_2$ dots and untreated regions. A sharp feature at 1.51 eV consistently appears in the CdCl$_2$ dots but does not appear in the untreated regions. A spectrum that corresponds well to that of the CdCl$_2$ dot spectra from Fig. 1.30 has been observed before in Ref.22, and was labeled as an "unidentified spectrum", thus not attributed to the A-center.

It should be noted that a clearly resolved spectrum in which the suspected the peak under discussion could be seen was only obtained from one cell. However, we can be confident in this data because the feature consistently appeared in two different CdCl$_2$ treated regions and did not appear in two separate untreated regions. In order to see clearly this tiny feature, a very specific injection level was required (Fig.1.31). Too low a current density and it was not excited. Too high a current density and the shallow defect was washed out from much more intense emission resulting from the main DAP band. It was only through the "fortuitous" choice of injection current that the tiny feature could be clearly resolved. Probably this is the reason why we did not see this peak in spectra presented in previous sections. The current density required to see such a subtle feature would logically change from cell-to-cell along with other varying properties such as J-V behavior.
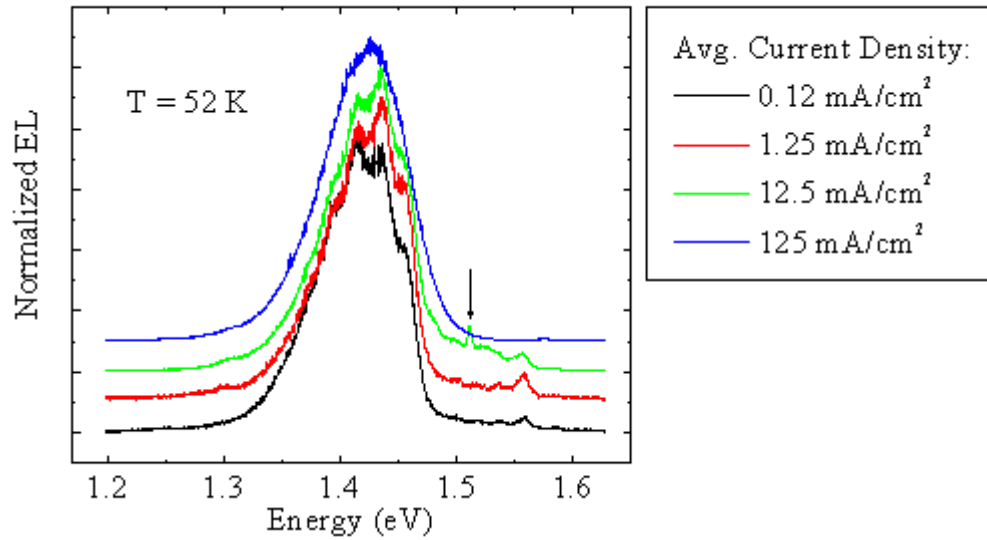
**Figure 1.31** EL spectra from a $CdCl_2$ treated region at different injection intensities. The arrow indicates emission from $CdCl_2$ treated regions that only visible at 12.5 mA/cm$^2$.

### 1.6.3   Summary

Main results of preliminary investigation of the effects of $CdCl_2$ through the use of non-uniform $CdCl_2$ treatment are as follows:

- $CdCl_2$ treated regions provide higher current densities causing higher EL intensity than the untreated regions at T>200K.
- $CdCl_2$ treatment apparently increase doping level at T>200K through creating not too deep acceptor levels, supposedly $V_{Cd}$-$Cl_{Te}$ complexes (A-centers)
- Mechanism of the observed inversion of the El brightness around T=200K is still unclear. It might be that the major defect responsible for higher conductance at higher temperature is not A-center, but deeper acceptor, perhaps partially compensated which makes temperature dependence of carrier concentration sharper.
- It is important to widely vary conditions of measurements in purpose not to miss manifestations of some defect related electronic states in the EL and PL spectra. This may help making our knowledge of the defect related states more complete as well as identification of these states more reliable.

### 1.7.   Non-Uniformity Mitigation: the Effects of Window Buffer layers

The addition of the high-resistance TCO (HRT) buffer layers is known to increase efficiency, and its value is underscored by its presence in record CdTe and CIGS devices. Though HRT's are a potential boon to growers of high-efficiency solar cells, the additional processing step that is required to deposit the HRT is not ideal for large-scale production. Thus, determination of the exact role of the HRT could provide manufacturers with an alternative to adding a processing step, decreasing production costs.

Through numerical modeling and indirect, one-dimensional measurements, Rau and Schmidt attribute the role of the HRT intrinsic ZnO layer to prevention of electrical

inhomogeneities in CIGS cells [30]. Karpov *et al.* further show how, in general, non-uniformity can be detrimental to solar cell performance [6, 31].

Here, we directly observe the non-uniformity mitigation effects of the HRT in CdTe cells through spatially resolved electroluminescence (EL) and light-beam induced current (LBIC) measurements. This decrease in non-uniformity has been measured in CdTe cells prepared at both NREL and CSM, both with and without HRT layers. Finally, we attempt to identify the cause of the non-uniformity in question, which appears to be related to areas of thin CdS.

## 1.7.1 Experiment

Cells were manufactured using standard procedures at NREL [32], and CSM [33, 34], detailed elsewhere. Addition of an HRT layer was the only intentional variation made at each institution.

EL is stimulated by injecting excess carriers through forward bias. Radiative recombination of excess carriers is detected with a CCD array detector. Though influenced by recombination effects at the main junction, EL is most highly sensitive to current distribution [24] and therefore provides a map of electrical transport through the device. Complimenting EL is LBIC. These measurements were performed by Tim Nagle at Colorado State University. In LBIC, light is locally injected into a solar cell with an electronically modulated, focused, 638 nm laser beam. The light-generated current is detected with a lock-in amplifier as the sample is scanned under the laser, giving a spatially resolved quantum efficiency (QE) measurement. For non-uniformity studies of layers of incomplete devices, an atomic force microscope (AFM) along with optical transmission measurements were performed on the same area of the substrate.

## 1.7.2. Results and discussion

Cells from both NREL and CSM with a HRT layer were found to be more efficient than cells without the HRT. The greatest efficiency boost came from fill factor (FF), with open circuit-voltage ($V_{oc}$) and short-circuit current ($J_{sc}$) being relatively constant between the two processing conditions.

Fig. 1.32 graphically shows a decrease in EL non-uniformity associated with the HRT in CdTe cells. Without the HRT, EL originates from isolated spots on the solar cell, with little to no detectable emission between bright spots. Though non-uniformity is not completely quenched with the addition of the HRT, it is greatly mitigated. Bright spots still exist, but they are much less intense with respect to the average intensity, and measurable emission is seen on nearly the entire solar cell. The HRT decreased the NU parameter in the CSM cells from 1.93 to 0.48 and in the NREL cells from 0.64 to 0.21.
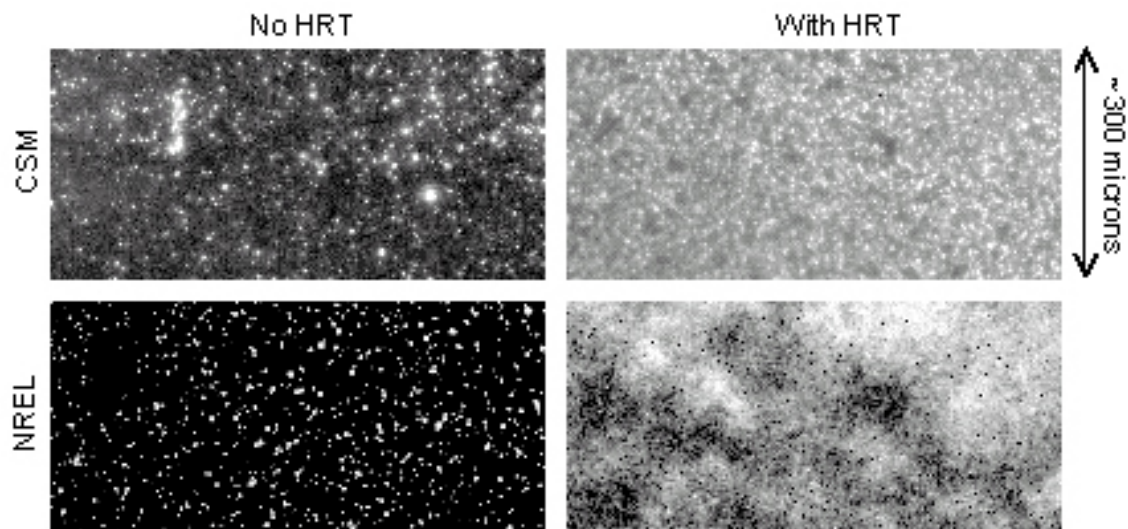
**Figure 1.32.** Electroluminescence from cells produced at CSM and NREL with and without an HRT layer. The non-uniformity visibly decreases with the addition of the HRT.

A similar decrease in non-uniformity with the addition of the HRT layer was observed in LBIC measurements of CSM cells, as shown in Fig. 7.2.
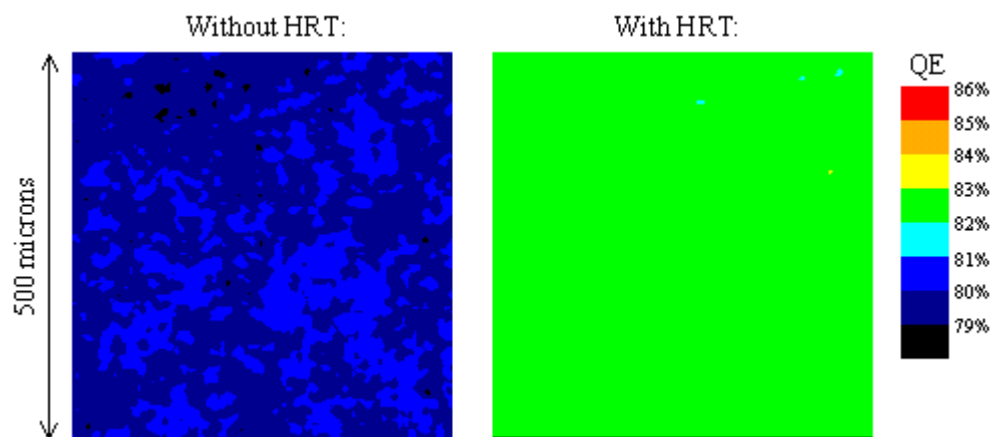


**Figure 1.33.** Light-beam induced current measurements on CSM cells with and without an HRT layer. There is a much lower level of contrast with LBIC than with the EL images of GI. 7.1. Quantum efficiency (QE) is indicated by the scale at the right. There is a decrease in non-uniformity as well as the increase in average QE with the addition of the HRT.

In addition to nearly eliminating isolated spots of low QE, the HRT also increases the average QE. NU decreased by a factor of ~2 (from 0.0036 to 0.0017) with the addition of the HRT. The NU measured with LBIC was much smaller than the NU measured with EL. We have made this observation when comparing EL and LBIC data with many cells in the past, noting that EL is more sensitive than LBIC to variations in device properties.

A correlation was found between the number of bright spots in EL and the number of areas of low QE in LBIC. Namely, both techniques yielded a number density of $10^5$-$10^6$/cm$^2$ in

cells without the HRT. Because the HRT is deposited between the highly doped TCO and the CdS, we suspected the CdS could be responsible for the non-uniformity.

Optical transmission and AFM measurements were performed on CdS grown by chemical bath deposition (CBD) at CSM. These measurements (see Fig. 1.34) were performed on the exact same spot of the CdS. Bright spots in the transmission measurements correspond to high spots in the AFM measurement. The fact that the high spots seen under AFM measurements has not been more widely reported is probably due to the fact that their spacing (~10 µm apart) is large enough to be outside of normal scan ranges (a composite of four adjacent AFM scans at full range was used for this study). The number density of these spots is ~$10^6$/cm$^2$, suggesting these inhomogeneities in the CdS could be responsible for the observed non-uniformity in EL and LBIC measurements.
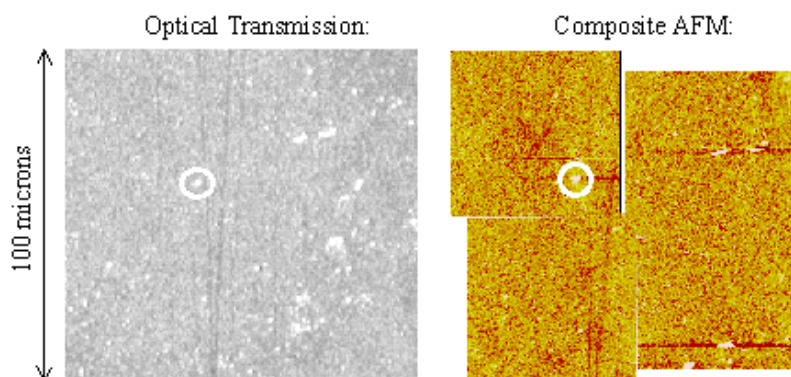


**Figure 1.34.** Mapping the CdS with optical transmission and AFM measurements. Lighter areas in the AFM image correspond to higher spots. The AFM is a composite of four scans. The circled bright spot in the transmission measurement corresponds to the circled high spot in the AFM measurement.

The increase in optical transmission coinciding with increased height warrants further discussion. Greater transmission implies decreased CdS thickness, but increased height implies increased thickness. However, the CdS is not grown on a completely flat surface, thus the AFM measures height of the CdS plus the TCO and any contaminants in the layers. High spots could at least partially be due to areas of increased TCO thickness. Indeed, AFM measurements of TCO films (not shown) reveal a surface roughness ~60% that of the CdS surface. In addition to increases in TCO thickness, some of the surface roughness of the CdS is likely due to transparent particulates (such as CdO, organic compounds, or even gas bubbles) formed during deposition. Thus, these rises are not necessarily increases in CdS thickness and could possibly leave a thinner CdS layer on top (Fig1.35). In this self-consistent explanation, areas of high TCO and/or contaminants would account for the high spots observed with the AFM while the thinner CdS atop the mounds would account for the increased transmission.
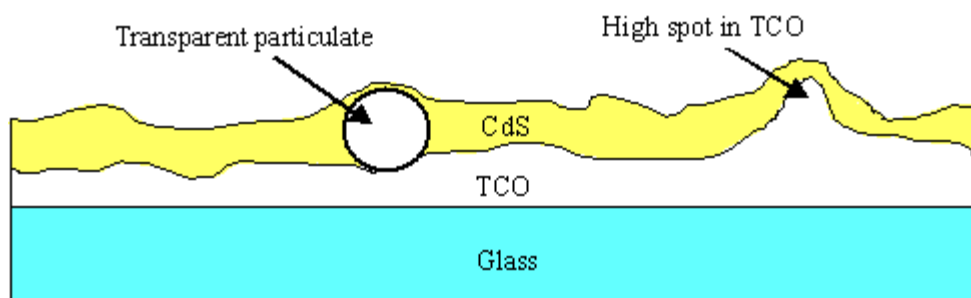
**Figure 1.35.** (not to scale) A proposed explanation of why high spots in the AFM images of CdS-coated plates could correspond to thin spots in the CdS. The high spots could be caused by either high spots in the TCO or particles incorporated into the CdS film. Non-conformal CdS deposition could result in thin CdS on high spots and result in regions with high topography but reduced film thickness.

Though we have shown direct evidence of the non-uniformity mitigating properties of the HRT, the exact mechanism has not been discussed. Visoly-Fisher *et al.* propose that the HRT serves to add additional thickness to the n-type layer that is necessary for high $V_{oc}$ [35]. Accordingly, the full benefits of the HRT are realized when the CdS is intentionally thinned to increase photocurrent (a variation not performed here). Not fully discussed in their study are spatial variations within the plane of the solar cell, the main effect discussed in this section. A solar cell with an average CdS thickness sufficient to support a high $V_{oc}$ can still have local areas of thin CdS exhibiting reduced $V_{oc}$. These regions could be one source of "weak diodes". Therefore, the use of an HRT can improve cell efficiencies even without thinning the CdS, as was the case with the cells studied here. It must be emphasized that thin CdS is not the only possible type of weak diode; they could be generated from multiple sources. Though the most significant change in overall device performance was in increased FF and not $V_{oc}$, simple modeling of a weak diode in parallel with a standard diode (both having some I-V roll-over) can produce a large drop in FF without much change in $V_{oc}$.

The weak diode explanation is corroborated by the EL and LBIC results. As the weak diode has a lower $V_{oc}$, it will pass significantly more current at a given forward bias than the standard diodes surrounding it. This high current produces the bright spots observed in EL. In addition, the origin of the low $V_{oc}$ weak diode is a thin CdS layer, which would result in less band bending. Less band bending would result in less photocurrent, as was observed with LBIC.

### 1.7.3. Summary

- Presence of HRT buffer layer obviously decreases non-uniformity of electric properties of a cell which was demonstrated by comparison of the EL images of cells with and without buffer layers
- The CdS layer could be a strong contributor into efficiency-robbing nonuniformity in the cell electrical properties. It was concluded based on EL mapping of completed cells combined with AFM and optical measurements of TCO/CBD CDS structures. Observed microscopic areas of thinned CdS may constitute one form of a "weak diode".
- HRT layer between TCO and CdS layer probably blocks weak diodes although mechanism of blocking is still unclear

## 1.8 Long-Term Photoconductivity Transients in CdS

CdS photoconductivity has been widely reported, and has been used to explain effects such the dependence of apparent quantum efficiency on electrical bias [38,39]. However, CdS effects are sometimes confused with CdTe photoconductivity when explaining effects such as I-V crossover (i.e., non-superposition of the light and dark J-V curves) [40]. Here, evidence of photoconductivity in CdS was observed with electroluminescence (EL) measurements of CdS/CdTe solar cells.

### 1.8.1. Experiment

EL was induced under constant current conditions of 25 mA/cm$^2$. The EL was imaged with the same system as in Sec.1.2. To induce a photoconductive response in the CdS, an Ar-ion laser was employed. This laser can support several discrete excitation energies. Laser energies used were 1.94, 2.41, 2.54, and 2.71 eV. The laser beam was focused into an elliptical shape using a cylindrical lens. After taking an EL image in the dark, laser light was shined on the device. An image of the reflected laser light was recorded. Following this exposure, a second EL image was acquired in the dark.

### 1.8.2. Results and discussion

The photoconductive CdS effect is most easily observed visually with a cell with a high-contrast EL pattern. A Cu dot cell (as described in Sec.1.3) serves this purpose well, as shown in Fig.1.36. The laser energy used was 2.71 eV, with a power density of approximately 1.7 W/cm$^2$. The cell was exposed to the laser beam for 3 minutes. Before laser exposure, EL is seen from Cu dots with a relatively uniform distribution throughout the cell. After laser exposure, the cell's EL pattern changes; bright areas of EL emission are only seen on Cu dot areas that were exposed to laser light.
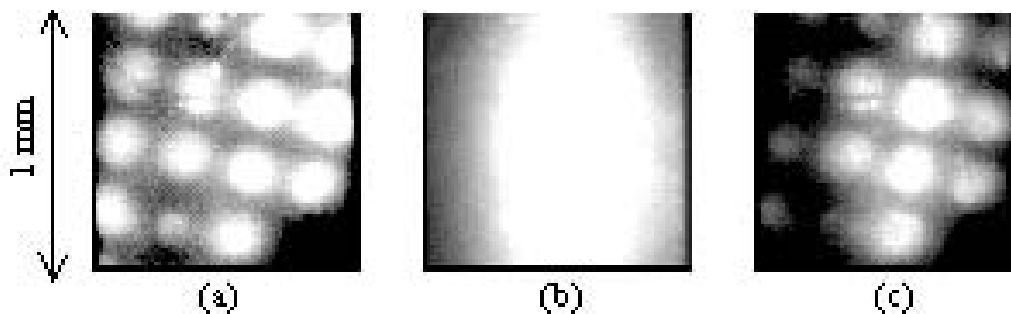


**Figure 1.36.** Photoconductive CdS effect in EL image of Cu dot cell. (a) EL image before laser exposure, the edge of the cell can be seen in the lower right corner. (b) Laser pattern, acquired with reflected image. (c) EL image after 3 minutes laser exposure.

The EL pattern is generally dominated by electrical transport effects [24]. In particular, areas of low resistance, such as the Cu dots described in Sec.1.3, show increased EL because they are preferential current pathways (Fig.1.36a). The image in Fig.1.36c presents the EL image from the portion of the cell exposed to laser. Now the strong EL comes from the area exposed to the laser beam. Within this area it is stronger at the Cu-dot location. Beyond the exposed area even Cu dots look much darker than before. The EL image transformation can be explained by the persistent photoconductivity induced by laser in the exposed area. Current density (and EL intensity) redistributes in favor of now low resistance region in expense of higher resistance unexposed area. The observed effect should be ascribed specifically to CdS by based on experiments with varying laser excitation energy. The band gap of CdS is 2.42 eV [41]. If this effect is to be attributed solely to CdS, then no photoconductive effect should be observed with a laser of insufficient energy to excite the CdS ($\leq$ 2.41 eV).

The processing details of the CSM gas jet deposition cells (GJD) used in the following experiment can be found in Refs. 33 and 34 as well as in Sec. 5 of this report. These cells were made without any intentional non-uniformity (e.g., Cu dots). The results are summarized in Fig. 1.37. An initial EL image was acquired of a cell. Then, the cell was exposed to 1.91 eV laser light of power density $\sim$ 170 mW/cm$^2$ for 5 minutes. A second EL image was acquired. No significant changes were observed in the EL pattern. Next, the cell was exposed to 2.41 eV laser light (just below the band gap of CdS) under nominally the same conditions.
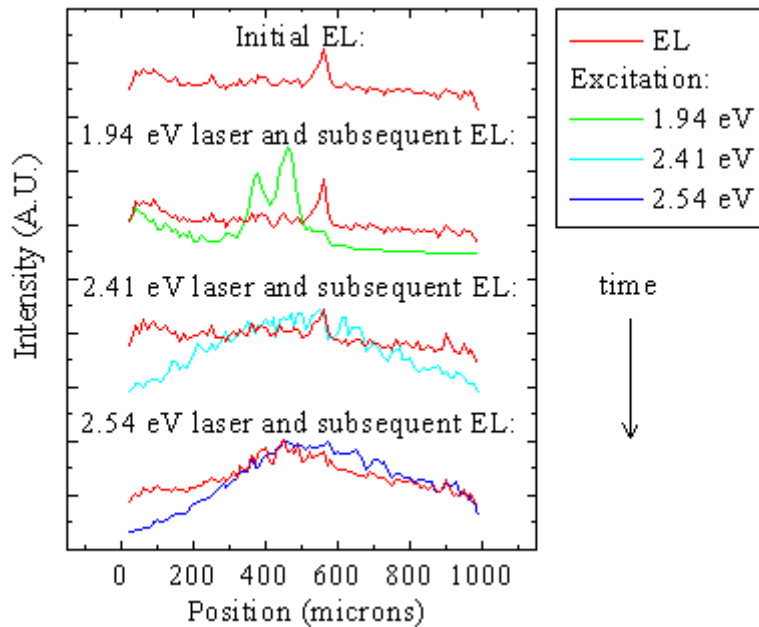


**Figure 1.37.**   Photoconductive CdS effect as a function of excitation energy. The line scans were produced by integrating along the horizontal axis of the detector. EL images were acquired in sequence with laser exposures. The data towards the top of the graph were acquired earlier.

The peak in the EL near 600 μm was due to a localized bright spot. The two peaks in the 1.94 eV laser reflection line are not important. The EL pattern was unaffected by the laser exposure until exposed to 2.54 eV light, at which point the EL line scan mimicked that of the laser.

Minor changes were observed with EL, such as diminished bright spot intensity, but the pattern remained largely the same. After exposure to 2.54 eV, laser light (exceeding the CdS band gap) under the same nominal conditions, the EL pattern changed significantly. The cell exhibited enhanced EL over regions that were exposed to the laser light, and suppressed EL in unexposed regions. Both effects are a result of localized enhanced conductivity that was induced by the laser. The EL intensity is diminished in the unexposed regions because of the constant current excitation conditions: more current in one area must result in less current in others. Because these effects were only observed with optical excitation energies exceeding the CdS band gap, we can be confident that they are due to CdS photoconductivity.

The fact that the change in the EL pattern observable after the laser was turned off, shows that the photoconductive effect persisted after light exposure. Again, a cell was exposed to laser light of 2.71 eV and 1.7 W/cm$^2$ for 30 minutes (not shown). A laser-induced EL pattern change was observed again. After being allowed to "recover" for 21 hours under short circuit conditions in the dark, another EL image was acquired. The cell still showed enhanced emission in the laser exposed region and diminished emission in unexposed regions. However, some decay of the effect was observed, as the contrast between regions was smaller after 21 hours than immediately following laser exposure.

The general trend of greater EL in laser-exposed regions and lesser EL in unexposed regions was used above to show the basic effect of laser-induced, localized CdS photoconductivity. Another observed change in the EL pattern was diminished intensity of bright spots relative to the "background" EL. Bright spot intensity was diminished in both laser-exposed and unexposed regions. A striking example of this effect is shown in Fig. 1.38. A one minute laser exposure of 2.71 eV and 1 W/cm$^2$ was used. Bright spots in the entirety of the image show greatly diminished intensity. The fact that these bright spots are so influenced by the conductivity of the CdS (as modulated by the laser exposure) could be considered as supporting the conclusion in Sec. 1.7 that CdS layer could be a strong contributor into the electrical non-uniformity of a cell.
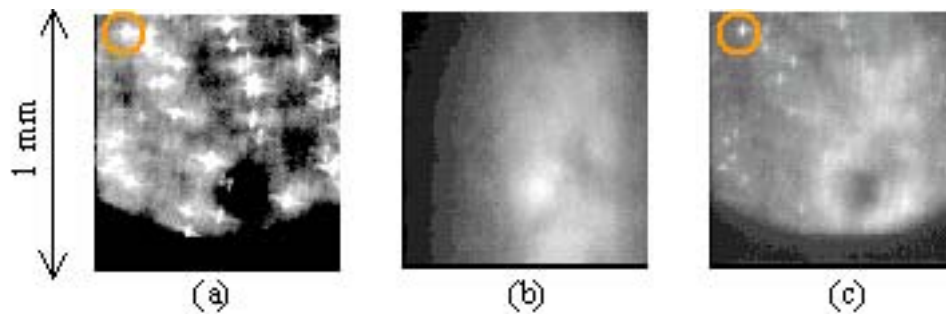


**Figure 1.38.** Photoconductive CdS effect on EL bright spots with CSM cell. (a) EL image before laser exposure. The circled bright spot has an intensity of ~14,000 counts. (b) Laser pattern, acquired with reflected image. (c) EL image after 1 minute laser exposure. The circled bright spot now has an intensity of only ~4,000 counts.

The extremely long lasting effects of the photoconductivity of CdS were easily observed because of extreme sensitivity of EL to spatial variations in cell properties. Previously, the effects of Cu were studied by adding an intentional non-uniformity in the device during processing in the form of Cu dots [24]. Here, a focused laser was used to induce non-uniformity

into the device post-processing. In this way, the CdS was forced into a dominant role in determining cell uniformity with respect to electrical transport and therefore EL pattern. The effect of laser exposure appeared to be a long-term transient. The decay of the photoconductivity could be studied more in-depth by carefully controlling the laser spot and then comparing EL intensities of laser-exposed and unexposed regions over time. Monitoring this decay at different temperatures might allow the extraction of an activation energy for the decay process. Using this technique with completed cells allows one to specifically target CdS related effects, such as variations in CdS process or the use of TCO buffer layers.

### 1.8.3   Summary

- Irradiation of a cell with a laser of photon energy above the CdS bandgap causes significant changes in the EL pattern that could be explained by the induced photoconductivity of CdS.
- Irradiation makes the electrical current density distribution more uniform, which indicates diminishing of nonuniformity in electrical properties of the CdS layer detrimental for the cell performance.
- The effect of laser exposure on EL is long-lasting (hours-days. Analysis of observed long term transients along with similar studies at varying conditions of irradiation, injection level and temperature, can be useful for investigation of the photoconductivity mechanisms. Identification of defects involved (point defects, grain boundaries) and their transformation under illumination is an important goal for these studies.

### 1.9   Conclusions

- Spatially resolved measurements of electroluminescence (EL) on scales of several microns to centimeters is easy to perform on CdTe cells at various temperatures. These measurements demand only current densities of the order of $10^1 A/cm^2$. EL mapping is a very useful and informative method for revealing and studying lateral nonuniformities in solar cells/modules.
- EL mean intensity and pattern (bright spots on darker background) depends strongly on processing technology and cell stressing. EL is so sensitive to cell degradation that could be used for early predictions of the cell/module lifetime.
- Simultaneous studies of spatially resolved EL and PL from the same cell area allows distinguish nonuniformities in carrier transport from those in recombination rate as sources of nonuniformity in EL.
- Patterned doping with Cu and patterned $CdCl_2$ treatment demonstrated possibility to reveal nonuniformity in defect distribution and also strong influence of $CdCl_2$ on accommodation and manifestation of Cu atoms. Cu signatures are easy to detect with EL spectra. Cu distribution could be determined with EL scans.
- EL measurements on cells with the single- and bi-layer structure of front contact have shown that both back and front contacts influence non-uniformity in electron transport through the cell. Bi-layer front contact significantly reduces the nonuniformity.
- EL studies have provided and independent evidence of photoconductivity in the CdS layer and revealed long-lasting (hours-days) effect of exposure to a laser with the photon energy above the CdS bandgap. This provides a new method for investigations of the CdS photoconductivity mechanisms, e.g., identification of defects responsible for the photoeffect, their generation, transformation and migration under illumination.

**2. ADMITTANCE SPECTROSCOPY AND CAPACITANCE TRANSIENT MEASURE-MENTS AS METHODS FOR STUDYING DEEP ELECTRONIC STATES IN CdTe/CdS SOLAR CELLS**

## 2.1 Introduction.

Deep electronic states are a common concern for the developers and manufacturers of solar cells. First, these states may act as recombination centers, reducing the lifetime of photo-generated carriers, hence photocurrent collection and cell efficiency. This effect competes with the inevitable band-to-band recombination and is especially detrimental for the indirect gap semiconductors like Si, where the lifetime controlled by radiative band-to-band transitions is rather high. Direct gap semiconductors like CdTe are much less sensitive to recombination centers because their band-to-band lifetime is in the range of $10^{-8}$ s. Therefore the restrictions on the impurity content and structural defects concentration are less severe than for Si. However, in the case of thin film polycrystalline CdTe the material contains many structural defects. Indeed, the fine grain structure of the film (grain size of $\sim 1\mu m$) inevitably introduces a very high concentration of deep electronic states in the gap that could act as recombination centers.

Another aspect of the deep states problem arises when the concentration of traps, $N_t$, is comparable with or higher than the density of shallow levels that control the majority carrier concentration ("doping level"). In this case traps can significantly contribute to the space charge density in the depletion region, influencing the width of the region where the built-in electric field effectively separates photogenerated electrons and holes, providing higher photocurrent. Recent studies of thin film CdTe cells detected trap densities ($N_t \tau\, 10^{15}\, cm^{-3}$) higher than the "doping level" $N_{C-V}$ determined from C-V profiling, [14, 42-45]. Also high trap concentration can lead to the significantly overestimated doping level [46]. For CdTe the analysis and the estimates of possible errors were presented in [47].

Deep states of high density may considerably influence free hole concentration (Fermi level position) and its temperature dependence. We have already discussed the problem with respect to Cu doping effect in Sec. 1.3. SIMS measurements in CdTe:Cu based cells always indicate high Cu concentration, up to $10^{18}$ cm$^{-3}$. It is believed that Cu occupies mostly Cd sites, providing an acceptor state. However, the net "doping level" determined with C-V profiling is usually of the order of $10^{14}\, cm^{-3}$ at room temperature. Various models were proposed to explain this effect, such as Cu accumulation by grain boundaries while the concentration in the grain bulk is small or strong compensation of Cu acceptor states with the comparable concentration of donors. Another explanation may be that the Cu concentration in the grain bulk is high, but the resultant free hole concentration is much lower due to only partial ionization of these acceptors. Below we present results of modeling based on the assumption that the energy ionization of the level is $E_V + 0.35 eV$ (see e.g., [21, 48])
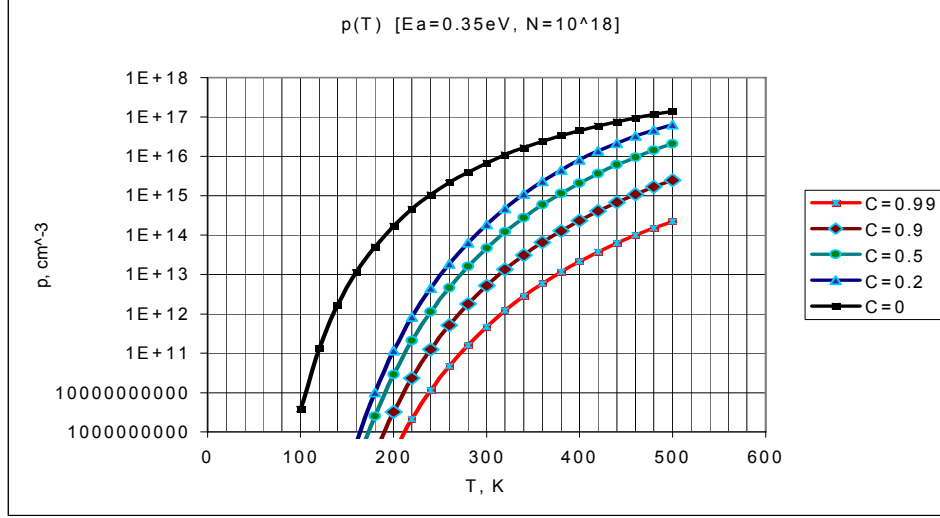
**Figure 2.1.** Hole concentration vs. temperature in CdTe for $E_a = 0.35 eV$, $N_A = 10^{18} cm^{-3}$, and varying compensation degree $C = N_D / N_A$

Important conclusions can be made based on the curves in the figure:

- For the assumed energy of the level, hole concentration at room temperature can be much lower than the acceptor density. The difference decreases at elevated temperature and rapidly increases with cooling.
- Even a moderate compensation considerably decreases ratio $p / N_A$, especially at lower temperatures.
- Even a slight variation of the compensation degree adjusts the modeled hole concentration to that measured one.

We have briefly discussed some aspects of the deep states problem to support the need to continue and further develop studies of deep states in CdTe thin film solar cells. However, our own experience and analysis of other investigations revealed numerous problems we have to solve to be successful. This urged us to review our previous results, revise experimental methods and approaches to the data interpretation, develop new instrumentation, measurement and data analysis procedures.

We begin (Sec. 2.2) with a description and discussion of the admittance spectroscopy (AS) method and modifications we have used for studying deep states in CdTe cells. Then we briefly discuss some results of our AS studies, mostly those that revealed the specific problems to be discussed in Sec. 2.3. The latter is devoted to the analysis of the problems we face when applying widely used AS methods or deep level transient spectroscopy, their technical limitations, and shortcomings of common theory used for the data interpretation. We discuss alternative approaches that can help, at least partially, to overcome the problems revealed by previous studies. In particular, we are focusing on measurements of transient effects, detecting and studying very slow, metastable states. Sec. 2.4 contains description of our recent developments in the technique of measurements aimed at realization of the alternative

approaches. Finally, in Sec. 2.5, we present and preliminary results obtained with a new measuring system.

## 2.2 Admittance Spectroscopy of Deep States in CdTe Based Cells.

### 2.2.1 Admittance spectroscopy (AS) basics

AS is based on the measurement and analysis of frequency dependent admittance/ impedance. Trap recharging (capture/emission of free carriers) caused by application of AC voltage to the diode (cell) leads to the appearance of AC current that has both out-of-phase and in-phase components providing correspondingly the imaginary and real parts of admittance, $Y$, and impedance, $Z$. LCR meters usually display the data in the "parallel, $p$," and "series, $s$," modes as $G_p = 1/R_p \equiv \text{Re}(Y)$, $R_s \equiv \text{Re}(Z)$, and $C_p \equiv \text{Im}(Y)/\omega$, $C_s \equiv [\omega \cdot \text{Im} Z]^{-1}$. The equivalent electrical circuit of a cell could be more or less complicated, therefore it is important to be cautious when extracting the trap related parts of capacitance, $C_t(\omega)$, and conductance, $G_t(\omega)$, from the raw data provided by LCR meter. Frequeny dependence of $C_t$ and $G_t$ arises from the finite rates of capture/emission processes. Each deep state (trap) has its own characteristic frequency $\omega_t$ (inverse characteristic time: $\omega_t = 1/\tau_t$) usually close to the emission rate. For a simple circuit: main diode + single level traps in the depletion region, the frequency dependencies are described by Eqs. (2.1-2.3) and illustrated by the following schematic figures

$$C(\omega) = C_d + \frac{C_t^o}{1 + (\omega/\omega_t)^2} \qquad (2.1)$$
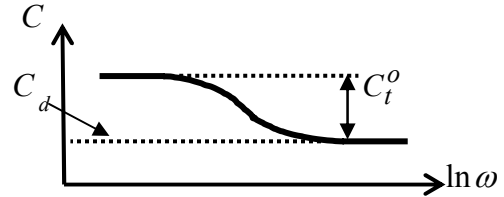


$$G(\omega) = G_d + \frac{G_t^o (\omega/\omega_t)^2}{1 + (\omega/\omega_t)^2} \qquad (2.2)$$
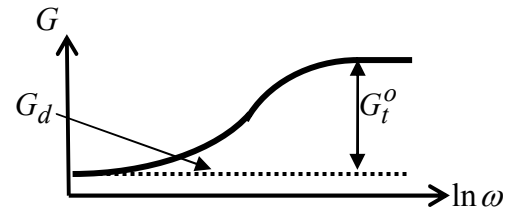


$$G_t^o = C_t^o \omega_t \qquad (2.3)$$

Here $C_t^o$ and $G_t^o$ are the maximum $C_t(\omega)$ and $G_t(\omega)$ values, while $C_d$ and $G_d$ are the parameters characterizing the same diode without traps. These four parameters can be determined by comparison the frequency dependences in the low frequency (LF) and high frequency (HF) limits, respectively at $\omega << \omega_t$ and $\omega >> \omega_t$:

$$C_d = C(\omega_{HF}); \ G_d = G(\omega_{LF}); \ C_t^o = C(\omega_{LF}) - C(\omega_{HF}); \ G_t^o = G(\omega_{HF}) - G(\omega_{LF}) \qquad (2.4)$$

The trap characteristic frequency can be determined from any of the four frequency dependent functions: $-\dfrac{dC}{d\omega} = \varphi_1(\omega)$; $\dfrac{dG}{d\omega} = \varphi_2(\omega)$; $-\omega\cdot\dfrac{dC}{d\omega} = \varphi_3(\omega)$; $G/\omega = \varphi_4(\omega)$. Each has a peak whose position is determined by the trap characteristic frequency:

$$\omega_{peak} = \omega_t / \sqrt{3} \text{ for } \varphi_1 \text{ and } \varphi_2; \quad \omega_{peak} = \omega_t \text{ for } \varphi_3 \text{ and } \varphi_4 \tag{2.5}$$

For $\varphi_4$ it is so if $G_D << G_t$, which is usually the case for our cells.

Which of the functions is more suitable to utilize depends on the properties of the main diode, trap characteristics, conditions of measurements, e.g. bias, light/dark conditions, etc. When the LF or HF limits are not available for the instruments in use, but the peaks in the $\varphi_i(\omega)$ dependencies are within the available frequency range, then the trap related parameters can be determined as $C_t^o = 2\omega_t \cdot \varphi_3(\omega_p)$ and $G_t^o = 2\omega_t \cdot \varphi_4(\omega_p)$ or, by similar analysis of $\varphi_1$ and $\varphi_2$.

The position of the trap energy level in the bandgap is usually derived from the temperature dependence of the characteristic frequency based on the equation (specified for the hole trap):

$$\omega_t = 2\sigma_t \cdot \langle v_{th}\rangle \cdot N_v \cdot \exp\left(\frac{E_t - E_v}{kT}\right) \tag{2.6}$$

where $E_t - E_v$ is the trap level energy with respect to the valence band edge, $\langle v_{th}\rangle \propto T^{1/2}$ is the average thermal velocity, $N_v \propto T^{3/2}$ is the effective density of states in the valence band and $\sigma_t$ is the trap capture cross section. If the Arrhenius plot $\ln(\omega_t / T^{-2})$ vs. $1/T$ provides a linear graph, then the activation energy $E_t - E_v$ is derived from the slope. The intercept of the extrapolated straight line with the $1/T$ axis provides the value of the product $\gamma \cdot \sigma_t$ where

$\gamma = \dfrac{N_v \cdot \langle v_{th}\rangle}{T^2} = \dfrac{16\pi \cdot k^2 \cdot m^*}{h^3} \approx 3\cdot 10^{21} \cdot \dfrac{m^*}{m_o}(cm^2 \cdot K^2 \cdot s)^{-1}$. Thus the only parameter we need to know is the effective mass. There is some uncertainty in the effective mass value we must use in calculations because of the complicated valence band structure in CdTe (degenerate heavy and light hole bands) as well as the spread in published values for both. However, if we use $m^* / m_o \approx 0.8$, the possible error should not exceed a few tens %. Other factors can dominate the error, e.g., nonlinear graph, errors in the extrapolation, etc. Uncertainty in the estimate of $\sigma_t$ within one order of magnitude could be considered acceptable.

To estimate the trap concentration from AS data, the simple theory for a single trap level, and uniform distribution of "doping level" $N$ and trap concentration $N_t$, provides an equation:

$$\frac{C_t^o}{C_d} = \frac{N_t}{N}\frac{1 - x_t / x_d}{1 + (N_t / N)\cdot(x_t / x_d)} \tag{2.7}$$

where $x_d$ is the depletion width and $x_t$ is the "crossing point", the distance from the interface where the deep level crosses the Fermi level, $E_t(x_t) = E_F$. For a small $x_t / x_d$ ratio, e.g. at forward bias, $C_t^o / C_d \approx N_t / N$. Thus, if one observes $C_t^o / C_d \geq 1$, that means that the trap density is higher than the "doping level". Indeed, sometimes we have observed a two- to threefold decrease in capacitance value with increasing frequency. It is hard to make more definite quantitative estimates because of the assumptions of the concentrations uniformity. In the case of small trap concentration ($N_t << N$), Eq. 2.7 takes a simpler form:

$$\frac{C_t^o}{C_d} = \frac{N_t}{N}\left(1 - \frac{x_t}{x_d}\right) = \frac{N_t}{N}\left(\frac{U_t}{U}\right)^{1/2} \tag{2.7a}$$

where $U = V_{b-i} + V_{bias}$ is the total band bending and $U_t \equiv (E_t - E_F)/e$.

## 2.2.2 Modifications of admittance spectroscopy

We have also used two modifications of AS for studying trap density of states in CdTe cells. As formulated, both methods can be applied not only to detecting and studying single levels or isolated trap levels, but also to study and quantitatively estimate continuous distribution of trap levels over energy.

***The first modification*** developed by Walter et al. [49] proposes the following equation for deriving the trap density of states, $D_t$, (DOS), from the capacitance frequency dependence:

$$D_t(E_\omega) = -A(U, E_F, x_d) \cdot \frac{dC}{d\omega} \cdot \frac{\omega}{kT} \tag{2.8}$$

Here $A$ is a coefficient that depends on the total band bending, $U$, Fermi level position in the quasi-neutral region, $E_F$, and depletion width, $x_d$. The energy $E_\omega$ is calculated as

$$E_\omega = kT \cdot \ln(2v_o / \omega) \tag{2.9}$$

where $v_o = \sigma_t \cdot \langle v_{th} \rangle \cdot N_v$ is the "attempt-to-escape" frequency.

For CdTe at T = 300 K, $v_o(s^{-1}) \approx 10^{26} \cdot \sigma_t(cm^2)$, e.g., $v_o \approx 10^{12} s^{-1}$ for $\sigma_t = 10^{-14} cm^2$. $E_\omega$ is the demarcation energy between trap states that can recharge under the AC voltage of frequency $\omega$ and those that are not able to follow oscillations of testing voltage. With increasing testing frequency $E_\omega$ shifts toward the valence band.

In the case of small trap concentration ($N_t << N$) and uniform doping level

$$A(U, E_F, x_d) = \left(\frac{N}{2e\varepsilon\varepsilon_o}\right)^{1/2} \frac{U}{U_\omega^{1/2}} \tag{2.10}$$

where $U_\omega = \dfrac{E_\omega - E_F}{e}$ .

The DOS function can be also derived from the conductance dependence on frequency:

$$D_t(E_\omega) = -A(U, E_F, x_d) \cdot \frac{d}{d\omega}\left(\frac{G}{\omega^2}\right) \cdot \frac{\omega^2}{kT} \qquad (2.11)$$

Thus, this method, contrary to the standard AS, can provide information not only on single trap levels that manifest themselves as peaks in the DOS function, but also on trap level bands and continuous distribution of deep states in the bandgap. It should be mentioned that single levels and bands could not be distinguished if the width of the latter does not exceed a few kT.

Since $E_\omega \propto T$, measurements at different temperatures widen the range of energies for which DOS can be determined. Integrating the measured DOS function over energy provides the concentration of various traps. Note that only defects located in the vicinity of the crossing point (trap level crosses Fermi level) contribute to the measured capacitance. With increasing trap energy, the crossing point moves toward the interface. Thus, $D_t(E_\omega)$ is actually determined at different locations. If the DOS function is spatially uniform, this method can provide exact and unambiguous information.

***The second modification***, drive level capacitance profiling (DLCP) method [50], is also aimed at determination of the trap DOS function. The method is based on measuring capacitance at a fixed frequency and makes use of the dependence of the measured capacitance on the amplitude of the AC testing voltage. As the amplitude $\delta V$ ("driving level") increases we obtain higher order on $\delta V$ corrections to the capacitance. At relatively small $\delta V$, $C \approx C_o + C_1 \delta V$ and the density of trap states can be determined as

$$N'_t(E_\omega) = -C^3 / (2e\varepsilon\varepsilon_o A^2 \cdot C_1) \qquad (2.12)$$

Here $E_\omega$ has the same meaning as before and is determined by Eq. 2.9. $N'_t(E_\omega)$ is the concentration of traps of energy below $E_\omega$ at the distance $x_{t\omega}$ from the interface where the Fermi level crosses the level $E_\omega$. Varying the applied DC bias voltage $V_{bias}$ can change the crossing point position. By measuring $C(\delta V)$ at different biases we can obtain information on the spatial distribution of $N'_t(E_\omega)$. Since $E_\omega$ depends on testing frequency and temperature, measurements of the same kind at varying frequency and temperature provide broader and more detailed information on the DOS function and its spatial variation. Again we must note that due to variation of $E_\omega$ hence $x_{t\omega}$ with frequency, the shape of the DOS dependence on energy could be determined correctly only if the DOS does not depend on distance. If it does depend, we face also the problem of uncertainty in location at which $N'_t(E_\omega)$ is measured. Measurements at varying bias, due to moving crossing point $x_{t\omega}$ can provide at most the trends in spatial dependence of DOS.

### 2.2.3   Some results of the AS application to CdTe cells

Admittance spectroscopy measurements at CSM were performed on cells fabricated with various processing techniques at various facilities (VTD, CSS - NREL, sputtering – UT).

Specifically, the effects of back contact, CdCl$_2$ treatment and etching of CdTe surface were studied with the cells based on the VTD material with all postdeposition processing steps provided at CSM. In nearly all cells a high trap concentration was found with non-uniform spatial distribution.

Fig. 2.2 shows typical frequency dependencies of capacitance and conductance measured on the FS/CSM cells with Cu/Au back contact. Measurements were done using two LCR meters; one for the frequency range of 20 Hz to 1 MHz and the other for 75 kHz to 30 MHz. Switching from one to the other sometimes introduced a small shift in displayed capacitance like that seen in the left figure. Compensating the shift provides a continuous graph with smooth variation of the slope. The shift is insignificant in the $G(f)$ dependence.
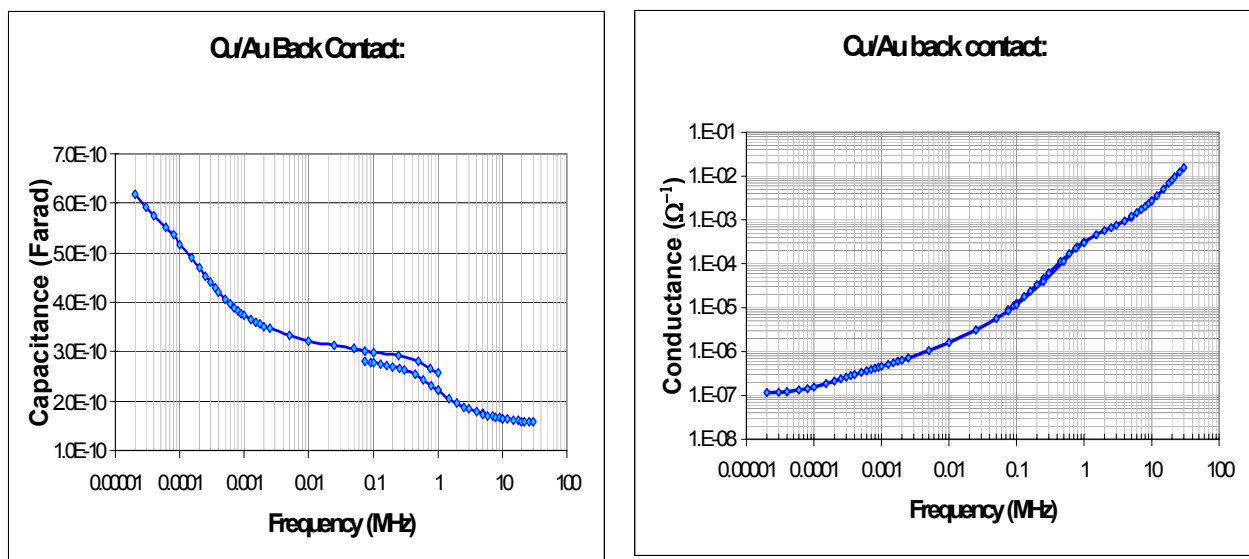


**Figure 2.2**. Capacitance and conductance of a VTD/CSM cell with the Cu/Au back contact measured at room temperature

The shape of both dependencies correlate with the trap concept and equations presented in Sec. 2.2.1. The capacitance value gradually decreases while the frequency increase several orders of magnitude. This suggests the presence of several types of traps or a continuous distribution of levels and characteristic times. The two-fold decrease in $C$ between 20 Hz and 100 KHz means that the total density of traps with characteristic times in the range of $\sim 10ms$ to $\sim 1.5\mu s$ , exceeds $N_{C-V} \approx 3 \cdot 10^{14} cm^{-3}$ for this cell measured at zero bias. Reduction of capacitance without saturation at higher frequencies indicates the presence of faster traps. The $C(f)$ dependence does not manifest any tendency to saturation at low frequency indicating the presence of slower traps ( $\tau > 8ms$ ).

To examine the slower traps we studied capacitance changes after switching the applied bias, which revealed long-term transients with characteristic times varying from seconds to minutes to hours. This may be at least partially attributed to changes in the space charge density caused by slow reoccupation of traps by carriers. Based on the theory of transients [46] we

estimated the concentration of slow traps responsible for the observed effects was $N_t^{slow} \tau 10^{15} cm^{-3}$.

The $(dG/df)$ vs. $f$ plot in Fig.2.3 demonstrates two peaks that could be attributed to single levels or relatively narrow trap bands of enhanced trap DOS.
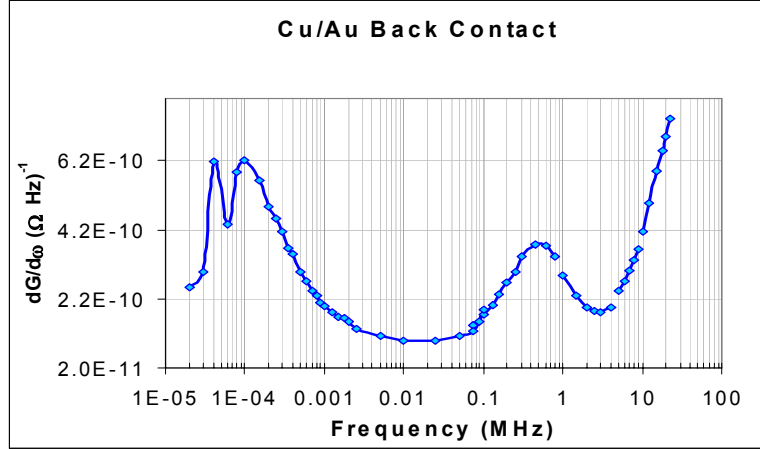


**Figure 2.3.** $(dG/df) - f$ plot has two peaks with characteristic times of 1.6 ms and 0.35 μs

The characteristic times derived from the peak frequencies are ~1.6 ms and ~0.35 μs. The trap concentrations estimated from the peak magnitudes are comparable to the "doping level" for both peaks. Application of the Walter/Herberholz method [49] (Sec. 2.2.2) showed the presence of the narrow band centered at the energy $E_\omega \approx (0.32\text{-}0.37)$ eV (depending on temperature). The maximum DOS value was $\sim 2 \cdot 10^{16} eV^{-1} cm^{-3}$. We estimated the total concentration of traps in the band as $\sim 1.5 \cdot 10^{15} cm^{-3}$.

Comparison of the results of AS for Cu/Au and Au-contacted cells demonstrates significant effects of Cu dopant. In particular, the high frequency peak ($\Delta E = (0.35 \pm 0.02) eV$) that is well pronounced in Cu-doped cells disappears in the undoped cells. Instead, a small peak at 100 kHz is seen. The decrease in magnitude and some shift in peak position was observed for the low-frequency peak (~ 100 Hz). Significant differences were noted in transients. Changes caused by stressing are also more significant for cells doped with Cu.

Effect of postdeposition treatment, specifically CdCl$_2$ treatment and etching of CdTe surface, on deep states in CdTe bandgap was studied by using a standard AS and DLCP (Sec. 2.2.2). The VTD/CSM cells were studied. Postdeposition treatments and ZnTe:Cu/Au back contact were applied at CSM. Averaged characteristics of differently treated cells are presented in Table 1. Results of AS measurements for typical cell of each type are shown in Fig. 2.4.

The table shows that a significant trap density belongs to the energy range between 0.4 and 0.6 eV; the deeper trap concentration is high at all depths. For all types of cells the estimated trap density is greater than the "C-V doping level". Cells A and B with the highest efficiency both

have high trap concentration, while the least efficient cells D (without CdCl$_2$ and etch) have a much smaller trap concentration.


**Table 2.1.** Characteristics of cells with different postdeposition procedures

| Cell type | CdCl$_2$ treated | Etch | Eff., % | N$_{cv}$ *) 10$^{14}$cm$^{-3}$ | | Density of traps (10$^{14}$cm$^{-3}$) for E$_t$<E$_\omega$**) | | | | | |
|-----------|------------------|------|---------|--------------------------------|--------------------|------|------|------|------|------|------|
| | | | | | x, μm | ~2.3 | | ~1 | | ~0.15 | |
| | | | | | E$_\omega$***⁾eV | 0.6 | 0.4 | 0.6 | 0.4 | 0.6 | 0.4 |
| A | Yes | Yes | 10.8 | 2.3 | | 20 | 10 | 25 | 7 | 35 | 9 |
| B | Yes | No | 10.5 | 3.1 | | 25 | 10 | 20 | 8 | 20 | 8 |
| C | No | Yes | 8.6 | 1.9 | | 30 | 8 | 20 | 5 | 25 | 5 |
| D | No | No | 6.2 | 0.75 | | 10 | 6 | 7 | 3 | 8 | 3 |

*⁾ Doping level at the depth x=1.5μm (from C-V profile at f=100 KHz)
**⁾ Obtained with drive level capacitance profiling (DLCP)
***⁾ Approximate values
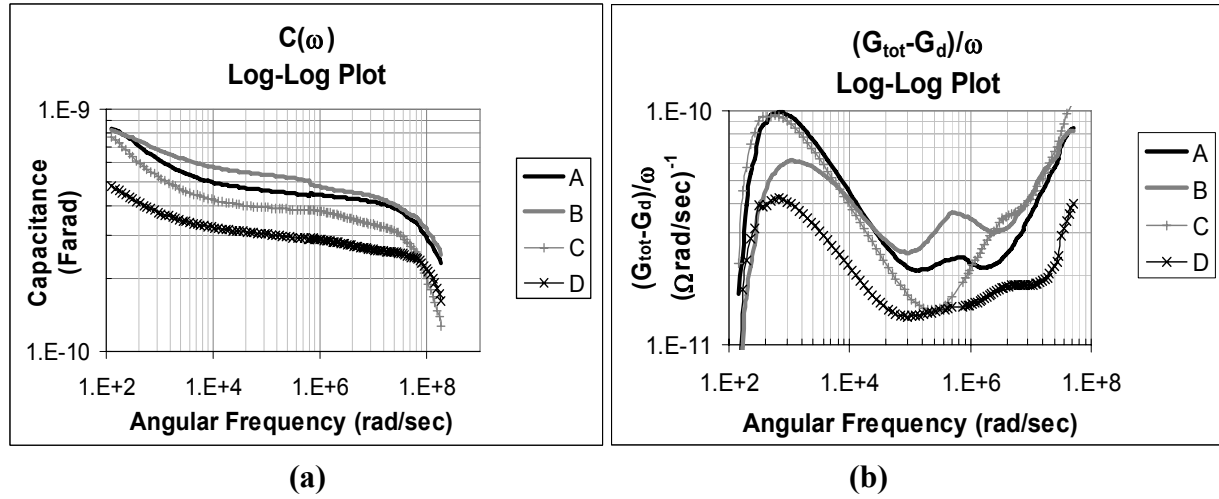


**Figure 2.4** Results of AS measurements on cells with different postdeposition treatments (see A, B, C, D in Table 2.1)

The results of the standard AS measurements confirm the DLCP results. A significant (about two times) decrease in capacitance (Fig. 2.4.a) means that the total trap concentration in the characteristic time range from 10 ms to 1 μs exceeds the doping level. Peaks in Fig. 2.4.b reveal the existence of several distinct trapping levels or bands with widely varying characteristic frequencies ($\omega_{peak} = \omega_t$). Assuming the "attempt-to-escape" frequency $\nu_o$ value of $10^{12} s^{-1}$ the trap energy was estimated: for the lower frequency peaks ($\omega_{peak}\sim5\times10^2 s^{-1}$) E$_t$-E$_v \sim$ 0.6eV; for the higher frequency peaks ($\omega_{peak}\sim10^6$ s$^{-1}$), E$_t$-E$_v \sim$ 0.4eV. The CdCl$_2$ treatment (cells A and B) increases concentration of states in both bands. For cells C and D (without CdCl$_2$) the peaks at

$\omega_{peak} \sim 8 \times 10^5 \, s^{-1}$ are not clearly visible. Instead, peaks appear close to $2 \times 10^6 \, s^{-1}$. The influence of etching on the conductance spectra is well seen for these two samples.

Differences in trap concentrations and depth profiles were also revealed by DLCP measurements on traps prepared with different CdTe deposition techniques (VTD, NREL, UT). For all cells, trap density was minimal in the vicinity of the depletion edge and increased toward the interface and back contact. The highest trap density $1 \cdot 10^{16} \, cm^{-3}$ was found in the UT cell at reverse bias. The VTD cell maximum density was around $1 \cdot 10^{15} \, cm^{-3}$. For the NREL cell it was in the range of $(4-6) \cdot 10^{15} \, cm^{-3}$.

### 2.2.4. Summary

The standard admittance spectroscopy and its modifications (Walter et al. [49] and DLCP [50]) applied to studies of thin film CdTe cells provided mutually complementary and consistent information on deep electronic states in CdTe. The main results are:

- In all cells manufactured at different facilities, a high trap concentration was found, sometimes several times greater than the "C-V doping level".
- At least two narrow bands of deep states were detected in the energy range of $0.33-0.4eV$ and $0.57-0.63eV$. There was evidence of a significant amount of deeper/slower traps ($\tau > 10ms$) and much slower traps that are not detected with our LCR meters.
- Concentration of traps and their spatial distribution depend on CdTe deposition technique and postdeposition treatment. Significant changes were caused by doping with Cu and stressing.
- No evidence of detrimental effect on cell performance due to enhanced trap concentration was found for the traps detected in these studies ($\tau < 10ms$, $E_t - E_V \, \delta \, 0.6eV$).

### 2.3. Some Problems and Possible Approaches to Their Solution

### 2.3.1. Effect of high trap concentration

The analysis of results of AS and DLTS measurements usually is based on equations valid for small trap concentration: $N_t << N$. As shown in the previous section, CdTe thin film cells have rather high trap concentration. In particular, both narrow bands detected by AS contain density of states exceeding the "C-V doping level". To illustrate complications caused by high trap concentrations, let us consider a simple model of a single trap level while $N_t(x) = const$. For $N_t << N$, the $N_t$ value can be determined from the $C(\omega)$ dependence, if $N$ (hence $E_F$) and the trap level $E_t$ are already known, by using an equation from Sec. 2.2.1:

$$\frac{C_t^o}{C_d} = \frac{N_t}{N}\left(\frac{U_t}{U}\right)^{1/2} \tag{2.7a}$$

where $U = V_{b-i} + V_{bias}$ is the total band bending and $U_t \equiv (E_t - E_F)/e$.
The equation for an arbitrary trap concentration, Eq. 2.7, can be presented in a similar form

$$\frac{C_t^o}{C_d} = F(t,b) \cdot \frac{N_t}{N} \left(\frac{U_t}{U}\right)^{1.2} \tag{2.13}$$

with the correction factor

$$F(b,t) = \sqrt{\frac{1+t(1-b)}{b}} \tag{2.14}$$

where $b \equiv U_t / U$ and $t \equiv N_t / N$.
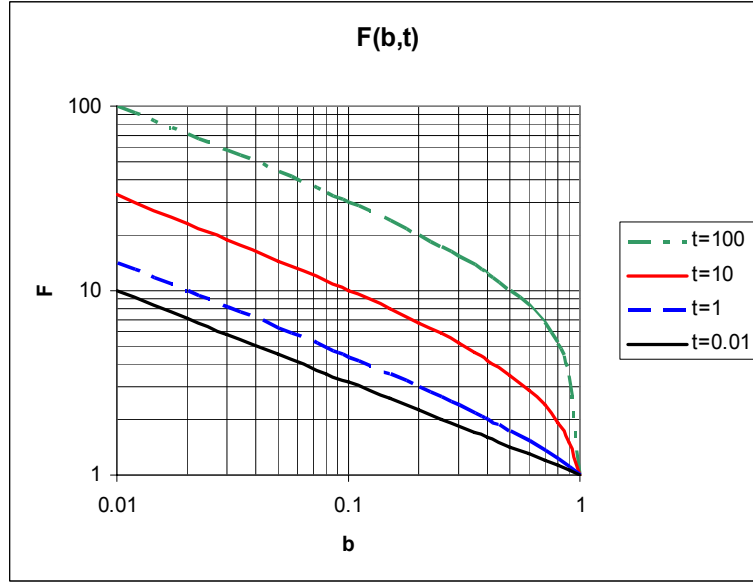


**Figure 2.5** Correction factor $F(b,t)$ in Eq. 2.13

It is seen from the figure that commonly used equation (2.7a) can lead to underestimation of trap concentration, especially significant if the Fermi level is located close to the trap level (small $b$). The error increases with the $N_t / N$ ratio growth. It should be noted that the Eqs. 2.8 and 2.10 used for the determination of trap density of states when applying modified AS, also should be corrected in a similar way for a high trap concentration.

### C-V Profiling in the presence of high trap concentration

We also face another problem when using common theory for estimating trap density from AS measurements. Equations 2.7 and 2.10, corrected or not, allow us to estimate not the trap concentration itself but the ratio $N_t / N$. Thus to estimate trap concentration or DOS function we need to first determine the "doping level" which is usually derived from C-V measurements. But in the case of high trap concentration the common C-V data treatment procedure can provide incorrect $N$ profiles with an overestimated doping level.

C-V profiling is usually performed with the testing signal frequency as high as possible to exclude the trapped charge oscillations contribution in the measured capacitance. It can be done if the testing frequency is higher than the characteristic frequency of all traps so that the trapped

charge cannot follow the voltage oscillations. If this condition is satisfied, measured capacitance is determined by the depletion width. Specific capacitance (per unit area of a cell) is

$$C = \frac{\varepsilon\varepsilon_o}{x_d} \qquad (2.15)$$

The common approach to the C-V profiling assumes that a change in space charge in the depletion region $\delta Q$ due to small change in bias $\delta U$ is due only to the shift of the depletion edge $\delta x_d$, hence

$$\frac{dC}{dU} = \frac{dC}{dx_d}\frac{dx_d}{dU} = -\frac{\varepsilon\varepsilon_o}{x_d^2}\frac{dx_d}{dU} \qquad (2.16)$$

The space charge density at the depletion edge is $\rho(x_d) = -eN(x_d)$, therefore the change in voltage across the depletion region is

$$\delta U = -\delta\left\{\frac{1}{\varepsilon\varepsilon_o}\int_o^{x_d} x\rho(x)dx\right\} = \frac{e}{\varepsilon\varepsilon_o}N(x_d)x_d\delta x_d$$

and

$$\frac{dx_d}{dU} = \frac{\varepsilon\varepsilon_o}{e\cdot N(x_d)\cdot x_d} \qquad (2.17)$$

The well known equation to derive the doping profile from C-V measurements is

$$N(x_d) = -\frac{C^3}{e\varepsilon\varepsilon_o}\left(\frac{dC}{dU}\right)^{-1} = \frac{2}{e\varepsilon\varepsilon_o}\left(\frac{dC^{-2}}{dU}\right)^{-1} \qquad (2.18)$$

Eq. 2.17 is approximately correct only for a low trap concentration. However, small change in the DC bias applied to a cell not only shifts the depletion edge, but shifts the crossing points of all trap levels as well, $\delta x_{ti} = \delta x_d$. If the trap is able to follow the bias changes, this leads to changes in trapped electrical charge. As pointed by Kimmerling [51], the total time of C-V profiling, as well as the time spent for applying the bias increment and measurements at a new bias, can be much longer than the characteristic time of a trap. In other words, the characteristic time of the bias change, $\theta$, can be (and usually is) much longer than $\tau_t = \omega_t^{-1}$ and $\omega^{-1}$. This means that, if the trapped charge does not oscillate, it however follows the changes in DC bias. The effect under discussion has been confirmed by numerous observations of the hysteresis loops in C-V profiles, and correspondingly in $N(x)$ profiles, usually more significant in the latter.

Changes in space charge density within the depletion width influence the $dx_d/dU$ value as illustrated by Eq. 2.19 derived for the multi-level model:

$$\frac{\delta x_d}{\delta U} = \frac{\varepsilon\varepsilon_o}{e}\left\{x_d N(x_d) + \sum_i x_{ti} N_{ti}(x_{ti})\right\}^{-1} \qquad (2.19)$$

where summation is over all traps with $\tau_t < \theta$. By replacing Eq. 2.17 with 2.19 we obtain the equation for the "apparent" doping level, $N'$, derived from C-V measurements with the common procedure:

$$N'(x_d) = \frac{2}{e \varepsilon \varepsilon_o} \left( \frac{dC^{-2}}{dU} \right)^{-1} = N(x_d) \left\{ 1 + \sum_i \frac{x_{ti}}{x_d} \frac{N_{ti}(x_{ti})}{N} \right\} \qquad (2.20)$$

To evaluate possible effect of traps on the "C-V doping profile" we have calculated the apparent doping level for a two-trap-level model with trap energy $E_{t1} = 0.4eV$ and $E_{t2} = 0.6eV$, close to those detected in CdTe using AS (see Sec. 2.2.3). The characteristic times determined for these two traps, $\tau_1 \sim 10^{-6}s$ and $\tau_2 \sim 10^{-3}s$, are shorter than the "delay time" provided by our LCR meters, which means that the trapped charge follows DC bias changes. The model was simplified by the assumption that the real doping level and trap concentrations are spatially uniform. The results are shown in Fig. 2.6 for the real doping level varying in the range $10^{13} cm^{-3} \leq N \leq 3 \cdot 10^{14} cm^{-3}$, and two sets of trap concentrations, consistent with the concentrations estimated in Sec. 2.2.3: (1) $N_{t1} = 3 \cdot 10^{14} cm^{-3}$, $N_{t2} = 1 \cdot 10^{15} cm^{-3}$ and (2) $N_{t1} = 1 \cdot 10^{15} cm^{-3}$, $N_{t2} = 3 \cdot 10^{15} cm^{-3}$.
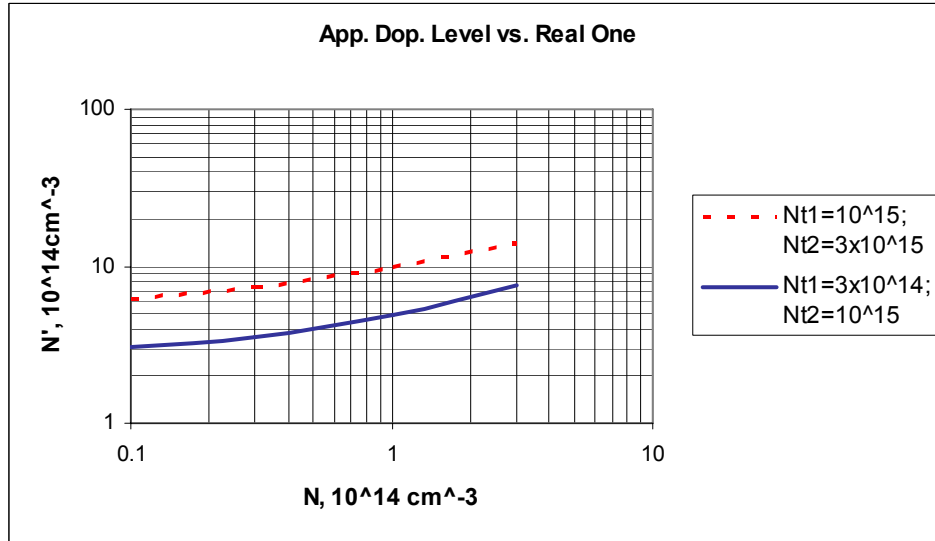


**Figure 2.6** Apparent doping level versus the real one for the two-trap-level model.

The main features of the apparent doping level, $N'$, seen from the figure are:
- $N'$ could be significantly higher than the real doping level $N$ for high trap concentration
- $N'$ varies much less than $N$. In our calculations a 30x increase in $N$ is accompanied with only a two- to threefold increase in $N'$.

- The apparent doping level, calculated for trap density not exceeding the values determined experimentally, is in the range of $3 \cdot 10^{14} - 1 \cdot 10^{15} \, cm^{-3}$, which is close to what is thought to be the carrier concentration/doping level in thin film CdTe cells. However, we can say nothing certain about the real doping level/free hole concentration based only on C-V measurements.

To cope with the problems discussed above we have been working in two directions:
1. Experimentally obtaining more detailed and reliable information on trap energy level/bands, characteristic times, estimated concentration (or DOS function). To do this we have developed a new system (see Sec. 2.5) and significantly broadened conditions of measurements, such as temperature range, time of monitoring, bias, light intensity and spectrum, etc. AS, C-V profiling and J-V measurements are accompanied by measurements of transients caused by bias switch and illumination in the time range from seconds to hours and days.
2. Modeling cell characteristics, including J-V, C-V, C(f), and transients. The more detailed information we get from experiment and the greater the number of characteristics we model, the more reliable estimates we can make of the trap properties.

### 2.3.2 Technical limitations on the characteristic time of traps available for detection and studies.

The LCR meters in use limit the frequency range of admittance spectroscopy. In particular, our LCR meters nominally provide measurements in the range of 20Hz to 30MHz, but in reality the range is narrower due to the impact of parasitic effects and noises in the vicinity of upper and lower frequency limits. Another limitation on high frequency range comes from the cell series resistance, which in combination with the cell capacitance provides features in the admittance-frequency dependence similar to those due to traps. [52]. For a well developed back contact Schottky diode this feature's frequency is temperature-dependent with an activation energy in the range of ~hundreds of meV.

Thus, the AS capabilities to detect and study deep traps are confined to traps with characteristic times in the range of $\tau \sim 10^{-2}$ to $\sim 10^{-6} \, s$. The major problem is to extend the higher $\tau$ limit up to seconds, minutes and hours because there is evidence of a significant amount of very slow traps in our cells. The progress in this direction is strongly limited by electronic devices capabilities and principal difficulties of electrical measurements at very low frequencies. For example, accurate measurement of admittance at a single frequency such as 0.01 Hz will take at least tens of minutes, and measurements of frequency dependence in this range – many hours. More feasible solution of the problem is to use the temperature dependence of the trap characteristic time and bring $\tau$ into the range available for LCR meter. Indeed, for deep levels characteristic time is thermally activated and exponentially depends on temperature: $\tau(T) \propto T^{-2} \cdot \exp(E_t / kT)$. The ratio $\tau(T)/\tau(300K)$ presented in Table 2.2 shows that if the characteristic time is too short at room temperature for a deep level with $E_t = 0.3eV$, it could be increased ~100 times with cooling to T=220K and much more by further cooling. Conversely, very long $\tau(300K)$ for deeper levels like $E_t = 0.8eV$ can be made ~100 times faster at T=350K

Another approach to study slow traps, especially very slow ones, is to study and analyze admittance transients with characteristic times in the range of seconds, minutes, hours, days. The most unambiguous information on trap characteristic time and density can be derived from measurements and analysis of capacitance transients. Traps with the characteristic time in the range 10 ms $\delta\tau$ $\delta$ 10s at room temperature, not detectable by AS and not suitable for the transient studies, could be brought to the desired range by cooling. Since traps of this kind demonstrate high activation energy, we do not need too deep cooling (Table 2.2). Thus, combining AS and transient measurements with temperature variation allows the trap detection and studies in the whole reasonable range of characteristic times.

**Table 2.2.** Dependence of the characteristic time on temperature: $\tau(T)/\tau(300K)$

| T, K | $\tau(T)/\tau(300K)$ | | | |
|------|--------------|--------------|--------------|--------------|
|      | $E_t = 0.3eV$ | $E_t = 0.4eV$ | $E_t = 0.6eV$ | $E_t = 0.8eV$ |
| 350 | 0.14 | 0.08 | 0.027 | $8.8 \times 10^{-3}$ |
| 300 | 1.0 | 1.0 | 1.0 | 1.00 |
| 260 | 7.7 | 14 | 50 | $1.6 \times 10^2$ |
| 220 | $1.3 \times 10^2$ | $5.3 \times 10^2$ | $9.1 \times 10^3$ | $1.5 \times 10^5$ |
| 185 | $3.6 \times 10^3$ | $4 \times 10^4$ | $5.0 \times 10^6$ | ---- |
| 160 | $9.1 \times 10^4$ | $2.7 \times 10^6$ | ---- | ---- |
| 140 | $2.7 \times 10^6$ | ---- | ---- | ---- |

### 2.3.3 Capture cross section. Very slow traps.

Analysis of $\omega_t(T)$ data based on Eq. 2.6 and the Arrhenius plot, $\ln(\omega_t/T^{-2})$ vs. $1/T$, is aimed at determination of the trap level distance from the band edge, $E_t$, and the capture cross section value, $\sigma_t$. The treatment of the data is based on the assumption that the capture cross section is temperature independent, which sometimes is not true. Even if the Arrhenius plot provides a straight line graph, the activation energy derived from the slope is not necessarily equal to $E_t$. Capture cross section can itself depend on temperature exponentially

$$\sigma(T) = \sigma_\infty \cdot \exp\left(-\frac{E_\sigma}{kT}\right) \qquad (2.21)$$

In this case the activation energy is the sum of two energies ($E_a = E_t + E_\sigma$) and is used only as a "signature" of a specific trap but does not provide an estimate of the trap level position. At the same time, the common procedure to derive $\sigma_t$ from the y-intercept actually estimates the value of $\sigma_\infty \equiv \sigma(T \to \infty)$, but not the real cross section at finite temperature. An approach to determine $\sigma(T)$ and separate $E_\sigma$ and $E_t$ from DLTS measurements by varying the filling pulse time is presented in [46]. For example, application of this approach to InGaAsN alloys [53] suggested that $\sigma$ (T) follows Eq. 2.21 with the capture rate activation energy $E_\sigma \approx 0.4eV$. The real capture

cross section turned out orders of magnitude higher than that determined from the y-intercept. This kind of $\sigma(T)$ dependence is usually explained based on the model of a Coulomb-repulsive center having a potential barrier.

***Very slow traps***

The deeper the level the higher the trap characteristic time. For example, at T=300K, $\tau \approx 1.5s$  for $E_t = 0.7eV$ and $\sigma = 10^{-14} cm^2$. But the capture cross section is another factor that can make a trap slow or even "very slow". We will discuss here two possible mechanisms for the extremely slow capture rate, hence very low capture cross section. Both are based on the essentially inhomogeneous distribution of traps, namely traps gathered in clusters or traps belonging to the grain boundaries.

Cluster model

The cluster model proposed in [54] for $\alpha - Si$ was recently used for very slow capacitance transients in CuInGaSe$_2$/CdS cells [55]. It is common to determine $\sigma$ from DLTS by measuring the density of trapped charge $N_f$ as a function of trap-filling pulse duration, $t_p$. Common theory predicts the dependence

$$N_f(t_p) = N_t \left[ 1 - \exp\left( -\frac{t_p}{\tau_t} \right) \right]$$

(2.22)

with saturation on the $N_t$ level when all traps are filled. In [55] unusually long pulses were used, up to $\sim 10^3 s$. Measured change in capacitance indicated trapping of majority carriers and demonstrated a logarithmic growth with pulse length in the five-decade range of $\sim 10^{-3} s \le t_p \le \sim 10^2 s$. An apparent saturation of the signal occurred only at $t_p \ge 10^2 s$. The explanation, as in [54], is that the potential barrier for free carriers created by the collective action of closely spaced charged traps is much higher than that for a single trap. This barrier increases with the trap filling in the cluster, providing stronger repulsion of carriers and reducing the effective capture cross section. Theoretical analysis of the model leads to an equation that fits the experimental results in [55]

$$\frac{\Delta C}{C_o} = A_o \ln\left( 1 + t_p / t_o \right)$$

(2.23)

where $A_o = \dfrac{kT}{2N_t \cdot e \cdot f}$ ; $t_o = \dfrac{2A_o}{n_o \cdot \langle v_{th} \rangle \cdot \sigma_t}$ ; $n_o$ is the free carrier density beyond the region occupied by the cluster potential. The cluster potential is $\Phi = N_s \cdot f$, where $N_s$ is the density of carriers captured at $t = t_p$, and $f$ is the model-dependent coupling factor. Theory also fits the data previously obtained for $\alpha$ -Si solar cells, Ge$_{0.3}$Si$_{0.7}$/Si heterojunctions and plastically deformed GaAs (see references in [54]). For CuInGaSe$_2$ cells of various In/Ga ratios studied in [55], the $t_o$ values were in the range of $10^{-4}$ to $10^{-2}$ s. Trap densities determined from the region, where $\Delta C(t_p)$ saturated, were rather high, from $4 \cdot 10^{15}$ to $\sim 2 \cdot 10^{17} cm^{-3}$, close or

greater than the "C-V doping level". Assuming uniformly charged spherically shaped clusters of radius $R$ (coupling factor $f = eR^2/3\varepsilon$ f), the authors estimated $R \approx 9 - 55 nm$ and $\sigma_t \approx 4 \cdot 10^{-22}$ to $3 \cdot 10^{-23} cm^2$. The authors recognize that the capture cross sections are surprisingly small but they have not yet proposed an unambiguous explanation.

Grain boundaries (GB)

It is mentioned in [55] that "the calculated radial dimensions of the hypothetical charging spheres are of the same order of magnitudes as the smallest polycrystalline 'grains'… This dimensional coincidence may imply that the charging is taking place at the surface of the grains."

We have recalculated the radius values using the same data and found that they are of the order of hundreds of nanometers, which makes the grain boundaries model even more probable. However the analysis carried out in [55] for the charged spherical trap clusters, should be revised with respect to two dimensional grain boundaries. We have done that and made some estimates for CdTe based on the information we obtained previously when studying the GB electronic properties in CdTe thin films [56-58].

The CdTe films were deposited on glass substrates at IEC (physical vapor deposition) and FS (vapor transport deposition). Some films were treated with CdCl₂ and doped with Cu at CSM. We also studied films prepared at NREL with a close space sublimation method. Those films were deposited on CdS/TCO/glass substrates and underwent a standard postdeposition treatment. Then they were lifted-off from the device and mounted on a glass substrate.

By using impedance spectroscopy [57, 58] we were able to separate and independently study individual contributions of grain boundaries (GB) and intragrain (IG) material in film resistance and capacitance: $R_{GB}, R_{IG}, C_{GB}$ and $C_{IG}$. Major results for all films:

- The $R_{GB}$ values are orders of magnitude greater than $R_{IG}$.
- Positive charge captured by grain boundary states provided a potential barrier for holes. The estimated barrier height $\Phi$ varied in dark from 0.3 to $0.8 eV$ depending on post-deposition treatment and doping.
- Illumination could decrease $R_{GB}$ significantly by reducing barrier height.
- Doping with Cu reduces dark $R_{GB}$ by more than two orders of magnitude. Potential barrier thickness $W$ (depleted thickness) estimated from capacitance was of the order of 200-500Å in the Cu-doped films.
- Space charge density in the depleted layer adjacent to GB calculated based on $\Phi$ and $W$ turned out to be very high: $\rho/e \sim 10^{17} cm^{-3}$, sometimes up to $10^{18} cm^{-3}$. This indicates that the doping level $N = N_A - N_D$ in vicinity of GBs is much higher than $N_{C-V}$. The same result was obtained in [38] from measurements and modeling the $R_{GB}(T)$ dependencies.
- Integrated density of charged states per unit GB area $D_{GB}$ estimated from the $C_{GB}(V_{bias})$ studies is in the range of $\sim 10^{12} - 10^{13} cm^{-2}$.

The following important conclusions from these results are relevant to the problem of slow traps and their contribution to the transients observed in CdTe cells:

- The GB state density per unit volume $N_{GB}$ is high. For cube-shaped grains with a grain size $d$, $N_{GB} = 3(D_{GB}/d)$. For $d = 1\mu m$ and $D = 10^{13} cm^{-2}$, $N_{GB} = 3 \cdot 10^{17} cm^{-3}$.

- The GB repulsive potential barrier makes capture cross section (CCS) for holes very low. CCS for a single deep state in the neutral GB, $\sigma_{GB}^{o}$, should be multiplied by a Boltzmann factor $\exp[-\Phi/kT]$ for electrically charged GB with a potential barrier height of $\Phi$. For example, assuming $\sigma_{GB}(\Phi = 0) \approx 10^{-16} cm^2$ (reasonable value for the neutral defect), we obtain $\sigma_{GB}$ ( $\Phi = 0.3eV$) $\approx 1 \cdot 10^{-21} cm^2$ and $\sigma_{GB}$ ( $\Phi = 0.5eV$) $\approx 4 \cdot 10^{-25} cm^2$ at room temperature.

- Since the potential barrier increases with the density of charged GB states, $N_{GB}^{+}$, the capture cross section, hence the capture rate, reduces rapidly with the number of trapped holes. For a charged plane (like GB), $\Phi \propto Q^2 = f \times (eN_{GB}^{+})^2$. A small change in the amount of trapped holes provides a change in the barrier height of

$$\delta\Phi \approx 2\Phi(N_{GB}^{+})(\delta N_{GB}^{+}/N_{GB}^{+}) \tag{2.24}$$

Thus, if we start with $\Phi = 0.5eV$ and then increase density of trapped holes by 10%, the potential barrier grows by 0.1eV and the capture rate decreases 50x at T=300 K. A 20% increase will reduce the rate about two thousand times. That means that we should not expect any significant change in the GB states occupation in any reasonable time of observation of capture process, say in hours or even days.

- It is easy to show that the kinetics of trap filling for reasonable time (small changes in $N_{GB}^{+}$) is described by the equation similar to Eq. 2.23: $N_{GB}^{+}(t) \propto \ln[t/t_o + 1]$. That increases the probability that the long term transients in capacitance observed in CIGS cells in [55] were due to filling GB states.

- The potential of the positively charged GB is repulsive for holes but attractive for electrons. Therefore the GB capture cross section and the capture rate for electrons is orders of magnitude higher than for holes, as seen in our studies of photoconductivity of CdTe polycrystalline films. Conductivity increases rapidly and greatly with illumination, due to the reduction of the potential barrier caused by a decrease in the GB positive charge. The latter is provided by capturing of photogenerated electrons that recombine with holes trapped by GB states. After the light was switched off, restoration of the film resistance takes hours. In a wide time range (from ~10s and not close to saturation) the time dependence of the resistance change is $\Delta R \propto \ln t$ which means that slow capturing traps are the major mechanisms of potential barrier restoration. The rate of capturing reduces with time of observation.

- These are all grounds to expect manifestation of the GB deep states in transients measured on CdTe solar cells. Analysis of the data will be complicated due to presence of both hole and electron capture/emission processes. GB provides acceptor-like and donor-like states in the gap, thus hole- and electron-traps. Detailed studying of transients can provide additional information about the GB electronic properties and their dependence on cell processing and degradation. It would be useful to compare results of studies on cells with those conducted on CdTe films, especially extracted from the cells with the lift-off technique.

### 2.3.4 Transients.

In previous sections we considered transients mostly as an additional tool for detecting and studying deep states. But the problem could be viewed from another, more fundamental, side. What are the mechanisms of transients in electrical and photoelectric characteristics that were being observed in CdTe cells for a long time but not studied thoroughly so far? Can studies of transients provide better understanding of basic issues behind cell performance and stability, for example, identify the defects effecting electronic properties of a cell, migration and mutation of these defects, their influence on cell degradation, etc.?

Strong support to the necessity of the systematic transient studies is provided by discussion of this subject (March 2002) initiated by Ken Zweibel. E-mail messages exchanged between members of CdTe team (26 messages in a week) helped to better understand the current status of transient studies in CdTe, to discuss definitions, in particular the terms "transients" and "degradation", to formulate the problems, and discuss some possible approaches to their solution.

One obvious problem is the influence of transients on cell characterization results. Since it is impossible to avoid the effect of transients, we must develop the procedures of measurement and data treatment that minimize their impact. As a first step, the CdTe Team needs to standardize conditions of measurements, which will make comparable the results obtained at various facilities. Transients manifest themselves not only in J-V characteristics. As the examples we can refer to the problem of C-V profiling in the presence of slow traps considered in Sec.2.3.1 or transients in conductivity of thin films (Sec. 2.3.3). Before developing standardized procedures of measurements and data treatment we need to study in detail and better understand transients of various characteristics of devices and materials of interest.

Transients can be caused solely by changes in trap occupation as well as by generation, mutation and migration of defects, and also by combination of these mechanisms. Discriminating these two mechanisms is an important but not simple problem, and cannot be solved based only on significantly different characteristic times of the processes or their reversibility.

The discussion mentioned above has shown that the whole CdTe National Team considers transients in CdTe cells as an important problem that should be addressed in the basic studies. At the same time it was mentioned more than once that there has been a lack of studies of this kind and information we have is far less complete and detailed than say for amorphous silicon. The publications on CdTe by Sasala & Sites [59, 60] and by MacMahon [61] should be mentioned. All three are devoted to transients in J-V characteristics at varying temperature due to light or bias switch. Some non-systematic data on capacitance transients can be found, mostly on hysteresis in C-V profiles.

Publications on capacitance transients in amorphous silicon provided vast information on metastable effects/defects in this material. Capacitance transients are mostly due to slow changes in the space charge density after switching bias or light. Therefore interpretation is easier than for transients in J-V dependencies or photoconductivity. From the magnitude of change in capacitance one can estimate the charged defect density, no matter whether these changes are due to change in filling existing traps or generation of new atomic/structural defects. The sign of the transient allows discrimination of majority- and minority-carrier traps. The capacitance magnitude and time dependence studied at various temperatures provide the characteristic time

of traps, their energy levels, capture cross section, concentration or DOS function in the case of continuous distribution of states. If transients are due to generation of new defects or their mutation, the activation energy of the processes can be derived from the $C(t,T)$ dependencies.

Capacitance transients in differently processed cells, both as-prepared and stressed, are an important part of our studies. We believe that these studies combined with intentional variations in deposition and postdeposition procedures, in sort, amount and method of introducing of dopant, and accompanied with structural and compositional studies, can also provide significant progress in identification of defects responsible for specific electronic states. The current situation is far from being perfect. Indeed, in many cases different authors attribute the same (or almost the same) energy level to different defects, even if the level is determined with the same method. Conversely, different levels are ascribed to the same defect. Frequently, a significant discrepancy is seen in the energy of the same state/defect obtained by measurements and theoretically. A good example is a variety of energy levels ascribed to the Cu substitute for Cd. It should be mentioned that the problem of identification is even more severe for polycrystalline CdTe, where manifestations of the same defect can differ to some extent for locations in the grain bulk and in the GB region.

## 2.4    New System for Measuring Admittance in a Wide Temperature Range

To realize the program of studying deep states with electrical methods a new measurement system has been built. It is designed to provide admittance spectroscopy (AS) measurements at different biases, capacitance-voltage profiling (CV), current-voltage characterization (JV), and measurements of transients (Tr) in all characteristics listed above. All measurements can be conducted at various temperatures, in dark and under illumination.

The experimental 'parameter testing space' for the admittance measurements (AS, CV, Tr) covers five dimensions:
1.  AC current frequency from 25Hz to 30MHz
2.  DC Bias from $-3$V to $+3$V.  A wider range can be used at the risk of damaging the sample.
3.  Temperature ranges from $-190^{\circ}$C to $+80^{\circ}$C.  We can maintain sample within one $^{\circ}$C for 10 minutes and for a longer time at temperatures near room temperature.
4.  Light of intensity up to 1 Sun is injected through a fiber cable.  Spectral content is varied using filters.
5.  Sampling time ranges from the shortest interval of about 1.5 seconds to about 600 seconds (keeping temperature within one degree C).  It is possible to sample up to several days at room temperature.

*Temperature*
A custom designed sample stage was built with the principal goal of providing thermal stability.  This is achieved through an insulated copper chamber with a large (15kg) copper mass. The high heat conductivity of copper reduces thermal gradients within the chamber and the large mass (heat capacity) provides thermal stability for the time sufficient to perform each type of measurement at practically constant temperature.  The chamber is heated or cooled beyond the testing temperature(s), allowed to settle, and then as it slowly (about 0.1 °C per minute or slower) returns to room temperature, tests are programmatically triggered at preset temperatures.
Temperature is monitored using a K-type thermocouple connected to an Omega I-series controller which is in turn connected to a PC through a RS232 port.

### Sample Stage

The sample rests on 5cm x 5cm glass rectangle that allows illumination from underneath. The back contact and front contact sample probes are Copper-Tin-Zinc alloy, shaped to have an approximately 1mm$^2$ flat surface for contact with a sample. They are mounted on a custom-built spring cantilever that is controlled with a set screw. The sample itself is located within a 5cm diameter by 5cm high copper cylinder inner chamber. The chamber has notches to allow the probes access to the sample. This inner chamber reduces convection around the sample and helps stabilize the temperature and reduce thermal gradients.

The inner chamber is enclosed in an outer chamber consisting of copper sheets and 2.54cm (1 inch) thick copper slabs. This outer chamber weighs 15kg and provides thermal mass to stabilize the temperature in addition to screening out electromagnetic noise. It is grounded to the LCR meters. The chamber is encased in three layers of insulation foam board with a total thickness of 11.43 cm (4.5 inches).

### Heating and Cooling

Heating is provided by four 6.4mm (¼ inch) by 11.4cm (4.5 inch) 35W cartridge heaters (140W total). These are inserted into bored holes in the copper slabs. The sample can be heated up to 80 °C. This upper limit is because of the melting temperature of the foam board insulation which is less than 100 °C.

Cooling is provided by pumping liquid nitrogen through 6.4mm (¼ inch) diameter copper tubing that is wrapped around the outer chamber copper slabs. The sample can be taken down to near liquid nitrogen temperatures.

### Light

Light is conveyed to the sample through the insulation and copper chambers with a fiber cable 1.25cm (1/2 inch) in diameter. The light source is provided by a Fiber Lite A240P power supply and the accompanying Fiber Lite A240L 150W light source. An intensity of up to about 1 sun is possible. Band pass filters can be inserted to control the wavelength from 500nm to 950nm.

### Time

The fastest LCR meter trigger response time is 1.3 seconds. A sampling length of 600 seconds is possible within a temperature range of 1C (heating/cooling temperature gradient of 0.1C per minute). At room temperature, tests can be run for several days for studying long-term transients.

### Thermal IV characterization

The copper sample stage can also be used to generate J-V curves in a wide temperature range, the same as for admittance measurements. The most desirable approach is to reroute the contact leads to a Keithley source meter and to run the appropriate HPVEE driver program. However, access to a Keithley source meter is limited. Therefore, an alternate system has been developed using the LCR meter as a DC power supply and an available Keithley Digital Multi Meter. Unfortunately, to date, the JV curves generated in this manner have been of inferior quality. This problem will be addressed as time permits. Currently we measure JV characteristics at room temperature with a separate system that allows observation of transients caused by the light pulse and bias voltage switch. The time of transient observation is up to hours.

## 2.5. Preliminary Experimental Results Obtained with the New System

In this section we present some results of initial studies aimed at exploring conditions and procedures of measurements to define those providing more visible manifestations of deep states, hence more opportunities for their detection and studying.

### 2.5.1 Bias induced transients

Measurements were conducted on the CdS/CdTe cells supplied by Dr. D. Albin (NREL).

**Table 2.3** Variations in processing specifications and front contact structure in the cells studied

| Cell ID | SnO$_2$ type | CBD CdS time, min | CSS O$_2$ press., torr | CdTe thickn., $\mu$m | CdCl$_2$ treat. time, min | Pre-contact. etch |
|---------|-----------|-----|-----|-----|------|------------|
| D131A | Bilayer | 35 | 0.8 | 8.9 | 10.0 | Std. NP |
| D133D | Bilayer | 37.5 | 0.8 | 9.0 | 10.0 | Std. NP |
| D135B | Bilayer | 40 | 0.8 | 8.3 | 10.0 | Std. NP |
| D114B | Single l-er | 35 | 1.0 | 8.5 | 15.0 | 200:50BrM |
| D117A | Bilayer | 35 | 1.0 | 8.7 | 15.0 | 200:50BrM |
| D115B | Bilayer | 35 | 0.8 | 9.7 | 6.0 | 200:50BrM |
| D116D | Bilayer | 35 | 0.8 | 9.1 | 13.5 | 200:50BrM |
| D217C | Bilayer | 37 | 0.8 | 9.2 | 8.0 | 200:50BrM |
| D220B | Bilayer | 37 | 1.4 | 8.8 | 7.0 | 200:50BrM |

CdS layers were prepared with the chemical bath deposition, and CdTe films were deposited with close space sublimation. For these first tests a wide range of processing conditions was examined. J-V dependencies measured at CSM demonstrated close efficiency values, except for cell D131A that has obvious shunting effect and was excluded from further measurements. The results of admittance measurements presented below were selected to illustrate the major statements and proposed approaches in Sec. 2.3.
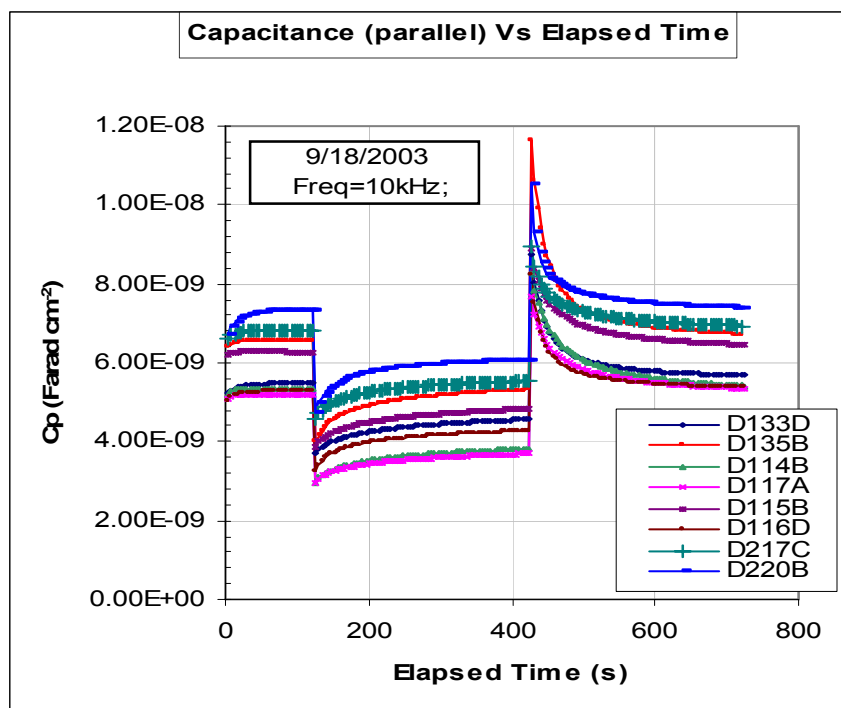
**Figure 2.7** Capacitance transients at T=23°C for the samples listed in Table 2.3, except D131A. The bias voltage sequence is: 0 V → -1 V → 0 V

As seen in Fig. 2.3, the capacitance transients of significant magnitude are observed for all cells. As mentioned in Sec. 2.4, the LCR meter trigger response time is in the range of seconds, therefore we lose the capacitance transients with shorter characteristic times. However, the equipment is available that allows observation and measurement of transients at much shorter time if needed (e.g., that created by Dr. D. Young at NREL). More detailed studies of admittance, including capacitance transients were conducted on the cell D220B. In particular, transients were measured over a much longer time range, up to $t = 2 \cdot 10^5 s$ (~55 hours). The results are presented in Fig. 2.8 with a logarithmic time scale. As shown by these tests, long-term capacitance transients were observed that required several days for total recovery of the initial capacitance.

The evolution of capacitance transients with cell cooling is illustrated by Fig. 2.9a. Fig. 2.9b shows only transients observed after voltage switching back from -1 V to 0 V. Curves show a decrease in magnitude and in the rate of capacitance change with cooling.
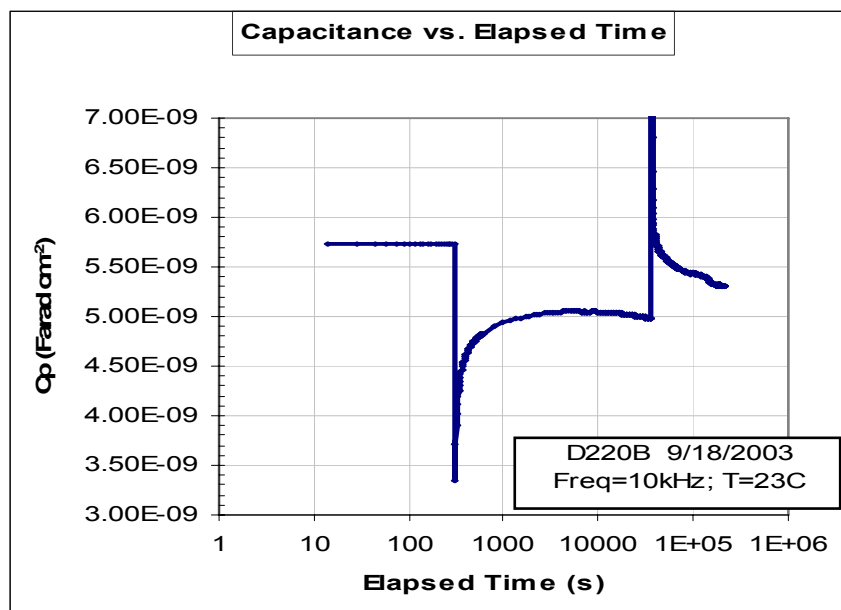
**(a)**
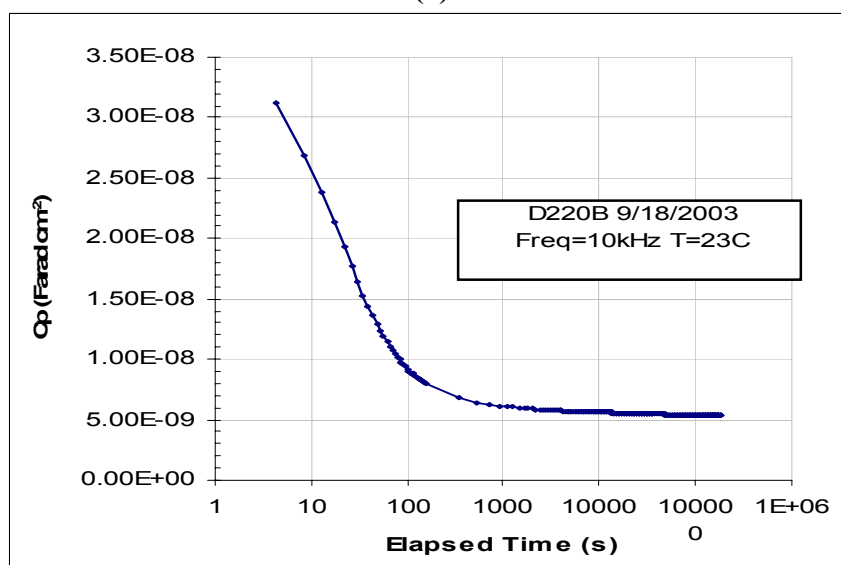


**(b)**

**Figure 2.8** Capacitance transients at T=23$^{\circ}$C for the cell D220B in a wide time range. (a) The bias voltage sequence is: 0 V $\rightarrow$ -1 V $\rightarrow$ 0 V; (b) after switching back to V= 0
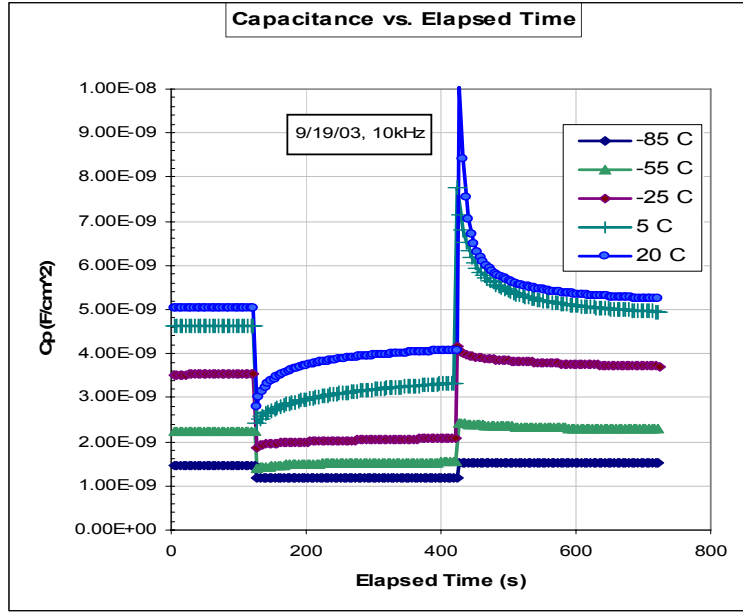
**(a)**
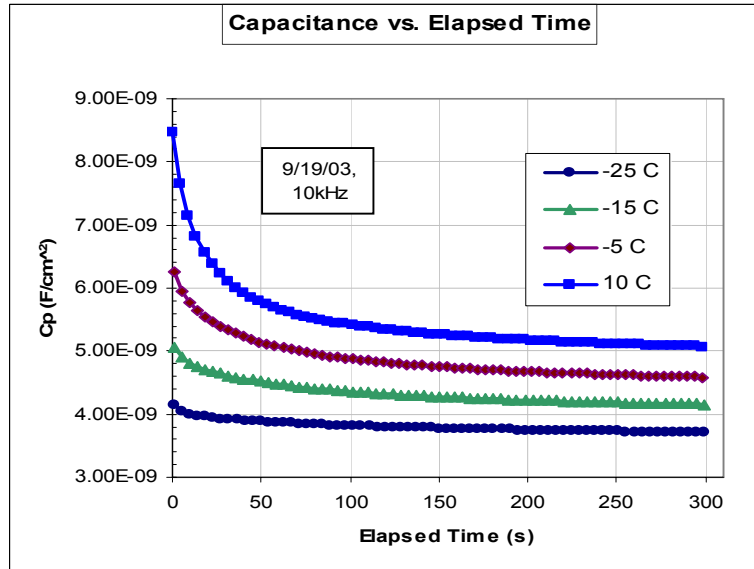


**(b)**

**Figure 2.9** Capacitance transients at reduced temperatures for the cell D220B.
(a) Bias voltage sequence: 0 V→ -1V → 0V;  (b) expanded view following return to 0 V.

To find possible manifestations of the single trap levels or narrow bands, we analyzed the so called DLTS function $S = dC/d(\ln t)$ at each temperature. According to the simple single level theory, the dependencies $S(t)$ or $S(\ln t)$ should have a peak at $t = \tau$ where $\tau$ is the characteristic time of the trap. As seen from Fig. 2.10, the peaks were observed at all temperatures in the range tested. Position of the peak, hence the $\tau$ value, shifted toward longer times with cooling. With a common procedure of $\tau(T)$ analysis, using the Arrhenius plot, we have estimated activation

61

energy of the trap level $E_a = 0.39 eV$ and capture cross section, $\sigma_\infty = 10^{-20} cm^2$. When cooling to -70 °C we have found another trap state: { $E_a = 0.42 eV$ ; $\sigma_\infty = 10^{-18} \cdot cm^2$ }. It should be mentioned that so far we did not try to separate contributions in activation energy of the trap level energy and potential barrier for capturing, therefore the capture cross section derived from Arrhenius plot is denoted as $\sigma_\infty$. A similar analysis of the transients after voltage switch from 0 V to -1 V revealed two more levels: { $E_a = 0.47 eV$ ; $\sigma_\infty = 10^{-16} \cdot cm^2$ } and { $E_a = 0.88 eV$ ; $\sigma_\infty = 10^{-12} \cdot cm^2$ }.
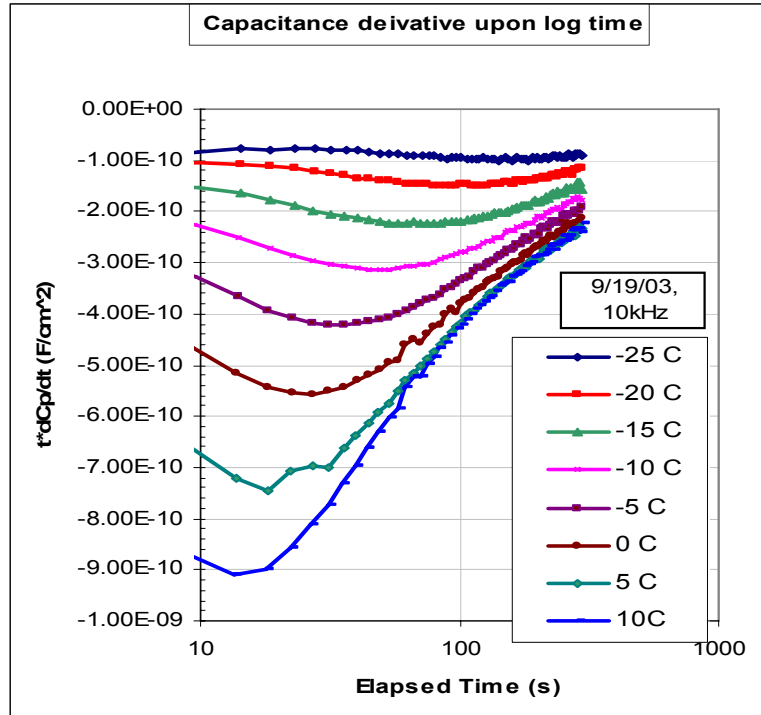


**Figure 2.10** DLTS function for the capacitance dependence on time after the voltage switch from -1V to 0 V, in the temperature range of 10°C to -25°C. Cell D220B.

Fig. 2.11 shows capacitance transients for the cell D217C at elevated temperatures. As expected, both magnitudes of transients and the rate of change increased with higher temperature. The data for the short times after switching voltage to -1 V are not available as explained above. Therefore we were not able to search for relatively "fast" states with $\tau \delta$ 1s. But evidence of the slower states can be seen at longer times. The tendency to saturation in the C(t) dependence is seen for the reverse bias applied as temperature increases. For the highest temperatures of measurements (70, 75, 80°C), saturation is followed by the additional increase.
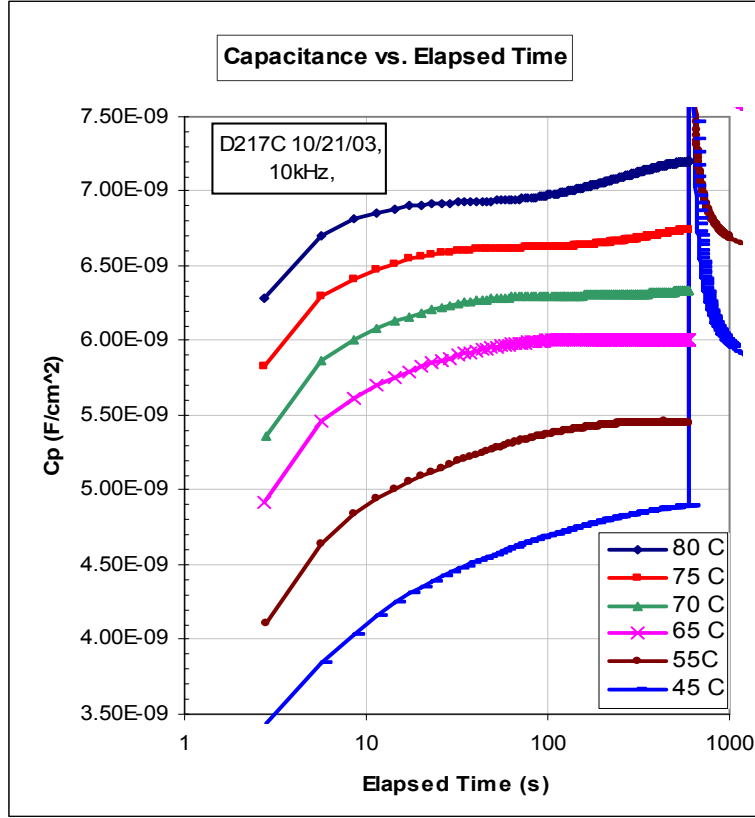
**Figure 2.11**  Capacitance transients at elevated temperatures for the cell D217C.

The DLTS function analysis reveals peaks in the S(t) dependence (see Fig. 2.12) whose position on the time scale rapidly shifts with temperature. This can be due to the presence of a new level with high activation energy.

All the states detected so far from the transient analysis did not reveal themselves in our AS measurements because their characteristic frequencies, $\omega_t = \tau^{-1}$ at reasonable temperatures are beyond the limits of LCR meters. At long times of observation, transient demonstrate very slow changes, maybe caused by specific capture-time dependence due to collective action of closely distanced traps (grain boundaries, or trap clustering).

We have also measured C-f and C-V profiles on all cells. C(f) and G(f) dependencies demonstrated a peak in the range of $\sim 10^5$ kHz or lower at lower temperatures and higher at the elevated temperatures. The Arrhenius plot in the temperature range of 220 K to 340 K provided an activation energy of 0.32 eV and capture cross section of $\sim 10^{-16}$ cm$^2$. Both C-V and C-f dependencies manifested a significant variation with temperature. Figs. 2.13 and 2.14 illustrate changes at higher temperatures.
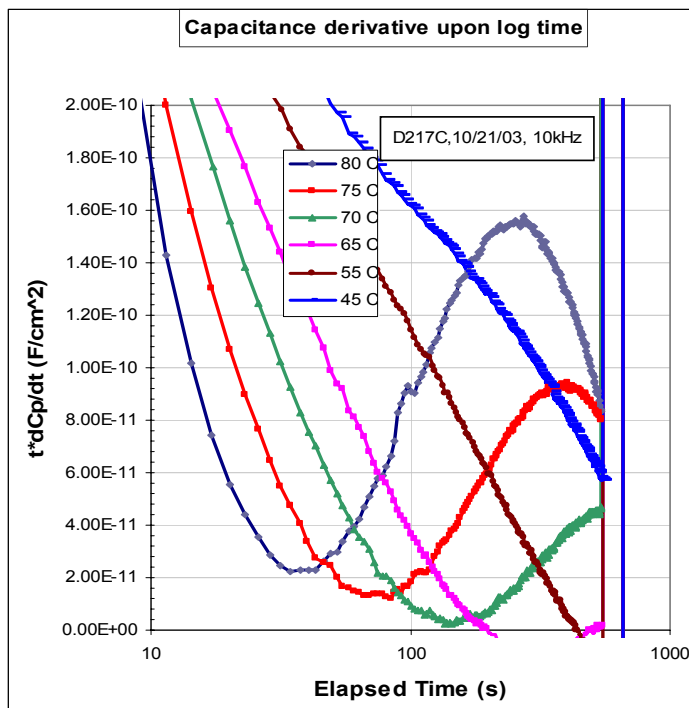
**Figure 2.12** DLTS function for the data presented in Fig. 2.11. The S(t) peaks are well seen at T >70°C indicating presence of a single trap level/narrow band.
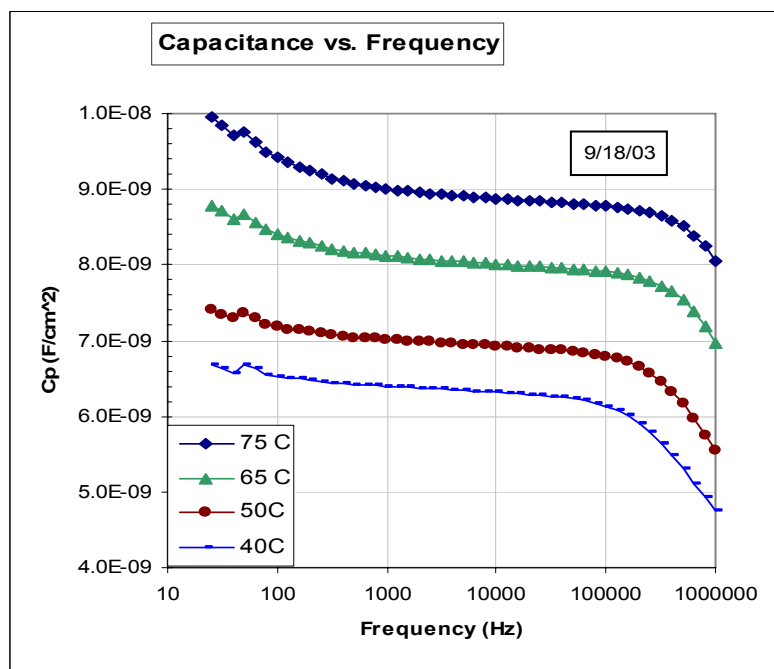


**Figure 2.13** Variation of the C-f dependence with varying temperature in the elevated temperature range. Cell D220B.
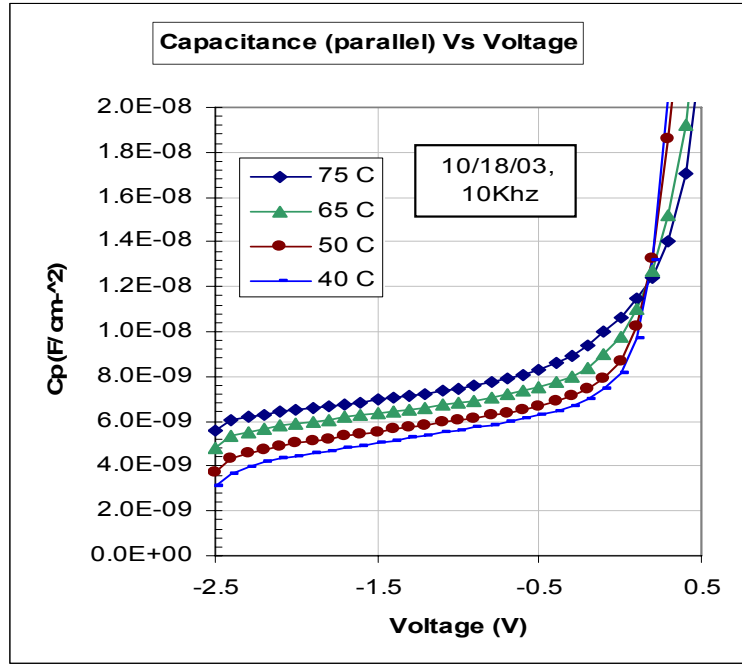
**Figure 2.14** Variation of the C-V dependence with varying temperature in the elevated temperature range. Cell D220B.

The temperature range of measurements was extended down to -130°C. Capacitance continually decreased over the entire temperature range. For example, its value measured at $V_{bias}$ = 0 and f = 10 kHz, decreased 4.2 times from T= + 80°C to T= -130°C. This effect can be explained partially by reducing contribution into measured capacitance of the oscillating trapped charge due to the exponential increase in characteristic time with cooling. However, the free carrier freeze-out effect cannot be excluded. If considerable contribution of the second effect is found, that would indicate a significant role of deep states in controlling carrier concentration. In turn, it will bring us again to the problem of concentration of the $Cu_{Cd}$ defects and their compensation, as well as of the origin of the state with $E_a \approx 0.32 eV$ detected by AS measurements.

Variation of polarity of the "charging pulse" can significantly influence transients and provides additional opportunities to detect and study traps. Capacitance transients at opposite polarities of the applied bias are compared in Fig. 2.15. It is seen that magnitude of a transient is much greater at forward bias (FB) than at reverse bias (RB). Difference between the capacitance values at the beginning and end of the FB transient is 24nF/cm$^2$ (maybe higher, because there is a delay between the bias switch and start of recording, and also the FB steady state was not reached). It is significantly greater than the initial, 6nF/cm$^2$, and final, 9nF/cm$^2$, measured capacitance values. If we attribute the transient to slow traps, we must conclude that their density is greater (maybe much greater) than the concentration of free carriers and faster traps.

The DLTS function for FB (Fig. 2.15 b) demonstrates a well pronounced minimum at $t \approx 280 s$ that can be considered as a manifestation of a very slow single level (narrow band) trap. No extrema are seen in the RB DLTS function. Generally, this should not be surprising. Indeed,

transients at FB and RB, even if controlled by the same trap, are provided by opposite processes: emptying and filling traps and vice versa depending on the trap type (for holes or electrons), while the emission and capture rates can be significantly different.
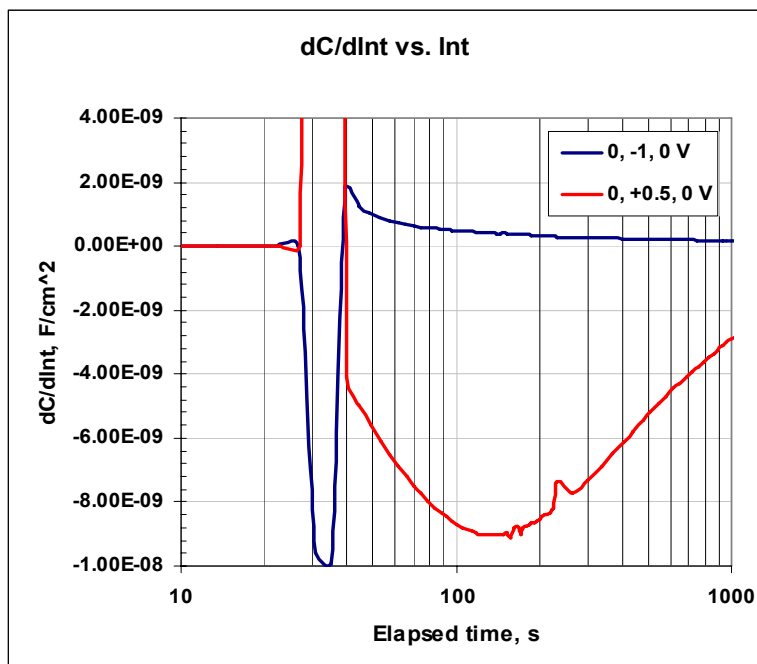


**(a)**
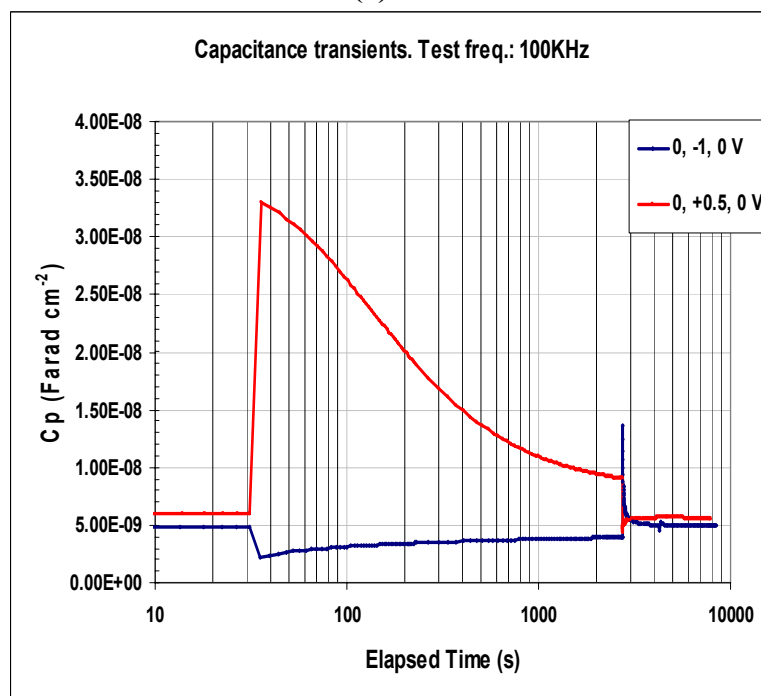


**(b)**

**Figure 2.15** Capacitance transients measured after switching bias from 0 V to V=+0.5V (red) and from 0 V to -1 V (blue). Cell D220B, T≈22°C, f=100 kHz.

In this respect it is very useful to compare transients recorded under applied bias and after switching back to zero bias (relaxation stage). DLTS functions look different for the two stages, sometimes they are rather complex revealing several extrema, both minima and maxima. Thus, comparing transients at different sequence of bias applied and at different polarity one can obtain more detailed and reliable information on the trap type/s, emission and capture rates.

It should be mentioned, that a near total recovery of the capacitance value occurs in several hours after switching back to zero bias in transients presented in the figures above. Reversibility may be considered as an additional argument that the observed transient are caused by a change in the slow trap filling with carriers, but not by generation, transformation or migration of the charged defects.

## 2.5.2 Light induced transients

Slow light induced capacitance transients have been observed at room temperature at wavelengths below and above the CdTe bandgap (wavelength cutoff $\lambda \approx 825$nm). Light intensities were very low, of the order of 0.1mW/cm$^2$. This excludes any significant changes in temperature, verified by the thermocouple readings that did not change with illumination within the accuracy of 0.1$^o$ K. Based on preliminary measurements of the temperature coefficient of capacitance, this may lead to thermally induced capacitance variations not exceeding 0.01nF/cm$^2$, whereas the observed light induced changes were in the range of 0.2 to 1 nF/cm$^2$.

Figure 2.16 shows capacitance versus time for a 30 second initial period in dark, a 45 minute (2700s) light pulse, and a 45 minute recovery period on the CdTe/CdS cell 217C supplied by D. Albin (see Table 2.3). The changes in capacitance indicate changes in depletion width due to changes in net space charge density (SCD). The SCD variations are inferred to result from net charging and discharging of traps.

A pronounced difference can be seen between the above band gap (680nm) and below band gap (1064nm, 1300nm) wavelengths. With the above band gap wavelength, following an initial spike, the capacitance drops below the pre-illumination level before gradually increasing. Both during and following the illumination the capacitance does not reach saturation indicating very long characteristic times ($\tau > 1000s$). Differences in starting capacitance during the initial 30 s period prior to lighting are due to remnant trap charges from previous testing. To start with the same capacitance the sample needed to be kept in the dark overnight indicating $\tau \sim$ hours.

The light source was a 150W halogen bulb filtered with narrow band (~20nm) Corian filters to select the wavelength incident upon the solar cell. Light intensities for the 680nm (1.82eV) and 1064nm (1.17eV) wavelengths were measured with a silicon based optical power meter. For the 1300nm (0.95eV) wavelength that is below the 1.1 eV silicon band gap, no direct light intensity measurements were made. In this instance the rheostat setting was left the same as for the 1064nm wavelength and the light intensity was assumed to be approximately the same.

Figure 2.17 shows capacitance versus time for light intensities of 0.025, 0.050, 0.100, 0.200, and 0.400 mW/cm$^2$. For each test, the sample was kept in the dark overnight prior to the test so as to start with a comparable capacitance value. In spite of this, there remained minor starting capacitance differences of up to 0.1 nF. On a couple of tests the sample was kept in the dark for 60 hrs over a weekend (not shown in figure 2.17) and this caused the starting capacitance to drop by an additional 0.2nF. Even with these offsets, the structure of the light induced CTr curves was essentially the same. Thus, overnight in the dark was determined to be sufficient for these low light CTr tests.
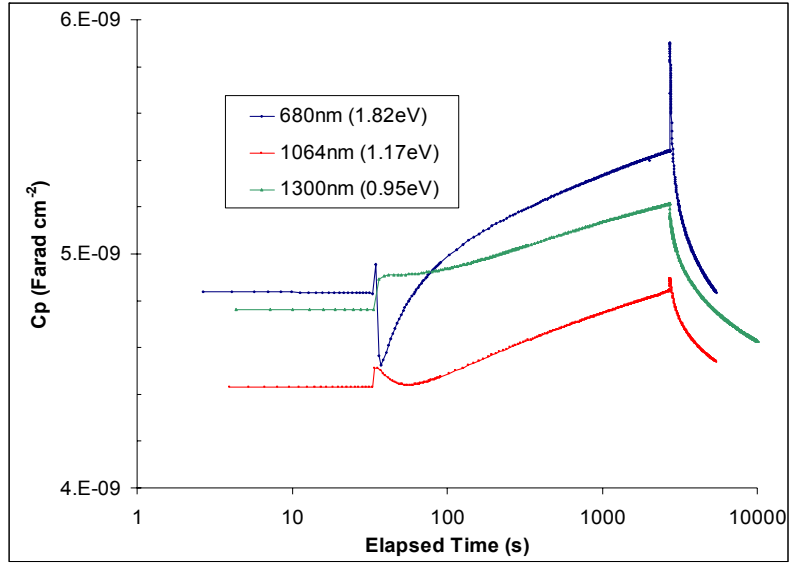
**Figure 2.16** Light induced capacitance transients for $0.1 mW/cm^2$ lighting intensity and wavelengths of 680nm, 1064nm, and 1300nm. Testing voltage frequency is 100kHz, sequence is 30s dark, 2700s light, 2700s dark. Sample D217C (Table 2.3)
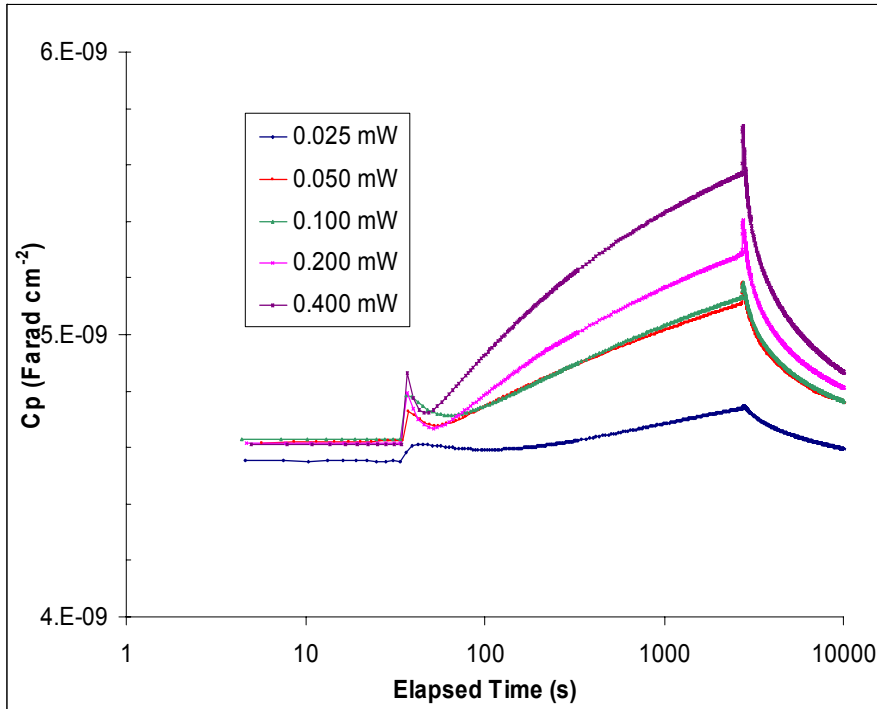


**Figure 2.17** Capacitance transients induced by the sub-bandgap (1064 nm) light of various intensities.

In all cases there was no measurable electrical potential generated by the cell from this sub - bandgap light source. There was an initial increase in capacitance indicating a net increase in the negative space charge density (SCD) for the p-type CdTe material. There is a subsequent decrease in capacitance followed by a gradual increase. The drop in capacitance never reached the pre-illumination level. During the 45 minute illumination period the capacitance increase never saturates. Since the light source is sub-bandgap, these phenomena are a result of direct interaction of photons with deep traps. This involves the promotion of electrons from the valence band to the trap or from the trap to the conduction band. This direct photon interaction is superimposed on the thermal emission and capture of holes and electrons by the trap.

When the light is switched off, as the cell returns to its pre-illumination equilibrium, there is a spike in capacitance followed by a gradual decrease in capacitance. This is a typical transient response. It takes at least several days in the dark for the cell to return to equilibrium. The magnitude of the effect increases with intensity but the basic structure remains the same. The spikes at the beginning of illumination and after the light is switched off are limited by the 3 second capacitance reading interval of our instrumentation and the approximately 2 seconds for the bulb to fully illuminate and extinguish.

The preliminary experiments with light indicate that further studies of light induced transients along with those caused by bias changes will provide new opportunities for detecting, characterization and identification of deep electronic states in CdTe solar cells.

## 2.6    Summary

1. The basics of admittance spectroscopy (AS) as a method for detection of deep states and studying their properties were presented and discussed along with two modifications of AS. (Sections 2.2.1 and 2.2.2)
2. Our studies of CdTe cells using AS and modified AS revealed various deep states with concentration, spatial distribution and characteristic time, that depend on deposition technique, postdeposition treatment, and contacting procedure (Sec. 2.2.3). A common feature of the cells fabricated at different facilities (FS, NREL, UT, FS/CSM) was a high trap concentration, $N_t$, exceeding doping level, $N_{C-V}$, determined by C-V profiling. In some cells density of detected trap states was of the order of $10^{16}$ cm$^3$. Experimental data also indicated presence of significant amount of slower traps not detectable with the standard AS equipment .
3. The common approach to the analysis of AS and DLTS measurements is based on the theory valid for low trap concentration much smaller than the doping level ($N_t << N$). In the case of CdTe this approach should be revised based on more adequate theory and numerical modeling using more reliable physical models. The common equations used for trap concentration estimates, actually provide the ratio $N_t / N$. Analysis presented in Sec. 2.3.1 shows that at $N_t \tau N$ this ratio is underestimated, especially if the levels are located close to Fermi level. On the other hand, the doping level derived from C-V profiling, $N_{C-V}$ can be strongly overestimated if $N_t > N$. Numerical estimates of apparent doping level, $N_{C-V}$, compared to the real one, $N$ , are presented  for CdTe with two trap levels having characteristics close to those determined by AS.

4. In Sec. 2.3.2 the technical limitations on the characteristic time of traps available for detection by AS are considered. As possible solutions of the problem, variation of temperature and measurements of transients are discussed.

5. The procedure for determining trap cross section is considered in Sec. 2.3.3, in particular with respect to the traps with the repulsing potential barrier. The latter is considered in more detail for the barrier provided by collective action of closely spaced traps, e.g., trap clusters and especially grain boundary states. The latter are considered as the most important origin of very slow traps. The trap filling dependence on time is specific for these "collective" trap states which can be used for their identification.

6. The current state of the transient studies in CdTe is unsatisfactory (Sec. 2.3.4). The transients have been observed but not studied properly. Studying of capacitance transients is the most promising method for detection slow/deep states, estimating trap concentration, distinguishing between the majority- and minority-carrier traps.

7. A new measurement system recently developed in our facilities is described in Sec. 2.4. The system is designed for studying the cell admittance, in particular, C-f and C-V dependencies, along with transients in a wide temperature range, from below -100$^{\circ}$C to +80$^{\circ}$C. Measurements can be conducted in dark and under illumination of varying intensity and spectrum.

8. The preliminary results of measurements presented in Sec 2.5 show that the system provides the expected/designed options. Measurements revealed transients, including very long-term ones. Analysis of transients based on DLTS function detected at least five levels or narrow bands with characteristic times in the range of $\sim 10s - 100s$ not available for common AS. Analysis of temperature dependencies using the Arrhenius plot allowed estimates of activation energy and capture cross section. We noted very slow transients a, non-exponential decays, and very low capture cross sections that could be attributed to grain boundaries. A significant capacitance dependence on temperature in the range of -130 to +80$^{\circ}$C was found. Possible mechanisms of dependence were briefly discussed.

## 3. EFFECT OF CdCl$_2$ TREATMENT, DOPING WITH Cu, AND STRESSING ON DEEP ELECTRONIC STATES (DES)

To date all high performance CdTe solar cells have included CdCl$_2$ treatment and Cu doping in a postdeposition heat treatment [62]. While the complex interaction between these two additives is known to favorably change the defect structures that control performance, the understanding of this process remains incomplete. To help address this, we used admittance spectroscopy (AS) and capacitance transients (CTr) to study differences in deep electronic states (DES) for CdTe cells produced with and without both Cu and CdCl$_2$. This study is a continuation of our previous efforts to monitor deep states behavior in cells under varying processing procedures [14]

### 3.1 Samples

The cells for this study were produced at NREL by Dr. D. Albin. They were grown on Corning 7059 glass substrates with a bi-layer (500 nm F-doped/100 nm undoped) tin-oxide

structure used as the front transparent contact. The CdS window layer was deposited by chemical bath deposition (CBD) to a thickness of ~80nm followed by close-spaced sublimation (CSS) of the CdTe absorber layer to a thickness of ~8μm. The CdCl$_2$-treated devices were annealed at 400° C in a CSS-arrangement using anhydrous CdCl$_2$ as a source in an ambient of 100 torr Oxygen/400 torr Helium for 7 min. All devices were then etched with a nitric-phosphoric acid (NP) etch consisting of 1:88:35 parts HNO$_3$:H$_2$PO$_4$:H$_2$O. Back contact carbon-based pastes (Electrodag 114) with and without Cu additives (Cu$_{1.4}$Te powder) were applied to the CdTe surface by brushing. The back contact areas are approximately 0.5cm$^2$ and a 260$^o$C anneal in helium was applied to activate the contact. To avoid back to front contact electrical shorting, a ~1 mm lateral margin of solar cell material was retained around the back contact. This enhances current collection at the back contact edges yielding higher short-circuit current values than would be obtained without the margin. The results presented in this section (Sec. 3) were obtained mostly on four cells with different combinations of CdCl$_2$ treatment and Cu doping: [No-Cu, Yes-CdCl$_2$], [Yes-Cu, Yes-CdCl$_2$], [Yes-Cu, No-CdCl$_2$], [No-Cu, No-CdCl$_2$].

   Light JV curves for each cell are shown in Fig. 3.1. The cells treated with CdCl$_2$ performed significantly better than the non CdCl$_2$ treated cells for all metrics including: efficiency (η); open-circuit voltage (V$_{oc}$); short-circuit current (J$_{sc}$); and fill factor (FF). The cells treated with Cu had better η, V$_{oc}$, and FF. The best cell with the combination CdCl$_2$ and Cu treatment had a slightly lower J$_{sc}$ than the CdCl$_2$ only cell. Rollover can be seen in the cells processed without Cu due to the back contact Schottky barrier [63].
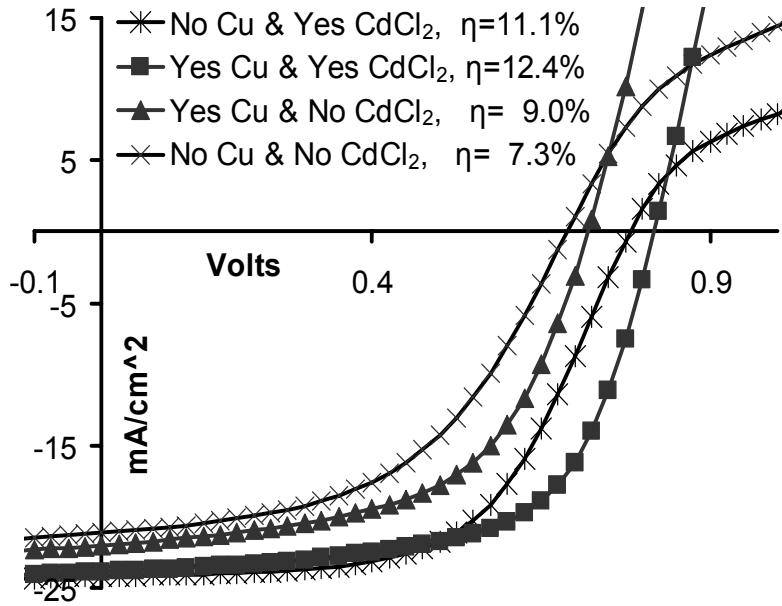


**Figure 3.1** Light JV curves for the four CdTe solar cells studied.

## 3.2. Admittance Spectroscopy Measurements and Analysis

### 3.2.1 AS spectra and their analysis. Trap signatures

As explained in Sec. 2.2.1, when the testing AC signal angular frequency, $\omega$, significantly exceeds the trap characteristic frequency, $\omega_t = 1/\tau_t$, the trapped electrical charge cannot follow the AC signal resulting in a lower measured capacitance, $C_p$, and saturation in the AC conductance, $G_p(\omega)$, dependence. Trap characteristic frequency $\omega_t$ can be determined experimentally from the plots of either $\omega\, d\, C_p / d\, \omega$ or $d\, G_p / d\, \omega$ versus $\omega$. Both have peaks at $\omega_{peak} = \omega_t$. Since the characteristic frequency strongly (exponentially) depends on temperature, trap oscillating capacitance measured at fixed AC signal frequency, is also temperature dependent. Namely, its contribution is negligible at low temperatures where $\omega_t << \omega$, while reaches its maximum and saturates at high temperatures where $\omega_t >> \omega$. To demonstrate trap contribution into capacitance, distinguish traps with different characteristic frequencies (times), and estimate their relative densities, we will use in this section images combining frequency and temperature dependences of capacitance and AC conductance as seen from the figures below. The magnitude of the trap contribution to the capacitance, $C_t$, indicates the relative trap concentration. This is applicable even when the trap concentration is higher than the doping level as is often the case with polycrystalline thin film CdTe cells.

The measured capacitance $C(\omega)$ and conductance $G(\omega)$ are modeled here by:

$$C(\omega) = C_d + \frac{C_t}{1 + (\omega/\omega_t)^{2\beta}}; \qquad G(\omega) = G_d + (C_t\omega_t)\frac{(\omega/\omega_t)^{2\beta}}{1 + (\omega/\omega_t)^{2\beta}} \qquad (3.1)$$

$C_d$ and $G_d$ represent the base depletion capacitance and the cell DC differential conductance, respectively. $C_t$ represents the maximum low frequency trap capacitance. We have added a phenomenological term, $\beta$, in the exponent to help with fitting to the experimental data. This is similar to the stretched exponential parameter that is used to model many natural phenomena [64]. The capacitance transition from $C_d + C_t$ to $C_d$ can be spread over a wide range of frequencies and often a good fit is obtained with $\beta \approx 0.5$. This could be caused by a finite width band of trap energy levels. The peak location in plots of either $\omega\, d\, C_p / d\, \omega$ or $d\, G_p / d\, \omega$ versus $\omega$ is again at $\omega = \omega_t$ and does not depend on the $\beta$ value.

We used $C_t$ for relative comparisons of trap concentrations and have avoided using common quantitative formulas because the trap concentrations are high relative to the free carrier concentration, violating underlying formula assumptions. Besides, the trap concentrations vary spatially further complicating quantitative analysis. We verified that the $\omega\, d\, C_p / d\, \omega$ peaks were not manifestation of RC circuit back contact Schottky barrier. It was done by adding known resistors in series and checking that $\omega_{peak}$ did not change. It did not change also with application and varying of the forward bias around +1 V, which should change resistance of a Schottky barrier and related $\omega_{peak} = (RC)^{-1}$.

AS differences were observed between each of the four differently processed cells and the most noticeable were between the Cu- doped and undoped cells. This can be readily seen by comparing the graphs in Fig. 3.2 which show the AC conductance versus temperature.
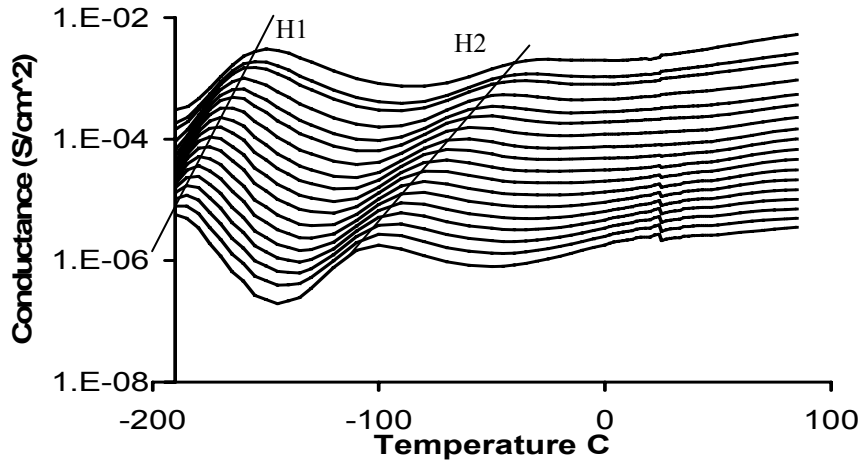


**(A)**
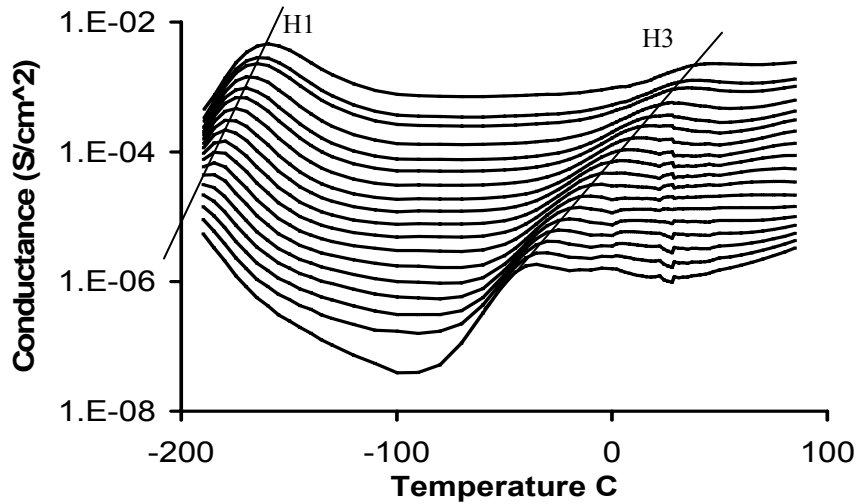


**(B)**

**Figure 3.2** AC conductance versus temperature lines shown for AC frequencies ranging from 1kHz (bottom line) to 1MHz (top line). The upper graph (A) is for the cell with both the Cu and $CdCl_2$ treatment, and the lower graph (B) is for the cell with only the $CdCl_2$ treatment. The detected majority carrier traps labeled H1 through H3 are shown with lines connecting the conductance peaks.

The upper Fig. 3.2A shows the cell with the combined Cu and $CdCl_2$ treatment and Fig. 3.3B shows the cell with the $CdCl_2$ only treatment. Each line corresponds to a fixed AC signal frequency with frequencies ranging from 1kHz to 1MHz. The peaks on the lines indicate traps with the characteristic frequency corresponding to the line frequency at the peak's temperature. The families of peaks clearly show the temperature to characteristic frequency relationships for multiple traps. Lines connecting the peaks have been added and are labeled to identify the different trap signatures that are subsequently discussed.

A total of three distinct hole trap signatures were analyzed. Table 3.1 lists the traps along with the cells in which they were detected

**Table 3.1**. Activation energy, $E_a$, apparent cross section, $\sigma$, and trap contribution to capacitance, $C_t$, for traps detected with AS in cells with different combinations of Cu and $CdCl_2$.

| Trap | Cu | $CdCl_2$ | $E_a$ (eV) | $\sigma$ $(cm^2)$ | $C_t$ $(nF/cm^2)$ | Temp. Range for the Arrh. plot (K) |
|------|-----|----------|------------|-------------------|-------------------|-------------------------------------|
| H1 | No | Yes | .128±.003 | 8E-14 | 3.0 | 83 to 108 |
|    | Yes | Yes | .133±.006 | 4E-14 | 2.1 | 83 to 118 |
|    | Yes | No | .128±.005 | 2E-14 | 1.1 | 83 to 118 |
|    | No | No | .145±.007 | 1E-12 | 2.5 | 83 to 108 |
| H2 | Yes | Yes | .305±.010 | 9E-14 | 0.9 | 183 to 238 |
|    | Yes | No | .292±.009 | 6E-14 | 0.5 | 173 to 233 |
| H3 | No | Yes | .475±.006 | 7E-13 | 0.6 | 243 to 310 |
|    | No | No | .464±.009 | 8E-13 | 0.5 | 238 to 300 |

The trap signatures in the table were grouped based on a combination of their activation energy and their detection temperature range. Temperature and frequency dependent capacitance for all four combinations of Cu and $CdCl_2$ are presented in Fig. 3.3.
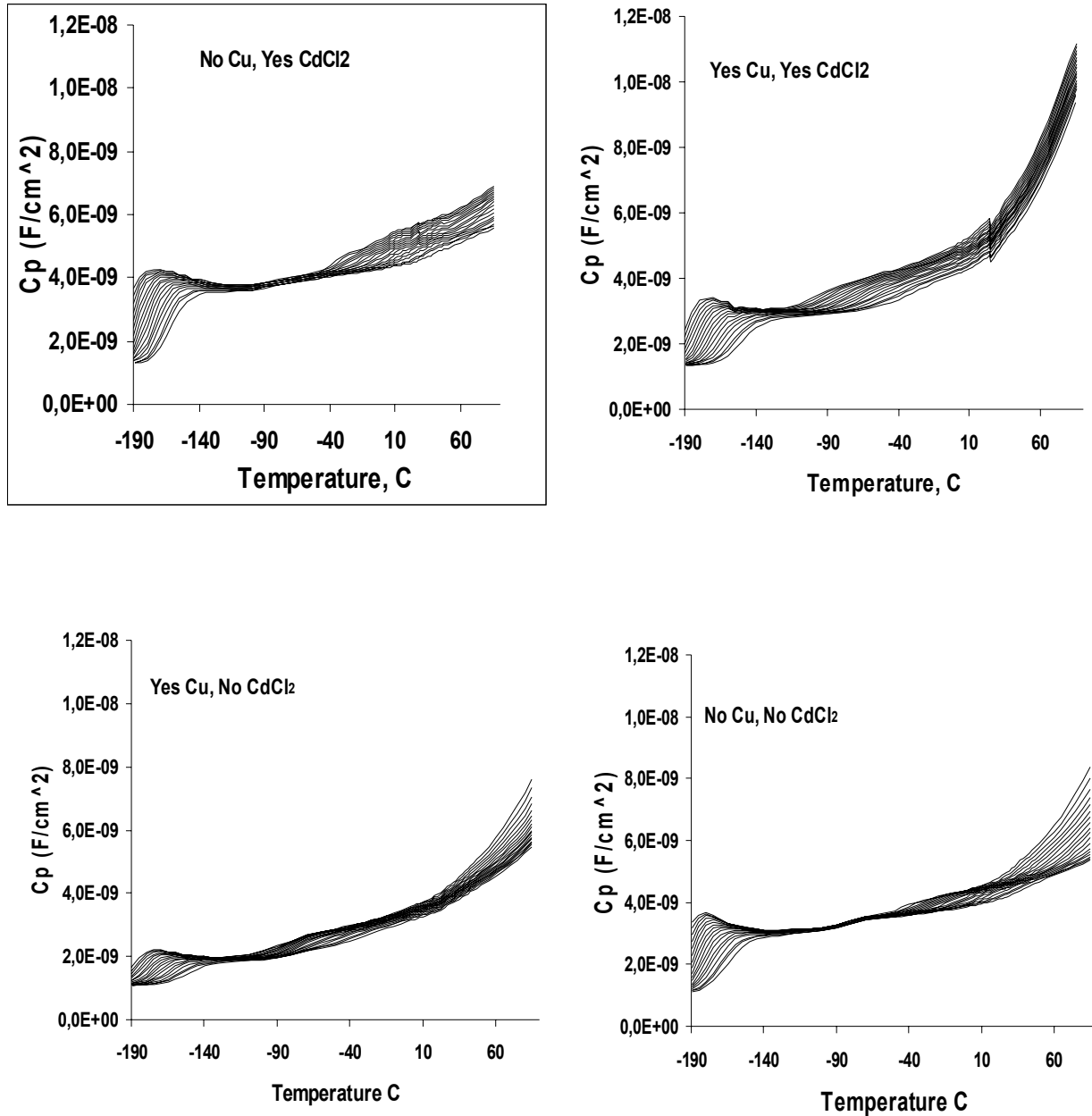
**Figure 3.3** Temperature dependence of capacitance at frequencies ranging from 1Khz (top line) to 1MHz (bottom line).

Frequency dependent capacitance at a fixed temperature indicates trap contribution into the measured capacitance. In agreement with the temperature and frequency dependent AC conductance in Fig. 3.2, the graphs in Fig. 3.3 demonstrate presence of at least three different types of traps. Trap labeled above as H1 manifests itself at low temperatures (Tδ-130 C). At the lowest temperature (-190 C) and highest frequency (1MHz), capacitance of all four cells is close to the value determined with the equation $C = \varepsilon\varepsilon_o / d$ (d is the CdTe thickness). Capacitance

75

increases with reducing frequency because frequency of voltage oscillations, $\omega$, comes closer to the trap characteristic frequency, $\omega_t$. As temperature increases to T≈-130 C, dependence on frequency becomes minimal indicating that above this temperature $\omega_t > 2\pi \cdot 10^6 s^{-1}$ and trapped charge follows applied voltage oscillations even at f=1MHz. At further increase in temperature the frequency dependence again becomes significant because now new slower (and deeper) traps start to contribute to capacitance, although the high frequency capacitance does not change for a while until the $\omega_t$ value exceeds $\omega$ due to temperature increase. After that, capacitance increases with temperature at all frequencies. An appropriate analysis of the $C(\omega, T)$ dependencies reveals the H3 trap in the [No Cu – Yes CdCl$_2$] spectra and the H2 trap in the cells doped with Cu.

The $C(f)$ dependence not disappearing at higher temperatures (up to T=+85 C) could be considered as a manifestation of multiple slower traps or wide trap level band.

At fixed temperature, difference between high frequency and low frequency capacitance which provides an estimate of the $C_t$ value, is proportional to the trap density. Therefore, it follows from the figures above that the H1 density is the greatest for the CdCl$_2$ treated, but not doped with Cu, cell. For the [Cu+CdCl$_2$] cell, the H2 density is high, while Cu doping alone, without CdCl$_2$, leads to a significantly lower H2 density.

### 3.2.2. Attribution of detected traps

We have mentioned previously that there is a lot of ambiguity and discrepancies in attribution of the deep electronic states to particular defects. However, keeping reservations, we would like to discuss possible attribution for the traps we have labeled as H1, H2 and H3.

A strong H1 signature was observed in all four cells with E$_a$ matching the 0.13 eV singly ionized cadmium vacancy $V_{Cd}^-$ acceptor defect [65, 20] as well as the chlorine A-center $V_{Cd}^{2-} - Cl_{Te}^+$ acceptor defect [65, 22]. Perhaps we deal with both presented in different proportions in differently treated cells. The NP etch leaves behind a ~0.1μm thick free Te layer at the back surface and a Te enriched layer underneath [66] . This serves as a source of $V_{Cd}^-$ diffusing in the CdTe depth. The C$_t$ values indicate that the H1 density *decreases* with the addition of Cu which is consistent with Cu substitutions on cadmium vacancies meaning partial replacement of $V_{Cd}^-$ with $Cu_{Cd}$. Just on this effect was based an explanation of temperature dependence of the EL pattern in the Cu-dot cells (see Sec.1). In turn, the H1 concentration *increases* with the addition of CdCl$_2$ which is consistent with the formation of $V_{Cd}^{2-} - Cl_{Te}^+$.

The H2 signature was only detected in cells doped with Cu. The E$_a$ ~0.30 eV is close to $Cu_{Cd}$ values observed by others [21, 67] and we thus inferred that this was a $Cu_{Cd}$ defect. The H2 concentration was higher with CdCl$_2$ implying that the defects induced by CdCl$_2$ increased the concentration of $Cu_{Cd}$.

The H3 signature with an E$_a$ of 0.47 eV was only detected in cells with no intentionally added Cu. This energy level has been detected by others [67, 68] and in two instances has been attributed to $V_{Cd}^{2-}$ [65, 69] in strong discrepancy with the theoretical $E_a$ estimates for this defect [20]. Besides, we note that H1 which we attributed to the singly ionized $V_{Cd}^-$ remains detectable

with Cu, while H3 does not, although both are ascribed to the cadmium vacancy. We also would not exclude that H3 is caused by the negative U-center $Te_i^{2-}$. The apparent discrepancy between our measured $E_a$ of 0.47 eV and the calculated transition (0/-2) energy of 0.57 eV [20] can be eliminated by suggesting the U value of –0.2 eV. We have observed the H3 trap only in the cells subjected to the NP etch, but did not see it in the cells etched with Br: Methanol. NP etch provides a strong excess of Te in the top layer of CdTe. One can suggest that due to that the interstitial Te concentration can be significant in CdTe, at least at the region not too remote from the back contact. Disappearance of the H3 manifestation in Cu doped cell could be attributed to masking by H2 contribution into admittance. Another, "more scientific", explanation could be that high Cu concentration leads to high negative space charge density in the depletion region. This, in turn, leads to redistribution of the CdTe band bending in the way that increases distance between the crossing point of the H3 level and back contact. Since excess Te diffuses from the back contact, it is reasonable to suggest that the $Te_i$ density sharply decreases with increase in this distance making H3 not detectable. However, we remain cautious about assigning H3 to a specific defect. The H3 β values were higher than average, possibly indicating a narrower energy band for this defect.

## 3.3    Deep States Studied with Capacitance Transients

As discussed in previous sections, the finite LCR meter frequency range puts limitations on the characteristic frequency of the traps that can be detected and studied with admittance spectroscopy. As an alternative method, we have used the capacitance transient measurements which allow detection of very slow states with the characteristic times $\tau_t = \omega_t^{-1}$ in the range of seconds, minutes, etc. The transient effects presented and analyzed in this section were induced by changes of the bias applied to a cell in various sequences: Zero Bias (ZB) → Forward Bias (FB), ZB→ Reverse Bias ( RB), FB→ZB, RB→ZB, FB→RB. Since the procedure of measurements in our measurement system (Sec. 2.4) provides $C, G_t(t, V, T)$ dependences in one temperature run, we have used the for the trap detection analysis of $C(t)$ and $G(t)$ at different temperatures. Activation energy and apparent cross section, as before for AS, were derived from the Arrhenius plot. The sign of the DLTS function peak (maximum or minimum) allowed to distinguish the majority (hole) and minority (electron) carrier traps.

### 3.3.1   Trap Signatures. Arrhenius plots

Figure 3.4 shows the Arrhenius plots obtained with transient measurements along with those obtained with AS measurements. The principal difference between these two groups is in the range of characteristic times. Traps H1, H2, H3 had characteristic times short enough ("fast traps") to be detected with AS. Traps E2, E3, H4, H5, H6 ("slow traps") could be detected only via transient measurements since the temperature range was limited to T~85 C to avoid irreversible effects caused by heating. Note that temperature ranges where we were able to detect and study manifestations of specific traps were narrower for slow traps studied with C-Tr. This leads to a larger inaccuracy in determining activation energy from the slope of a plot and capture cross section from the intersection with the 1/T axis. In particular, it is not clear whether the plots labeled H4 and H5 represent different traps or the same one.

It is seen from Fig. 3.4 and Table 3.2 that the set of detectable traps varies with the cell treatment. Namely, E2, H6 were found only in a cell with (CdCl$_2$+Cu) treatment. These states were not seen if one of the treatments was missed. E3, H4 were seen only without Cu doping, H5 with [Yes Cu - No CdCl$_2$] treatment. As seen from the table, all slow traps have low or moderate capture cross section, except H5 with $\sigma \approx 10^{-11} cm^2$.

**Table 3.2.** Traps detected with the capacitance transient (C-Tr) studies

| Cu / CdCl$_2$ | Hole/Electron  trap | $E_a, eV$ | $\sigma, cm^2$ |
|---|---|---|---|
| Yes /Yes | E2 | 0.21 | 1.0x10$^{-17}$ |
| No / Yes | E3 | 0.40 | 4.3x10$^{-15}$ |
| No / Yes;   No / No | H4 | 0.51;  0.53 | 1.7x10$^{-15}$;   6.2x10$^{-15}$ |
| Yes / No | H5 | 0.70 | 8.7x10$^{-12}$ |
| Yes / Yes | H6 | 0.83 | 8.3x10$^{-17}$ |
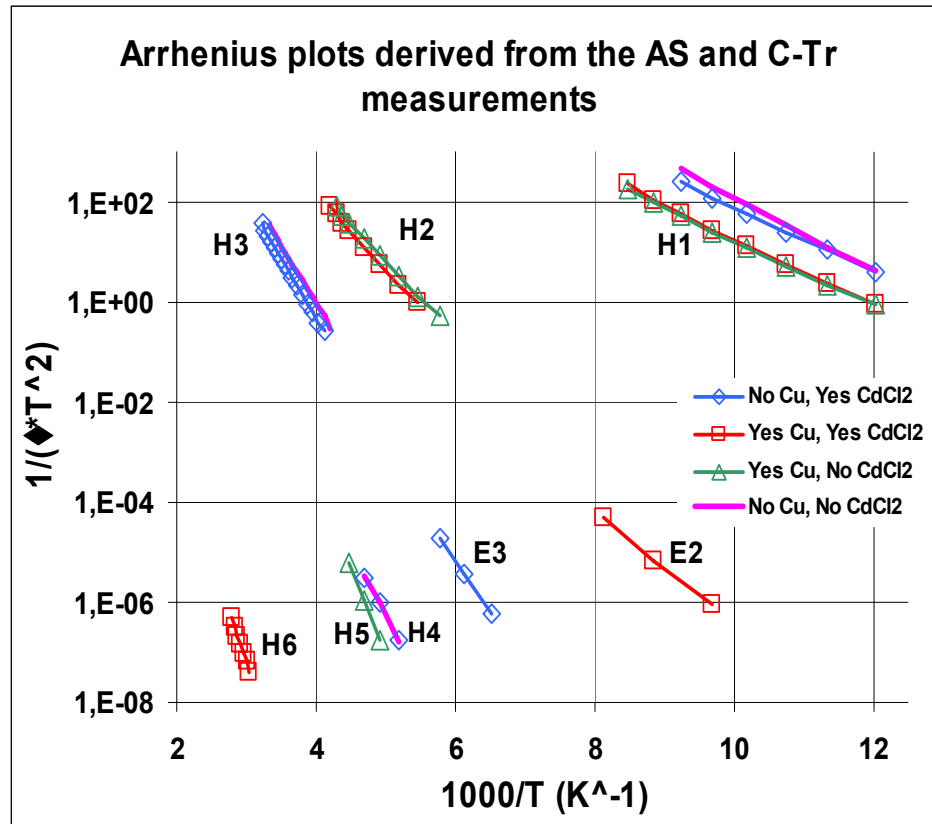


**Figure 3.4**      Arrhenius plots for traps detected by AS (H1, H2, H3) and those detected by C-Tr (H4, H5, H6, E2, E3). H1 to H6 are traps for holes; E2 and E3 are traps for minority carrier electrons.

### 3.3.2   Relative densities of different traps

It would be instructive to compare the different trap densities in differently treated cells. For the H1, H2, H3 states we have done it using the $C(T,\omega)$ dependencies presented in Fig. 3.2. For long term transients we used the magnitude of capacitance transients and the magnitude of a peak in the plot of DLTS function vs. time. Although there should be inaccuracies in the numerical estimates, the sequence of the determined $C_t$ values, probably, correctly represents ordering of the traps with respect to their density.

The H1 concentration (presumably related to $V_{Cd}^-$ and $V_{Cd} - Cl_{Te}$ A-center) are high. H1 states were found in all cells. Diffusion of Cu reduces density of H1 states, supposedly due to replacement of $V_{Cd}$ by $Cu_{Cd}$. Concentration of H2 states detected only in Cu-doped cells was also in the order of one nF/cm$^2$, but lower than the H1 density. The same order of magnitude has the concentration of H3 states except Cu-doped cells, where it was undetectable. Concentration ofH4, H5, E2 and E3 states in the cells where they could be detected is below 0.1nF. State H6 that was found only in a cell [Yes Cu / Yes CdCl₂], demonstrates the highest $C_t$ value of 7.5 nF/cm$^2$, which corresponds to trap density exceeding $10^{15}$cm$^3$.

**Table 3.3.** Transient capacitance $C_t$ for various types of traps

|  | Cell type | | | |
|---|---|---|---|---|
|  | No Cu / Yes CdCl₂ | Yes Cu/Yes CdCl₂ | Yes Cu / No CdCl₂ | No Cu / No CdCl₂ |
| Trap type | $C_t$, nF/cm$^2$ | | | |
| H1 | 3.0 | 2.2 | 1.1 | 2.4 |
| H2 | - | 1.0 | 0.5 | - |
| H3 | - | 0.6 | - | 0.5 |
| H4 | 0.07 | - | - | 0.07 |
| H5 | - | - | 0.08 | - |
| H6 | - | 7.5 | - | - |
| E2 | - | 0.025 | - | - |
| E3 | 0.08 | - | - | - |

### 3.4   Effect of Stress

The cells prepared as described in Sec. 3.1, were subjected to accelerated degradation  in light of 1 Sun intensity at 100$^0$C, under open circuit conditions. The stressed cells were characterized in the same way as the as prepared ones. The J-V characteristics are presented in Fig. 3.5 for all four types cells before and after stress and before stress.

Table 3.4 presents common cell parameters: efficiency $\eta$, open circuit voltage $V_{oc}$, short circuit current $J_{sc}$, fill factor $FF$, "shunt resistance" $R_{sc} = (dJ/dV)^{-1}\big|_{V=0}$, "series resistance" $R_{oc} = (dJ/dV)^{-1}\big|_{J=0}$

**Table 3.4** Cell parameters before and after stress

| Cell | Before/after stress | $\eta$ (%) | $V_{oc}$ (V) | $J_{sc}$ (A/cm$^2$) | FF (%) | $R_{sc}$ (Ω-cm$^2$) | $R_{oc}$ (Ω-cm$^2$) |
|---|---|---|---|---|---|---|---|
| No Cu Yes CdCl$_2$ | Before | 11.1 | 0.782 | 24.16 | 58.9 | 1350 | 11.2 |
|  | after | 9.9 | 0.757 | 23.82 | 54.7 | 912 | 13.7 |
| Yes Cu Yes CdCl$_2$ | Before | 12.4 | 0.818 | 23.88 | 63.3 | 578 | 5.2 |
|  | after | 11.7 | 0.788 | 23.91 | 62.1 | 992 | 5.7 |
| Yes Cu No CdCl$_2$ | Before | 9.0 | 0.720 | 22.03 | 56.6 | 276 | 6.3 |
|  | after | 7.7 | 0.692 | 20.25 | 54.6 | 376 | 7.7 |
| No Cu No CdCl$_2$ | Before | 7.3 | 0.688 | 21.16 | 50.1 | 287 | 10.5 |
|  | after | 6.7 | 0.683 | 20.24 | 48.4 | 286 | 13.75 |

Degradation of J-V dependences was not too severe for all cells. The efficiency decreased by about 11 relative percents for all cells. Decrease in $V_{oc}$ did not exceed 30 mV; the highest decrease in $J_{sc}$ by 1.8 mA/cm$^2$ was for the [Yes Cu –No CdCl$_2$] cell, for other cells it did not exceed 0.3 mA/cm$^2$. Fill factor decreased by 4.2% for the [No Cu –Yes CdCl$_2$] cell and only by 2% or less for other cells. $R_{oc}$ increased slightly in all cells. $R_{sc}$ reduced from 1350 to 912 Ω-cm$^2$ for the [No Cu –Yes CdCl$_2$]; for other cells it increased or stayed the same.

When presenting effect of stress on the trap system, we confine ourselves to two cells, both doped with Cu, one of treated and the other not treated with CdCl$_2$. It is seen that plots relating to the same trap states shift after stressing, indicating decrease in capture cross section, most significant (almost two orders of magnitude) for H1 and E2 states in the [Yes Cu – Yes CdCl$_2$] cell (Fig. 3.6) Changes in activation energy are less significant. They are within the accuracy of measurements and data treatment, except for H2 state that we are prone to attribute to the $Cu_{Cd}$ defect. For this state $E_a$ increases after stressing from ~0,3 to ~0.35 eV. By the way, just in this range vary the estimates of $E_a$ for $Cu_{Cd}$ acceptor in Ref. 21, obtained from Hall coefficient temperature dependencies in CdTe:Cu single crystals.
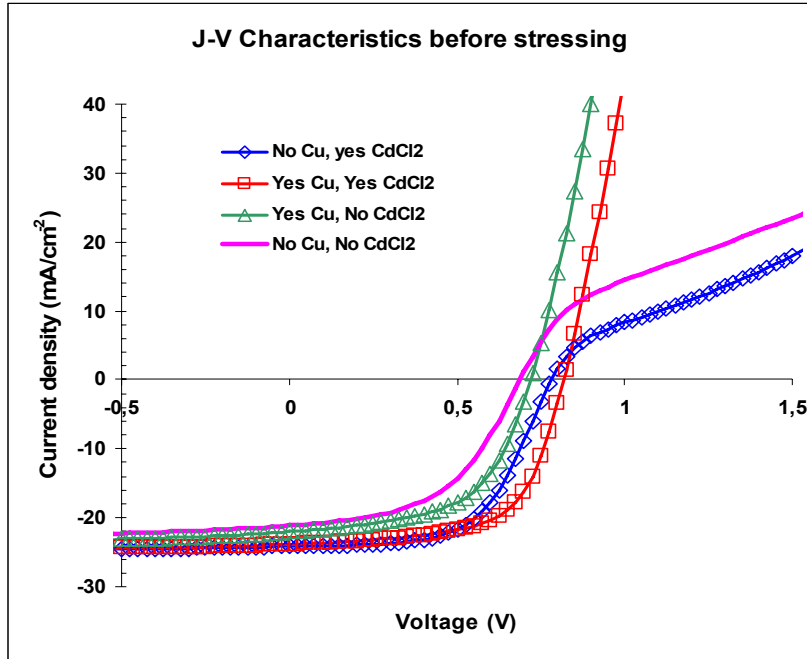
**(a)**
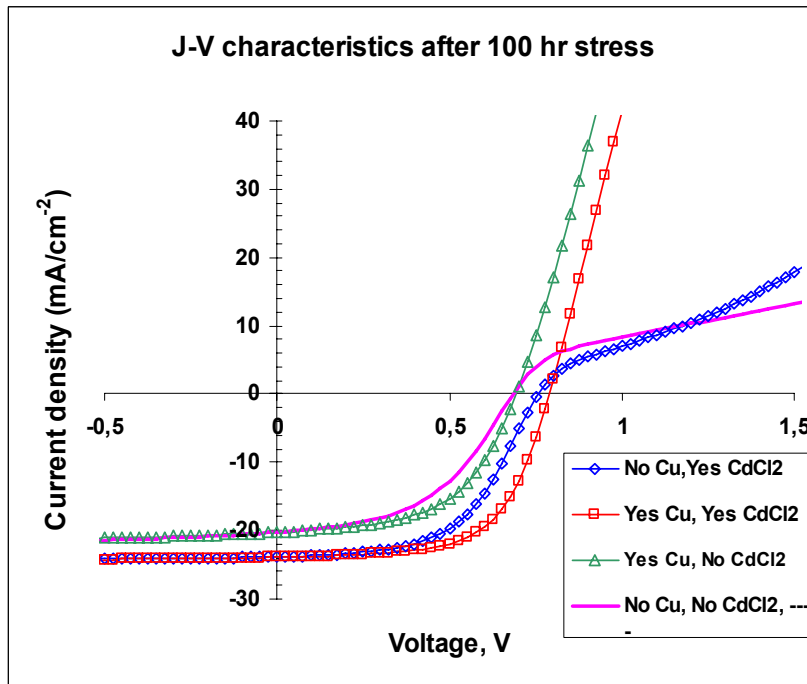


**(b)**

**Fig. 3.5.** Current-Voltage characteristics of [No Cu – Yes CdCl$_2$] and [Yes Cu – Yes CdCl$_2$]. cells. (a) – before stress, (b) – after stress.
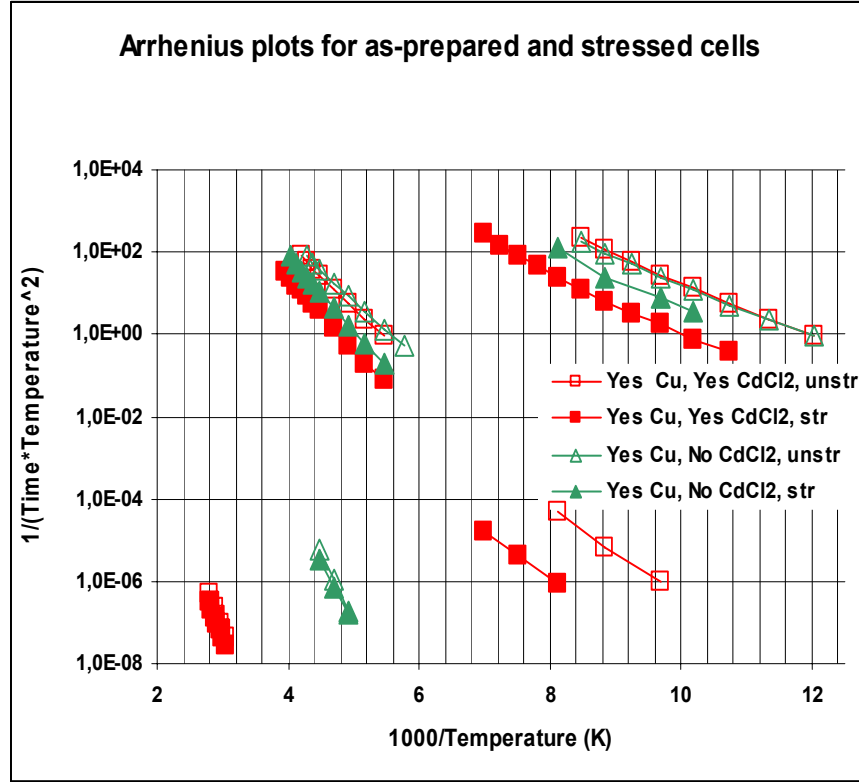
**Figure 3.6** Arrhenius plots for cells [Yes Cu – Yes CdCl$_2$] and [Yes Cu – Yes CdCl$_2$] before (empty marks) and after stress (filled marks).

Table 3.5 shows the tendencies of the trap density changes due to stress. As previously, we suppose that the transient capacitance magnitude could be used as an indicator.

**Table 3.5.** Transient capacitance $C_t$ for various types of traps before and after stress

| | Cell type | | | |
|---|---|---|---|---|
| | Yes Cu – Yes CdCl$_2$ | | Yes Cu – No CdCl$_2$ | |
| | Before stress | After stress | Before stress | After stress |
| Trap type | $C_t$ (nF/cm$^2$) | | | |
| H1 | 2.2 | 1.0 | 1.1 | 0.02 |
| H2 | 1.0 | 1.4 | 0.45 | 0.25 |
| H5 | - | - | 0.08 | 0.025 |
| H6 | 7.5 | 9.5 | - | - |
| E2 | 0.025 | 0.06 | - | - |

The Table shows that the $C_t$ value (hence trap density) for H1 states visibly decreases after stress. In the CdCl$_2$ treated cell $C_t$ reduces more than two times, in the non-treated cell about fifty times. The following possible explanation could be proposed for this difference.

- Let us assume, as in Sec. 3.2.2, that the H1 group is actually composed by states of almost the same activation energy (0.13-0.14 eV) provided by two types of defects: cadmium vacancies and $(V_{Cd} - Cl_{Te})$ A-centers. Contribution of A-centers into H group is comparable to that of cadmium vacancies in the CdCl$_2$ treated cells, whereas in the untreated cells concentration of the former is much less than of the latter.

- Probably diffusion of Cu during stressing causes its spatial redistribution. This, in turn, leads to a significant decrease in the $V_{Cd}$ density near location of the crossing point ($E_t = E_F$) due to replacement of $V_{Cd}$ by $Cu_{Cd}$. Therefore density of H1 states reduces dramatically in the untreated cell where majority of H1 states are produced by $V_{Cd}$.

- Let us suppose that density of A - centers is much less sensitive to concentration of Cu atoms. Their contribution into the H1 density becomes dominant after replacement of $V_{Cd}$ by $Cu_{Cd}$ and defines the limit to which $N_{H1}$ reduces due to stressing.

We have suggested in Sec. 3.2.2 that the H2 states ($E_a \approx 0.3 eV$) are provided by the $Cu_{Cd}$ acceptor defect. Table 3.5 shows that the $C_t$ value (also $N_{H2}$) is lower in the treated cell than in the untreated one. Moreover, in treated cell it increased by 40 % after stress, while reduced by 45% in the untreated cell. Probably these facts should be interpreted as manifestation of interaction of Cu-related and Cl-related defects. In particular, the $Cl_{Te}$ donor states should compensate the $Cu_{Cd}$ acceptors. On the other hand, we should consider possible influence of auto-compensation these two defects. Spatial redistribution and possible mutation of both types of defects (e.g., transitions $Cu_{Cd} \leftrightarrow Cu_i$ controlled by Fermi energy) can be behind observed differences and stress effects. However, due to the complexity of phenomena and lack of direct information of the defect nature, its concentration and spatial distribution, explanations and conclusions are still too speculative and ambiguous.

The third type of states, H6 ($E_a \approx 0.8 eV$), was observed only in the cell treated both with Cu and CdCl$_2$. The estimated density, $N_{H6}$, at crossing point exceeds $10^{15} cm^{-3}$. In the cell doped with Cu but untreated, H6 trap was undetectable. Possible explanation is that H6 is provided by some complex that involves both Cu and Cl. Note, the stress led to increase in $C_t$ by about 30%. This high density trap level located close to the CdTe midgap might be an effective recombination center and deserves to be studied thoroughly.

While H1, H2, H6 states in Cu doped cells demonstrated rather high concentrations, thus affecting cell performance and stability, other states had much lesser density, or even were undetectable. In future studies, H1, H2, H6 states should be studied more thoroughly in larger number of cells, as prepared as well as subjected to stresses of longer duration and under various conditions.


## 3.5    Summary

- Combination of admittance spectroscopy and capacitance transient measurements allowed detection and characterization of multitude of deep electronic states (traps) in CdTe solar cells.

- The set of detected traps, their signatures, and evolution caused by stress, vary with the post deposition treatment (Cu/no Cu and/or CdCl$_2$/no CdCl$_2$).
- Traps of higher density include those labeled as H1, H2, H6 with activation energy of ~0,13eV , ~0.3eV, and ~0.8eV respectively.
- The H1 group was observed in all cells and may be attributed to the mixture of two acceptor type defects: $V_{Cd}$ and $(V_{Cd} - Cl_2)$ A-center with indistinguishable activation energies. In CdCl$_2$ treated cells both defects are presented in comparable concentrations, in untreated cells $V_{Cd}$ strongly dominates.

- The H2 states were detected only in Cu doped cells and were attributed to $Cu_{Cd}$ acceptor defects. In CdCl$_2$ treated cells the H2 density is higher, maybe due to the auto-compensation effect with $Cu_{Cd}$ acceptors and $Cl_{Te}$ donors involved.

- The H6 states were detected in cells CdCl$_2$ treated and then doped with Cu. With only one or none of these treatments the states were undetectable. It was assumed that the H6 state is provided by some complex defect with Cu and Cl involved. Concentration of these states/defects was estimated to be in the range of $10^{15} cm^3$.
- Concentration of detected states has changed after stress (1 Sun light, $100^0C$, 100 hours). Variation in the changes from trap to trap and cell to cell could be  explained in the way consistent with the states attribution to the specific defects.

## 4. SCANNING TUNNELING MICROSCOPY AND LOCAL SPECTROSCOPY OF THE BACK CONTACT INTERFACE

## 4.1. High Resolution Current Mapping at $p^+$-ZnTe/p-CdTe Back Contact Interface

A number of microscopic probes have been used successfully on polycrystalline solar cell materials. Examples are cathodoluminescence spectroscopy [7] and near-field scanning optical microscopy [11, 72]. Under favorable circumstances these techniques can map carrier generation/recombination or impurity concentration with spatial resolution of about 100 nm. Scanning capacitance microscopy in an atomic force microscope has recently been used to determine the potential distribution at single grain boundaries, critical to charge collection and recombination [70]. A key device property, carrier transport across contacts and in the absorber itself, remains poorly understood, yet is crucial for optimizing the short-circuit current and efficiency of a solar cell.

We have demonstrated a novel technique, charge injection spectroscopy (CIS) in a scanning tunneling microscope (STM), which can provide detailed maps of carrier transport near the interface between the polycrystalline absorber layer of a thin film solar cell and an adjacent ohmic contact. We use this technique to image near-surface transport between a p-CdTe surface and a $p^+$-ZnTe back contact interface with lateral resolution below 20 nm, about 2 orders of magnitude below the absorber grain size. Charge transfer between the $p^+$-ZnTe contact and the p-CdTe absorber is highly non-uniform, and involves large areas with roughly constant high resistance coexisting with nanoscale high-conductance pathways. A majority of the cell current flows along these pathways, which are often localized at grain boundaries, thus highlighting an important role of grain boundaries as efficient near-contact transport channels. Conducting paths found within a few of the grains suggest that specific intragrain defects may also cause a lowering of the contact resistance. Identification and promotion of such beneficial defects could result in substantially reduced overall contact resistance.

The samples used were standard CdTe/CdS heterojunction structures in 'superstrate' configuration from First Solar, LLC (Fig. 4.1) with our standard ZnTe:Cu contact. STM experiments were performed on the ZnTe surface layer under dark conditions and at room temperature, using a home made tunneling microscope operating in air or high vacuum. Electrochemically etched tungsten tips were used as emitters, while the STM collector contact was made to exposed sections of the $SnO_2$ cell front contact. In this configuration, we simultaneously measured the surface topography via constant-current STM and current-voltage (I-V) spectra on a regular grid of points across the field of view (FOV). From the measured I-V spectra, current values at constant bias voltage were extracted to produce high-resolution two-dimensional current maps, I(x,y). STM measurements were complemented by XTEM, performed in a Philips CM200 microscope at 200 keV beam energy, on samples prepared by tripod polishing and brief low-energy ion milling.

Fig. 4.1 illustrates the layout of our STM experiments. With emitter and collector contacts on opposite sides of the solar cell, carriers injected from the tip into the $p^+$-ZnTe contact layer have to undergo transport into and through the entire device structure to contribute to the overall current measured at the $SnO_2$ collector contact. Conventional STM on single crystals is surface sensitive, and contrast is usually dominated by surface states of the sample. On a highly heterogeneous polycrystalline device structure, additional contrast may arise if the overall local conductance of contact and cell is low, i.e., comparable to the conductance of the tunneling gap.

Suppose, for example, highly insulating grains with a substantial potential barrier at the ZnTe/CdTe interface, separated by grain boundaries with higher conductance and locally reduced contact barrier. Carriers injected into the ZnTe layer above a grain [Fig. 4.1, position (1)] will then spread in the ZnTe to the surrounding grain boundaries, where they are transferred into the p-CdTe absorber and to the STM collector contact. The equivalent electrical resistance in this case is a sum of the tunneling resistance [$R_t$], the position-dependent resistance to carrier spreading in the ZnTe [$R_s(x,y)$], and the equivalent resistance of current transport across the contact and through the cell [$R_c$]: $R_{tot}(1) = R_t + R_s(x,y) + R_c$. If, however, the tip is placed over an area with low contact barrier [e.g., a grain boundary, position (2)], no spreading in the ZnTe occurs and only two terms remain: $R_{tot}(2) = R_t + R_c$.
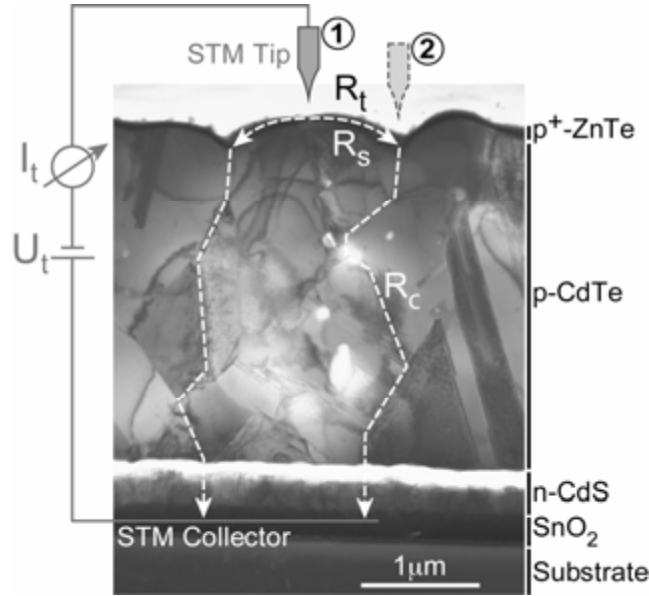


**Figure 4.1** XTEM cross-section of a p-CdTe/n-CdS solar cell, showing the cell structure and illustrating the contact configuration used in our STM measurements.

Measuring, at constant tip-collector bias and as a function of tip position, the current injected into the cell should thus provide detailed maps of non-uniform carrier transport near the ZnTe/CdTe back contact interface. In particular, this technique should be sensitive to high-conductance pathways due to locally reduced contact resistance, e.g., at grain boundaries or in 'defective' grains. A relatively resistive contact layer (such as the ZnTe contact used here) is key for obtaining current contrast, since for a highly conductive (metallic) overlayer the spreading resistance $R_s(x,y)$ is small compared to the other resistance terms, thus providing negligible contrast. Other STM-derived techniques, such as ballistic electron emission microscopy have been developed to map the local height of potential barriers, e.g., at Schottky contacts on single crystal substrates. In comparison to this three-terminal technique, CIS is relatively simple and can be used to reliably map local contact resistances on complex polycrystalline photovoltaic devices.

Fig. 4.2 (a) shows a current map obtained at $U_t = 2V$ on a $p^+$-ZnTe capped p-CdTe/n-CdS solar cell. Dark (bright) shading in the image marks areas in which the current injected into the cell is low (high).
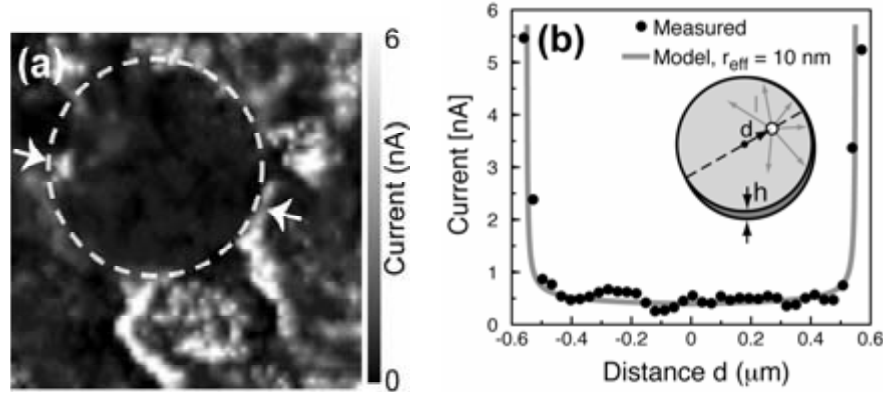


**Figure 4.2** Identification of the contrast mechanism in STM current maps on CdTe/CdS cells. (a) Grayscale STM current map at 2V bias (field of view: $2 \times 2$ $\mu m^2$). (b) Comparison of line profile across a single grain (between arrows in (a)) with model calculations for an effective injector radius of 10 nm. The inset illustrates the geometry assumed in the calculation.

The image shows substantial contrast in the form of large areas with uniformly low current, separated by bands of much higher conductance. We can use the data obtained on a single uniform grain (circle) and the surrounding grain boundary to verify the contrast mechanism proposed above, and to estimate the spatial resolution achievable in CIS. The expected current contrast due to a position dependent spreading resistance $R_s(x,y)$ was calculated for a simplified geometry of circular slab of ZnTe (thickness h) surrounded by a collector contact at its periphery (inset of Fig. 4.2 (b)). Current I injected at a distance d from the center of the slab will spread toward this collector contact. We have numerically computed the total resistance to current flow in the slab, as a function of the position and effective radius ($r_{eff}$) of the injector. The resulting current at constant injector-collector bias $U_t$ was compared with the experimental data. For $r_{eff} = 10$ nm, we obtain excellent agreement between the computed and observed current distribution across a single grain. This result not only confirms the assumed contrast mechanism based on spreading in the ZnTe overlayer, but suggests that it should be possible to map preferential conducting paths near the absorber/contact interface with lateral resolution of about 20 nm.

Simultaneous measurements of sample topography and of current maps provide information on the spatial distribution of high conductance pathways at an ohmic contact to a solar cell, in our case at the p+-ZnTe/p-CdTe interface. A correlation of topography with current contrast is given in Fig. 4.3. Panels 4.3 (a) and (b) show the simultaneously measured topography and current image within a field of view of $6 \times 6$ $\mu m^2$. The topographic scan [fig. 4.3 (a)] shows rounded elevated features, typically about 1.5 $\mu m$ in diameter, separated by well-defined deep trenches. Based on comparison with XTEM, we associate the elevated areas with individual grains, and the intervening trenches with grain boundaries. The current map [Fig. 4.3 (b)] shows large areas with roughly constant low current (dark), indicative of sample areas with low transmission probability across the ZnTe/CdTe interface, alternating with narrow, elongated conducting bands (bright) in which the contact is highly transparent.
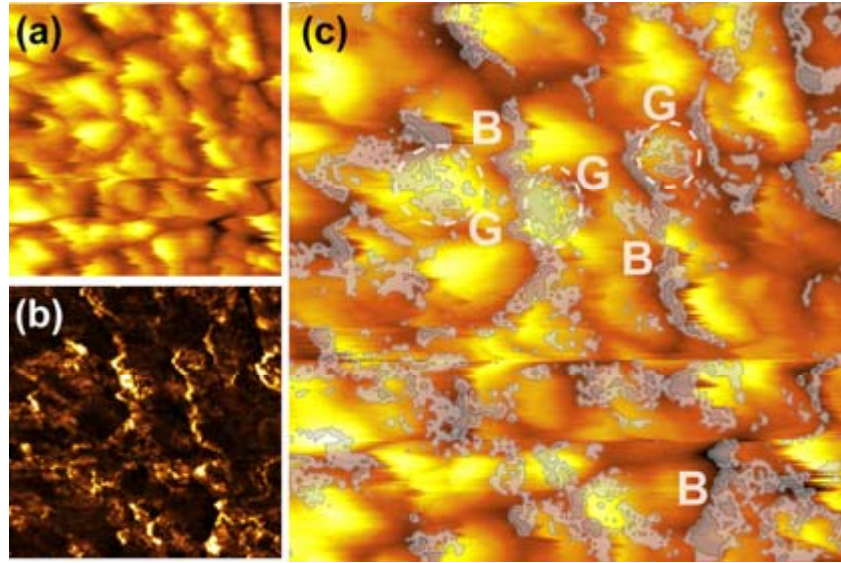
**Figure 4.3** (a) Topographic image obtained on a ZnTe capped CdTe/CdS cell (field of view: 6 × 6 $\mu m^2$, height scale: 0.7 $\mu m$). (b) Current map of the same region at 2V tip-collector bias (current range: 0 – 6 nA = $I_{max}$). (c) Overlay of topographic data (color) with contours of the 2V current map. Light and dark gray areas, indicating current levels of 0.3 $I_{max}$ and 0.85 $I_{max}$, respectively, trace troughs associated with grain boundaries (B) and some 'leaky' grains (G).

The position of these conducting paths is strongly correlated with grain boundaries. Fig. 4.3 (c) illustrates the correlation between topographic features and conductive pathways via a superposition of the topographic image with contours of constant current obtained from the current map. Regions of high current have a strong tendency to trace grain boundaries (B). The intragrain material generally shows rather uniform, low current, i.e., appears to be substantially more resistive than grain boundaries. An exception is a few 'leaky' grains (G), in which a high density of microscopic conducting paths are observed.

Our data show substantial contrast on a nanometer length scale in the local transport properties of the $p^+$-ZnTe/p-CdTe interface of p-CdTe/n-CdS solar cells. The observed features appear unrelated to the grain structure of the small-grain ZnTe contact, but instead trace the topography of the underlying CdTe with its much larger grain size. This observation confirms that our data indeed map transport across the ZnTe/CdTe interface, and in the CdTe absorber near this interface. Current flow between absorber and back contact is highly non-uniform, with few low-resistance areas likely carrying a large fraction of the overall current of the cell. A majority of these areas trace grain boundaries, which indicates that grain boundaries may play a crucial role as conducting channels for carrier transfer into the cell back contact. Given that performance of polycrystalline CdTe/CdS solar cells is superior to single crystalline devices, a beneficial role of grain boundaries in carrier collection and transport, see e.g. [71, 11]. We provide the first observation of preferential current transfer into contacts via grain boundaries. Importantly, some intragrain material also shows efficient current transfer into the contact. Comparison with XTEM images suggests that structural defects or an accompanying segregation of impurities may be responsible for a local lowering of the contact barrier within some grains. This observation points toward a potential route for achieving substantial gains in cell efficiency

via lowering of the back contact resistance by promoting these beneficial defects, and concomitant increases in short circuit current and fill factor.

## 4.2.    New Experimental Capabilities

While the initial experiments discussed above involved local I-V measurements between ZnTe-capped CdTe/CdS cells in air, we have developed new experimental capabilities, direct conductance (dI/dV) mapping and imaging in high vacuum. These new capabilities will be discussed briefly below.

### 4.2.1.  High-resolution conductance mapping

We have developed the capability of obtaining, simultaneously with topographic images, conductance (dI/dV) curves on a regular grid within the image field of view. Similar to the I-V measurements, from which high-resolution current maps could be derived, the dI/dV data allow us to produce maps of local conductance, dI/dV(x,y), near the back contact of a thin film solar cell.

First results were obtained on a new batch of $p^+$-ZnTe capped p-CdTe/n-CdS solar cells with layout as shown in Fig. 4.1. Our previous measurements showed symmetric I-V curves, i.e., negligible rectification. In our new data, in contrast, a strong dependence of conductance on bias polarity (i.e., rectification) is observed, the origin of which requires further clarification. Fig. 4.4 shows representative conductance curves measured within a grain, and at a grain boundary of a device that has undergone $CdCl_2$ treatment and Br:MeOH etching prior to evaporation of thin Cu and ZnTe layers.
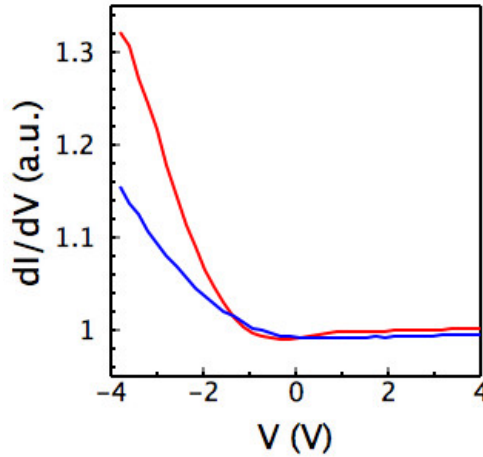


**Figure 4.4** Conductance spectra obtained at a grain boundary (red) and in intragrain material (blue). V > 0 corresponds to reverse bias of the main CdTe/CdS junction. Negative (positive) bias in fig. 4 corresponds to forward (reverse) bias of the p-CdTe/n-CdS junction of the cell.

We have obtained simultaneously measured maps of topography and local conductance, as shown in Fig. 4.5. The topographic image (Fig.4.5 (b)) shows, as before, rounded grains with diameter of about 1 μm, separated trenches that we identify as grain boundaries. The

conductance map at positive bias (Fig. 4.5 (a)) shows the same general contrast distribution that was observed in current maps: high conductance preferentially near grain boundaries, uniform low conductance when the tip is placed over a grain. The conductance image at negative bias, however, deviates from this behavior. Instead of conducting paths near grain boundaries, we observe contrast that correlates much less with topographic features.
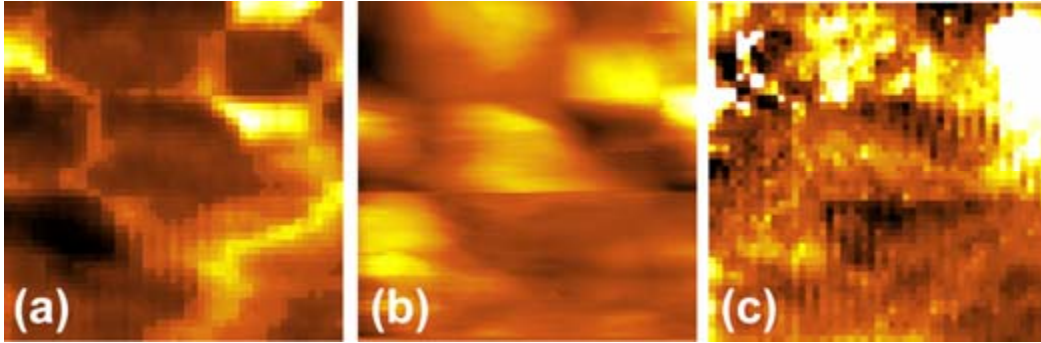


**Figure 4.5** Simultaneously measured topography and conductance maps (FOV: $2 \times 2$ μm). **(a)** dI/dV at V = +1 V (bright: high conductance). **(b)** Topography. **(c)** dI/dV at V = - 2.3V.

If we assume that the conductance images of Fig. 4.5 reflect high conductance pathways across the ZnTe/CdTe interface, we thus conclude that in these new devices clear differences exist between electron and hole transport across that contact. Currents of hole (majority carrier) injection into the CdTe are generally low, and strongly localized at grain boundaries. A substantial barrier to hole injection appears to exist at the contact to intragrain material. Electron injection, on the other hand, is more efficient and often shows minima at the grain boundary itself, surrounded by areas with higher conductance. A conclusive interpretation of these initial results of dI/dV maps requires additional measurements and modeling, and will be presented in the future.

## 4.2.2  Measurements in high- and ultrahigh vacuum

Most of the results shown above were obtained in a compact STM system, operating in air. Etched tungsten tips were generally used as probes for these measurements, since they can be formed into very sharp tips, required for scanning the rough surface of a solar cell. However, tungsten tips tend to oxidize over the extended times required to scan high-quality conductance maps. We have thus changed our experimental setup to be able to measure in high- or ultrahigh vacuum (Fig. 4.6). Incompatible materials, such as solder joints, were replaced with vacuum (UHV) compatible materials that can withstand baking temperatures up to 150°C required for rapid pump-down to UHV. In addition, we have implemented a heating system that will allow us to anneal samples in vacuum, for surface cleaning, or to induce grain regrowth or impurity diffusion.

**Figure 4.6** Compact UHV STM system for imaging and spectroscopy on solar cell materials.

## 5. NEAR FIELD SCANNING OPTICAL MICROSCOPY OF PHOTO-CURRENT AND PHOTOLUMINESCENCE IN CdTe SOLAR CELLS

Our prior studies of thin film CdTe cells using near-field microscopy (NSOM) have shown that cross sectional photocurrent collection (PCC) measurements of cleaved (or broken) cells can provide high spatial resolution information on the width of the collection region, the sulfur content in the CdTe, and diffusion of S into the material [11]. During this contract we have worked upon extension of this technique capabilities. ***Particularly, the NSOM on sub-grain length scales, both cross-sectional and in-plane, has been developed providing imaging photocurrent collection and also photoluminescence***. NSOM of electroluminescence is under development.

As shown in Sec.1, using the signatures of specific defects in the EL and PL spectra one can study spatial distribution of the defects on the ~10μm scale. With NSOM the same is possible to do on the sub-grain lengthy scale. PL can also provide information about the spatial distribution and nonuniformity of recombination processes.

One of the reasons for this development work was to allow a broader range of samples to be characterized. In our previous studies, the presence of the glass superstrate precludes high spatial resolution photocurrent in plan view. With photocurrent, we are restricted to samples fabricated into a cell. With PL we can study films in plan view before back contact fabrication. It would be advantageous, to be able to study films at a series of steps along the fabrication process to learn what each step does on a microscopic scale.

In this section we present the data that illustrate new possibilities we got for studying photo-electric properties of material on the sub-grain scale. Systematic NSOM studies of cells and constituent films, correlated with variation in processing and stress procedures, are the subject of continuing and planned for the near future experiments.

## 5.1. Plan-View Imaging of Photocurrent

### 5.1.1. CdTe/CdS cell

The plan-view NSOM image obtained once [11] on a CdTe cell, after an access for the optical probe was provided to the TCO surface (mechanical polishing and etching of glass), demonstrated in some locations higher PCC for the grain boundary regions than for the grain bulk. This result (if confirmed in other experiments) considered to be of significant importance providing better understanding of the grain boundary (GB) effect on the cell performance. The PCC plan-view studies were partially initiated by speculations on possible beneficial effects of GBs later presented in [13].

It was very difficult to repeat these in plane studies because CdTe cells are usually of a superstrate configuaration. The early technique we used for the TCO exposure was complicated and usually damaged a cell. The problem was solved recently after the University of Toledo provided us with a cell of a substrate configuration. The CdTe/CdS device has been grown on a Molybdenum substrate using an RF sputter deposition, then went through a $CdCl_2$ treament followed by depositing ITO via RF sputtering. A HeNe laser with wavelength of 632.8 nm was used as the excitation source in the photocurrent measurements. Results of this experiment (Fig. 5.1) consistently show a reduced PCC from grains as compared to the intergrain regions. Several images taken at random points on the device show qualitative agreement with one another and demonstrate on average a 5% difference in the photocurrent between these regions in favor of grain baoundaries. The 2x2 $\mu m^2$ images shown in Fig. 5.1 were generated with two different programs to aid in the visualization of the topography vs. photocurrent where the topography is on the left and photocurrent is on the right. As one can see, the photocurrent in the two higher grains is lower with an increase in photocurrent around the grains.

Recently, the NSOM measurements of the PCC on VTD CdTe cells with the transparent back contact, ZnTe:Cu, also showed enhanced PCC from the intergrain regions [72].. The investigated cell was of a superstrate configuration. Thus, a similar effect of grain boundaries on PCC was observed on differently processed cells with the light absorbed close to the CdTe/CdS interface (our case) and close to the top surface of CdTe [72].
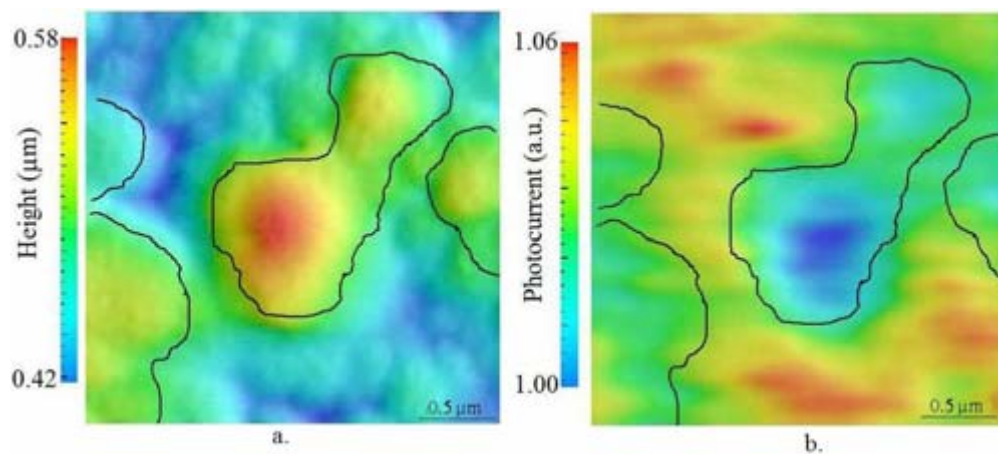


**Figure 5.1.** Correlation between a.) topography and b.) photocurrent plan-view images on CdTe cell of substrate configuration fabricated at the University of Toledo

### 5.1.2.  CIGS/CdS cell

As a substrate configuration is very suitable for in-plane imaging of PCC, a CIGS/CdS cell was also tested with NSOM. The primary reason for investigating this sample was to check whether the area where the ITO and CdS were lifted off contributed considerably into measured photocurrent and hence into estimated cell efficiency than the traditional scribing technique. The CIGS cells were prepared with standard procedure, then the new etching process was applied and efficiency was measured.  Several scans were taken in the etched  region at different locations that show very little or no PCC in this region.  Fig. 5.2 shows an image obtained with  the 26x26 $\mu m^2$ scan and the excitation wavelength of 632.8 nm. The bottom left corner presents the region with the CdS and ITO still attached. Toward the top right corner, the ITO and CdS have been lifted off.  The image on the left is the topography and the image on the right is photocurrent.
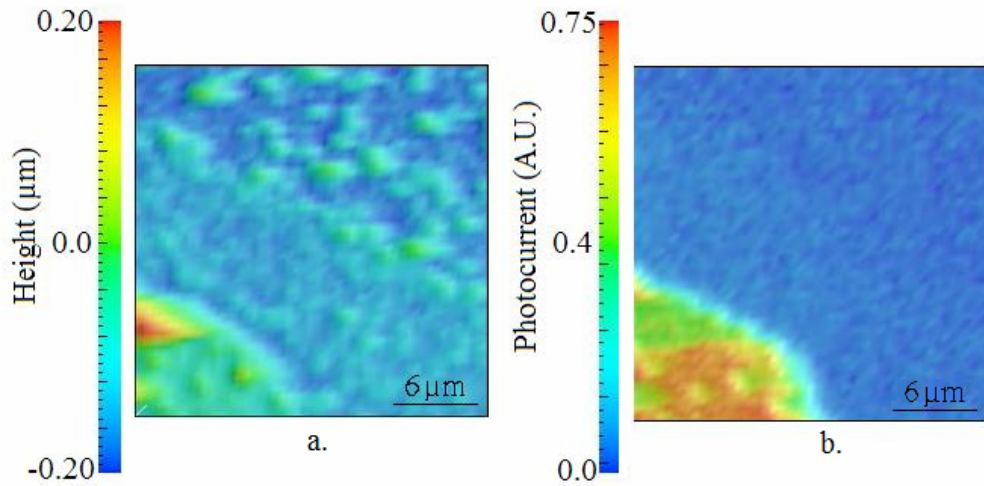


**Figure 5.2.**  Correlation between a.) topography and b.) photocurrent on CIGS at the etch step.

Fig. 5.3 shows significant difference between images obtained with the excitation wavelengths of 6.32.8 nm and 457 nm.
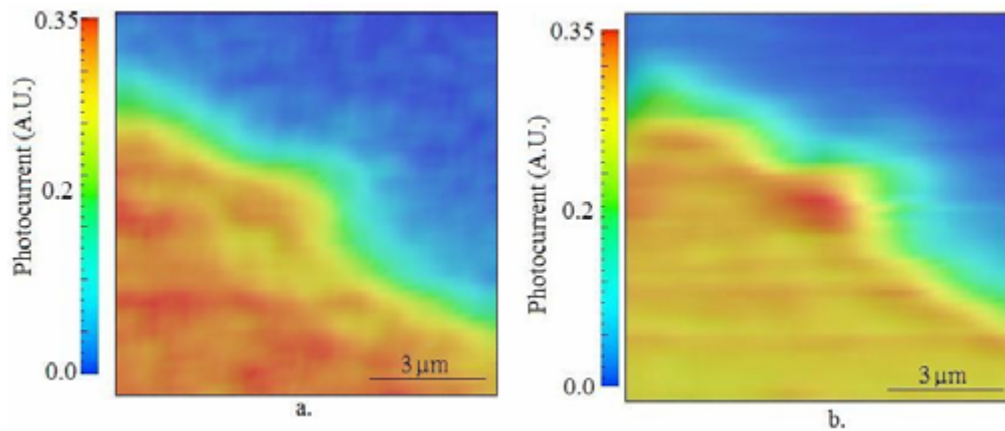


**Figure 5. 3**  Difference in PCC at the etch stop for wavelengths of a) 632.8 nm and b) 457nm

The PCC studies were conducted on the CIGS cell. Fig 5.4 shows the correlation between the topography and the PCC images of the same fragment of the cell area. The scan range is of 5x5 μm² with the outline of the grains marked with a black line in both images. An increase in photocurrent at the grain boundaries is seen relative to the grain interior. This is in contrast to a report by McDaniel and Hsu [73], in which they found that cells with grains larger than 10 μm or smaller than 1μm showed decreased photocurrent at the grain boundary as compared to the grain interior. However, the cells they studied had lower efficiencies than those used in this experiment, and they also had a much thicker (450 nm) TCO layer.
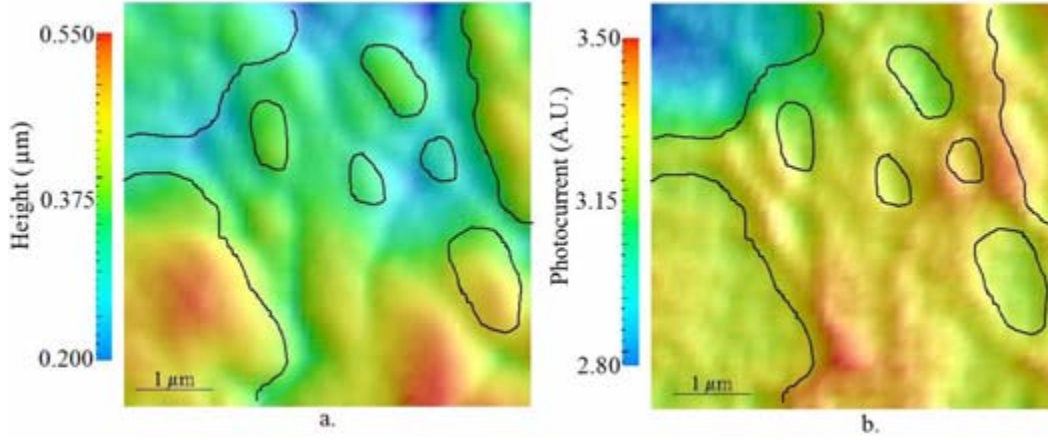


**Figure 5.4**   Topography (a) and photocurrent collection (b) images for the CIGS cell

## 5.2    NSOM Studies of Photoluminescence on CdTe/CdS Cells

Recently we have become able to perform room temperature NSOM photoluminescence (PL) measurements on the substrate configuration UT CdTe cells. Fig. 5.5 shows the near- field PL spectrum excited by the 488 nm (the photon energy is above the CdS bandgap) laser irradiation  through the front TCO contact.

Two broad peaks are seen in the spectrum centered at the photon energy of 1.718 eV ($\lambda$= 722 nm) and 1.468 eV ($\lambda$==845 nm), above and close to the CdTe band gap, respectively. PL spectrum was also measured excited by irradiation with the wavelength ranging from 457 nm to 632 nm.  As the excitation source went to longer wavelengths, the magnitude of the high energy PL peak decreased gradually and disappeared altogether at 632 nm wavelength. One can conclude that this peak is generated in the CdS layer and apparently is generated by the band-to-defect level transitions, whereas the lower energy peak is generated in the CdTe layer and may be attributed to the band-to-band transitions. A significant difference in magnitude of the observed peaks is determined by the fact that the cell is irradiated from the CdS side of CdTe/CdS junction, hence the exciting light with $\lambda$=488 nm is absorbed predominantly by the CdS layer.

**Near-Field Photoluminesence of CdTe**
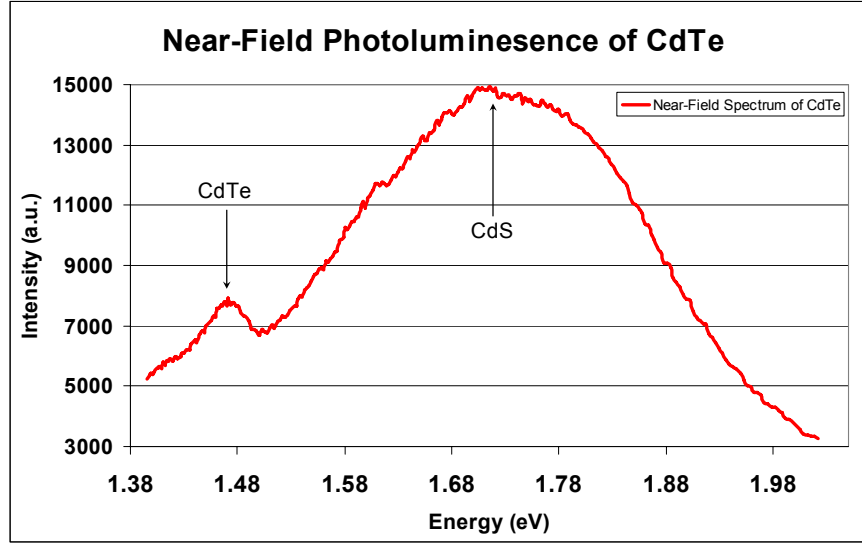


**Figure 5.5** Near field PL spectrum obtained on a cell of substrate configuration produced at UT. $\lambda_{excit.} = 488nm$. Measurements were done at nominal temperature of $25^0C$.

Fig. 5.6 shows the plan-view topography and PL images taken from the same fragment of a cell. The excitation source used to produce the PL was 488 nm and the images were not taken simultaneously therefore the two PL images show a shift due to the drift of the piezoelectric tubes. The PL from the CdS layer was taken with the spectrometer centered at 750 nm and spectral PL data was acquired between 712 nm and 774 nm, therefore allowing integrating PL intensity underneath the broad peak. As for the PL from the CdTe layer, the spectrometer was centered on 850 nm and spectral data was acquired between 829 nm and 866 nm. To demonstrate the similarity between two PL patterns, the CdS data was normalized to the CdTe thereby showing that the CdS follows somewhat the same pattern as the CdTe although there is a subtle difference.

The correlation between the PL and topography images is seen in two different length scales. The first characteristic length is of the order of at least several grain sizes, and possibly comes from the roughness of the Mo substrate. Shorter length scale, quite visible in the topography image, but also observable in the PL pattern, is of the order of a single grain size. The latter is much smaller for the films deposited with the RF sputtering than with CSS, VTD, Gas Jet, etc. The contrast in the PL intensity, better seen in the CdTe range, although small in both ranges, is mostly in favor of the grain boundary regions.
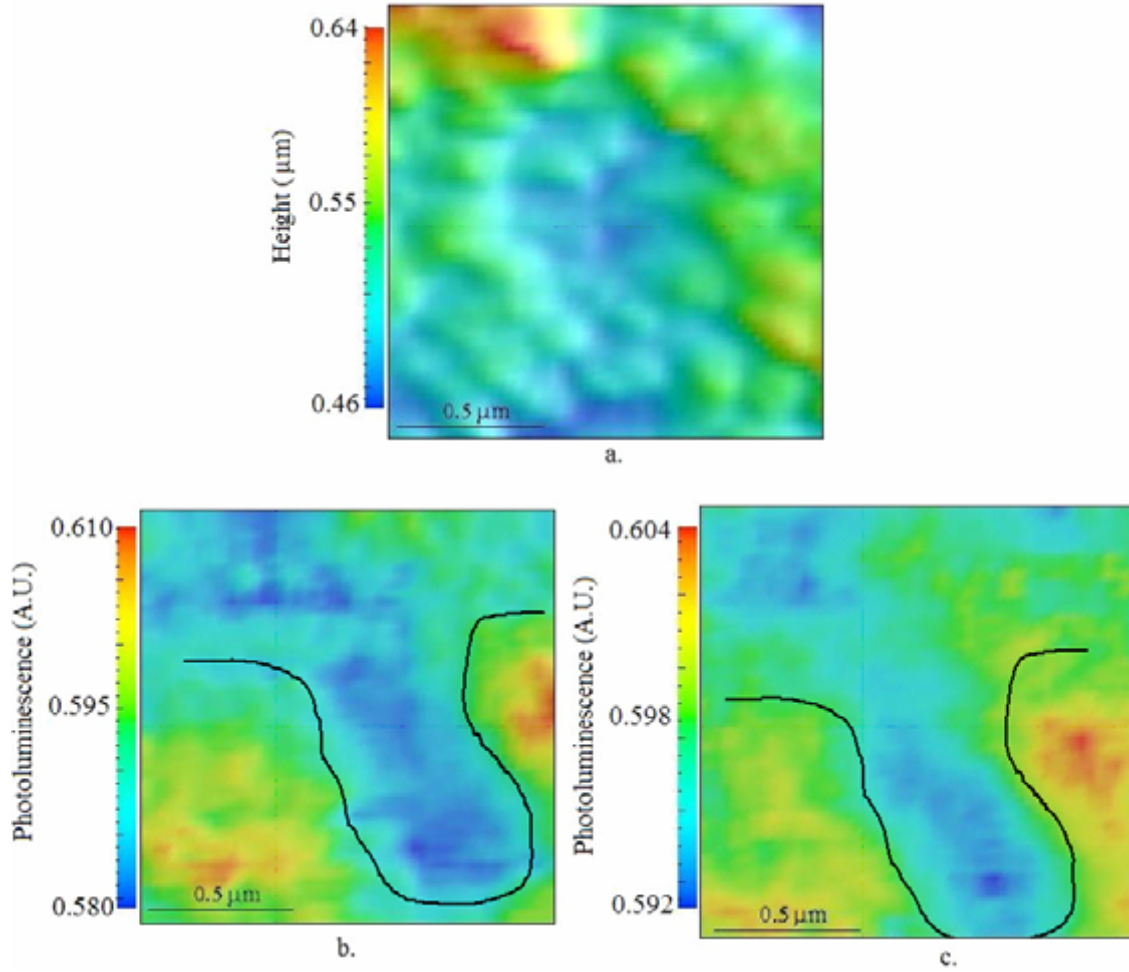
**Figure 5.6**  Correlation between topography (a) , CdS PL (b), and CdTe PL (c) in plan-view on the CdTe UT cell with the black line indicating the same PL structure in both spectrum.

The next experiment indicated that the NSOM PL image contrast could be controlled to some extent by applying bias voltage to a cell. Fig. 5.7 shows the NSOM PL spectrum excited with a source of $\lambda$=488 nm under zero, forward and reverse bias.   Fig. 5.8 presents the NSOM PL images for $\lambda$=750 nm and $\lambda$=850 nm taken from the same area at the reverse, zero and forward biases. The PL excitation source was of $\lambda$=488 nm.
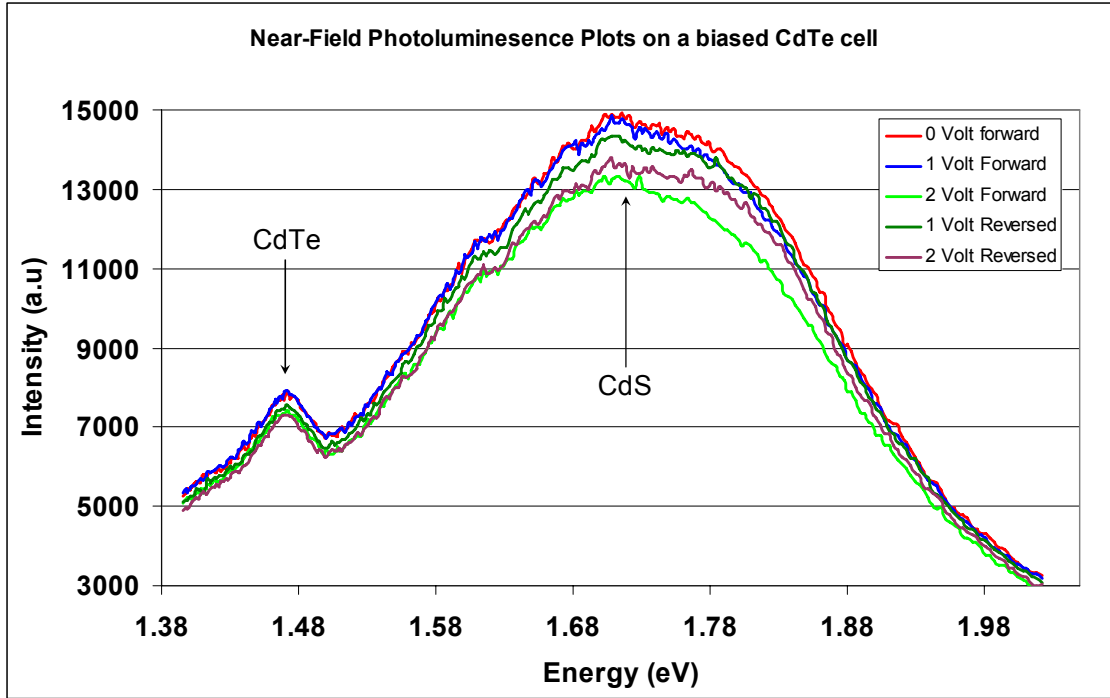
**Figure 5.7**  Effect of bias on the NSOM PL images.
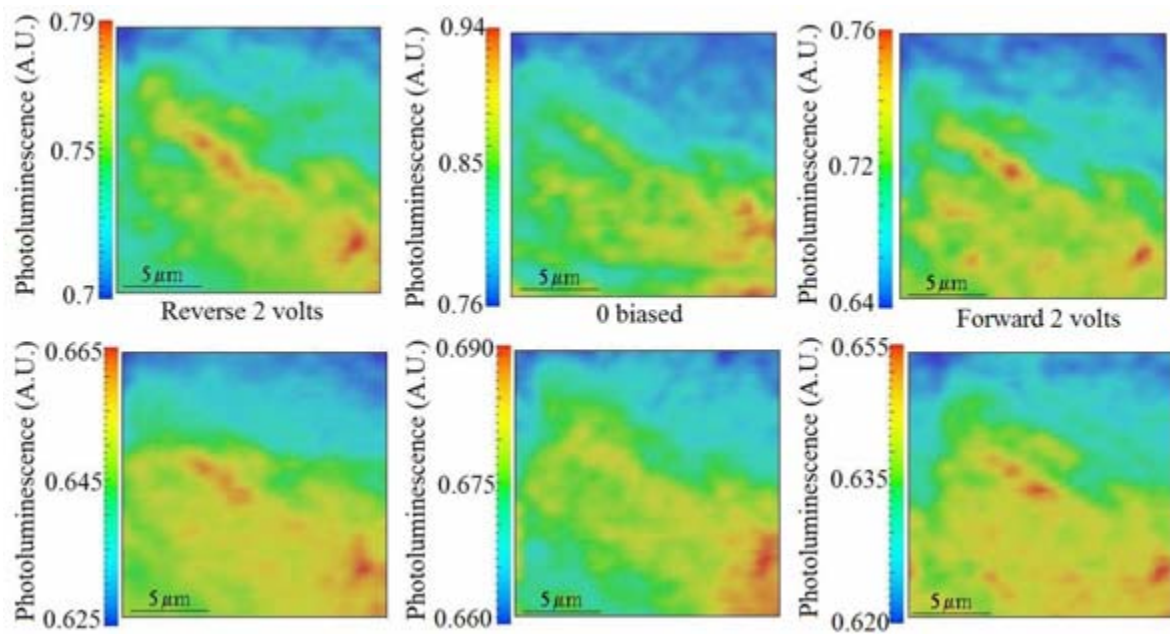


**Figure 5.8**   Spatial distribution of the NSOM PL intensity at the bias voltage indicated in the Figure. The PL was excited by the light of λ=750 (top images) and of λ=850 nm light (bottom images).

The effect of bias is obvious. Both reverse and forward biases enhanced the mean PL intensity and redistributed it spatially. In particular, in some areas the contrast has changed between what we believe to be the grain boundary region and the grain bulk. For example, the mean PL intensity in the II quadrant of images from the biased cell (for both positive and negative bias) is higher than that from the unbiased cell. Then, in the same quadrant one can see enhanced PL from the chains of circular spots which represent grains according to the topography image.

It might be that by changing conditions of the experiment, e.g., by using the excitation source of lower photon energy that will be absorbed only in CdTe, we can have stronger control of the PL images so that they better manifest spatial non-uniformity of PL. These studies are now conducted in our laboratory.

Finally, cross-sectional measurements have been made on the CSM CdTe devices were grown with GJD. The results obtained from this experiment are shown in Fig. 5.8. The top left image is the topography with the glass on the left side and the device on the right side. This is more easily seen in the top right PL image in which the glass is the blue part of the image and the device can be seen starting in the middle. This image is a scan of 3x3 microns. The spectrometer was measuring PL only in the CdTe range. The bottom image shows the combined PL and topography images. PL is represented by the color and topography with the texture.
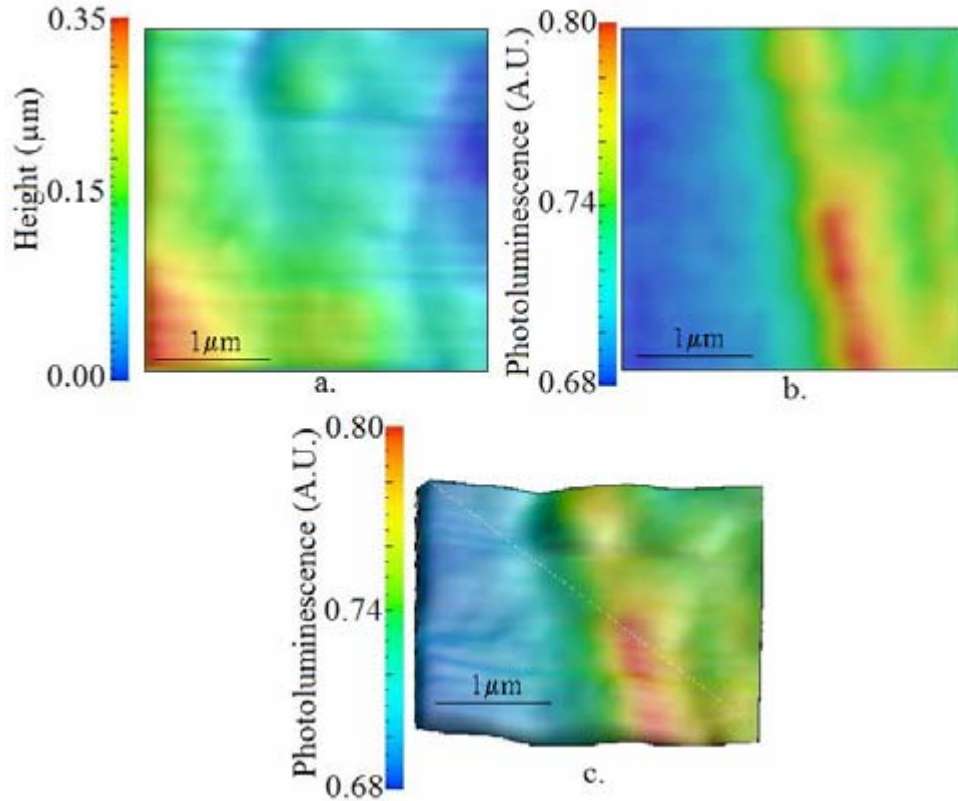


**Figure 5.9** Cross-sectional image of CSM CdTe devices with a.) topography, b.) PL of the CdTe spectral peak and c.) combination of PL and Topography with PL represented by the color and topography with the texture.

As expected, the maximum PL intensity is observed from the CdTe portion closest to the window layer from which the exciting light comes. Reducing of the incident light intensity due to absorption in CdTe causes the PL intensity fading with distance. Probably, more interesting and instructive could be nonuniformity observed in PL in the direction parallel to the device/glass boundary, that is at supposedly the same distance from the window layer. However it is too early to make some conclusions based on still preliminary measurements.

## 6.  CELL PROCESSING

In this Project the modification of both of our deposition techniques (electrodeposition, ED, and gas jet deposition, GJD) were undertaken. This was driven by efforts to improve our ability to produce cells rapidly and with sufficient control over all conditions to yield high reproducibility. First, the work has concentrated on increasing both the flexibility of the CdTe deposition systems (small areas and easily modified source materials) and the uniformity of the deposited film, however maximizing of device efficiency was also a goal of these activities.

### 6.1.  Electrodeposition

Previously the CdTe electrodeposition at CSM was conducted using a 4-electrode system with a 20 liter bath [74]. This system was donated by Ametek where it was used as a pilot plant. While good quality CdTe/CdS solar cells were produced at CSM in the past (NREL verified best of 12.9%), it has been difficult to maintain the system, and its large solution volume created a large amount of hazardous waste each time the bath composition had to be changed. In addition, since the bath is not in continuous use, startup time was lengthy. To address these issues, we have replaced the Ametek system with a 3-electrode configuration with a 2.5-liter volume bath. This setup increases lab safety and reduces both hazardous waste production and bulk chemical requirements. It also allows us to easily modify bath composition and temperature or utilize multiple baths.

Now, the solution is contained in a pyrex beaker 10 cm tall and 19 cm in diameter. The beaker sits on a stir/hot plate, which is used to stir the solution and maintain a desirable temperature. In operation, the beaker contains approximately 2 L of 1M cadmium sulfate with 600mg tellurium oxide and sufficient hydrochloric acid to make the pH ~1.8 at $70^0$C. The pH is monitored with a temperature compensated pH electrode, and the working electrode potential is controlled by a potentiostat with a Ag/AgCl reference electrode. A serious of Cd bars and a platinum mesh has been used as counter electrodes.

Deposition from the solution described above at -0.6 V Ag/AgCl resulted in current densities of ~1.8 mA/cm$^2$, and produced CdTe films approximately 3μm thick in 50 minutes. It is speculated that the deposition rate could be further increased by optimizing the solution flow pattern and rate, and possibly further increasing the tellurium concentration. However the achieved deposition rate is much higher than it was in the previous AMETEK system: 3-8 hours to deposit 3 μm film. The system used by British Petroleum before they abandoned CdTe cells grew films even slower.

The achieved higher deposition rate stimulated to continue optimization of ED system and the CdTe film and cell processing. However, we had to stop this work and concentrate our further efforts on development of the GJD system and processing. One of the reasons was that after BP abandoned CdTe cell area, the only US company in the field has become First Solar, LLC, which successfully uses the vapor transport deposition, VTD, technique. Our GJD technique, in principle is similar, to the FS VTD. In both cases the deposited substance is delivered by gas flow to the substrate.

## 6.2. Gas Jet Deposition System and the Cell Fabrication

In our GJD system, cadmium and tellurium vapors are produced by heating a quartz tube containing CdTe chunks to approximately 800 °C. Helium is passed through this tube, carrying the Cd and Te to a heated substrate where it reacts to form a CdTe film. The deposition chamber is pumped with a mechanical pump, and maintains a pressure of approximately 460 mtorr with a 140 sccm helium flow through the CdTe source tube. The substrate is heated with a resistive element, and is kept at a desired temperature which varied in our optimization experiments in the range of 380-450 °C.

Cells were grown on both single and bi-layer TCO/glass substrates. Our first experiments were done with commercial 3 mm thick soda lime glass coated with $SnO_2$:F as single layer substrates. Additional coating at CSM with the undoped $SnO_2$ provided bi-layer substrates. In our recent experiments we have used substrates made on 1 mm thick 7059 glass, with the TCO consisting of 500 nm $SnO_2$:F covered with 100 nm undoped $SnO_2$. Those were supplied by Dr. Dave Albin's group at NREL.

CdS was deposited on the substrates using a chemical bath deposition process. In this process, the substrates are first cleaned by boiling them in a solution of 20 mL Micro-90 detergent in 1200 mL deionized water and rinsing them in 5 changes of boiling deionized water. The cleaned samples were suspended in 1500 mL beaker in a heated ultrasonic bath. The beaker also contains a T-shaped rod connected to an electric motor to provide stirring. A solution of 900 mL deionized water containing 0.265 g cadmium acetate and 1.540 g ammonium acetate was stirred, ultrasonically agitated, and heated to 80 °C. When the solution reached 80 °C, 0.380 g thiourea dissolved in 100 mL deionized water and then 30 mL 29% ammonium hydroxide were added. This solution was stirred and ultrasonically agitated at 80 °C for 1 hour, after which the samples were removed and ultrasonically agitated in 80 °C water for 10 minutes. The process was then repeated, yielding CdS films usually 325 nm thick.

The CdS films were exposed to a 1 M $CdCl_2$ mist for 45 s, and then placed in a 450 °C tube furnace. The tube furnace has a volume of approximately 9.3 L and was purged with nitrogen flowing at 71 standard liters per hour. The furnace temperature was maintained at 450 °C for 50 minutes, and then allowed to cool to room temperature overnight with the nitrogen still flowing. Typically, the furnace takes 3 hours to cool from 450 °C to 100 °C. The samples were removed from the furnace the next morning, rinsed in boiling deionized water, and stored in a desiccator.

CdTe films were deposited on the CdS substrates using the GJD system. A plot of the process temperatures as a function of time for a typical growth is shown in Fig. 6.1. It should be noted that the temperature values in the figure are the thermocouple readings that can considerably differ from the real temperature. After loading the substrate, the chamber was evacuated, and the helium carrier gas was started flowing through the source tube. After the chamber pressure reached a steady state, the substrate heater was turned on (A) and allowed to reach approximately 400 °C at its surface. This takes approximately 25 minutes. Then the frit heater is turned on (B) and allowed to warm up for 10 minutes. Radiation and conduction from the frit heater cause both the substrate and source to warm slightly. The source heater is then turned on (C) and allowed to warm to ~700 C and dwell there for 10 minutes. Radiation from the source heater warms the sample holder to approximately 435 °C. The shutter is then opened (D), which allows CdTe deposition and warms the substrate holder to approximately 455 °C. For the T-t profile shown in Fig. 6.1, the deposition proceeded for 20 minutes and then the shutter was

closed and the source and substrate heaters were turned off (E). The frit heater was allowed to run another 10 minutes before it was turned off (F), in an effort to prevent the frit from being clogged with CdTe. The source tube and sample holder were allowed to cool to 50 °C before the chamber was opened for sample removal.
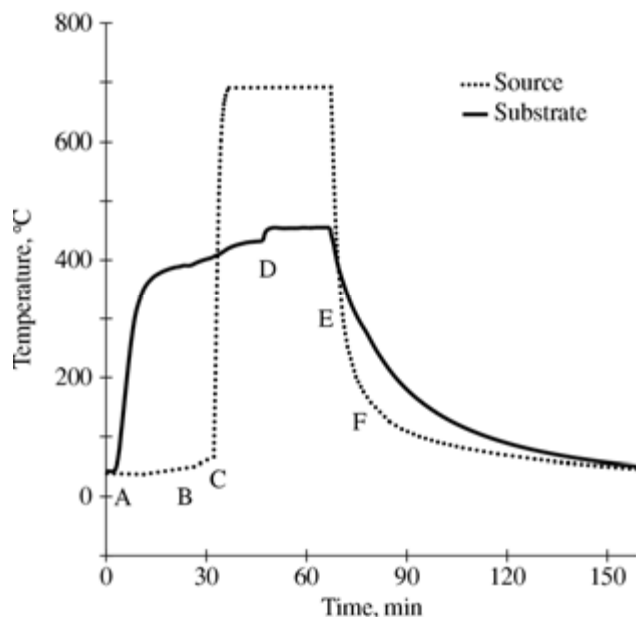


**Figure 6.1.** Nominal temperatures of a source and substrate versus time for a typical growth process

Deposited CdTe/CdS films were annealed placed in a graphite tray and covered with 1 mm glass source plates that had been exposed to a 1 M CdCl$_2$ mist for 2 minutes. The separation between the samples and the source plates was approximately 2 mm. The sample tray was placed in a 390 °C tube furnace with a 9.3 L internal volume that was purged with dry air at a rate of 71 standard liters per hour. The furnace temperature was maintained at 390 °C for 20 minutes, and then allowed to cool to room temperature overnight with the dry air purge running.

The annealed samples were rinsed in boiling deionized water for 1 minute and blown dry in preparation for making the back contacts. The samples were etched with 0.04 M bromine in methanol for 10 s, rinsed in methanol for 1 minute, and blown dry. The etched samples were immediately placed in a vacuum evaporator (approximately 5 minutes in atmosphere after the etch), in which were deposited 0.7 nm of copper followed by 50 nm of ZnTe. The ZnTe:Cu coated samples were annealed in a 9.3 L tube furnace. The samples were loaded into the furnace at room temperature, and it was purged with nitrogen at 142 standard liters per hour for 20 minutes. The purge was then reduced to 71 standard liters per minute, and the temperature was ramped to 200 °C in 15 minutes. The furnace was then turned off, and the temperature allowed to drop to 100 °C over 2 hours. The annealed samples were placed in a vacuum chamber and an array of gold dots 0.32 cm in diameter and 250 nm thick were deposited on them through a shadow mask.

The CdTe and CdS in a 5 mm strip along the perimeter of the samples was removed with a razor blade, and indium was applied to the exposed TCO with an ultrasonic soldering iron to form the front contact.

With the specifications described above or with some modifications numerous cell were grown, mostly on soda-lime-glass/SnO$_2$ substrates with highest efficiency of ~10%. However, combinations of processing parameters are still far from optimum. The ongoing experiments indicate that there is a room for a significant improvement of a cell performance.

## 6.3  Characteristics of Recently Fabricated GJD Cells

Here we present some results obtained on the cells grown recently with some modifications of processing procedure on different glass/TCO substrates.

Cells were grown on 1.5"x1.5" substrates consisting of either a commercial 3mm thick soda lime glass with a single layer of tin-oxide TCO or 1mm thick borosilicate glass (Corning 7059) with either a NREL produced single layer or bi-layer (500 nm F-doped/100 nm undoped) tin oxide TCO. The cell preparation process consisted of the following six steps:

- CDB CdS deposition with three 35 minute cycles of heated and agitated solution consisting of ammonium acetate, cadmium acetate, ammonium hydroxide, and thiourea.
- Gas Jet deposition with the CdTe chunk source temperature at 700$^o$C and the nominal substrate temperature at 380$^o$C.
- One or more CdCl$_2$ ultrasonic nebulizer mist treatments onto a warmed substrate (125$^o$C) followed by a 35 minute anneal at 410$^o$C.
- The CdTe top surface etch of 10 seconds in a 0.02 M bromine methanol solution
- Immediately following the etch, a thermal evaporation of 10 Å of Cu followed by 500 Å of ZnTe with a final anneal of 20 minutes above 180$^o$C (maximum temperature ~190$^o$C).
Thermal evaporation of 0.079cm$^2$ gold dot back contacts, approximately 50 per substrate.

The first three batches of cells whose characteristics are shown were subjected to a single two minute exposure to CdCl$_2$ mist. The fourth batch, as indicated in Fig.6.2, was exposed eight times, 16 minutes total. Histograms in Fig.6.2a demonstrate distribution of about 50 cells on each substrate over cell efficiencies. Efficiency is the highest (up to 12.4%) for the cells of the 4$^{th}$ batch (1mm borosilicate glass, 16 min CdCl$_2$). Most of cells demonstrate η□11%. The average efficiency of the batch 3cells grown on the same kind of bi-layer substrate, but with a single 2 min CdCl$_2$, is about 10%. Efficiency decreases as we go to single-layer layer TCO substrates. Decrease is stronger for the commercial 3mm soda lime glass substrate, and some weaker for the NREL 1mm corning glass substrate. Both single-layer batches demonstrate much greater non-uniformity of efficiency over the substrate area than the bi-layer ones.

- When analyzing the Voc, Jsc, FF, Rsc and Rs data, note that the colors of marks for specific batches are different form those for histograms. The highest values of Voc, Jsc and FF are observed for the cells of the 4$^{th}$ batch. Most of these cells have reasonably high Rsc and low Rs values. Single-layer-substrate batches have lower average Rsc and higher average Rs values than the bi-layer-substrate batches, as well as lower average fill factor. The most dramatic effect on cell efficiency is provided by Voc. The lowest efficiency cells of all batches have a very low Voc value. The short circuit current has the narrowest spread of values over the batch (Fig. c).
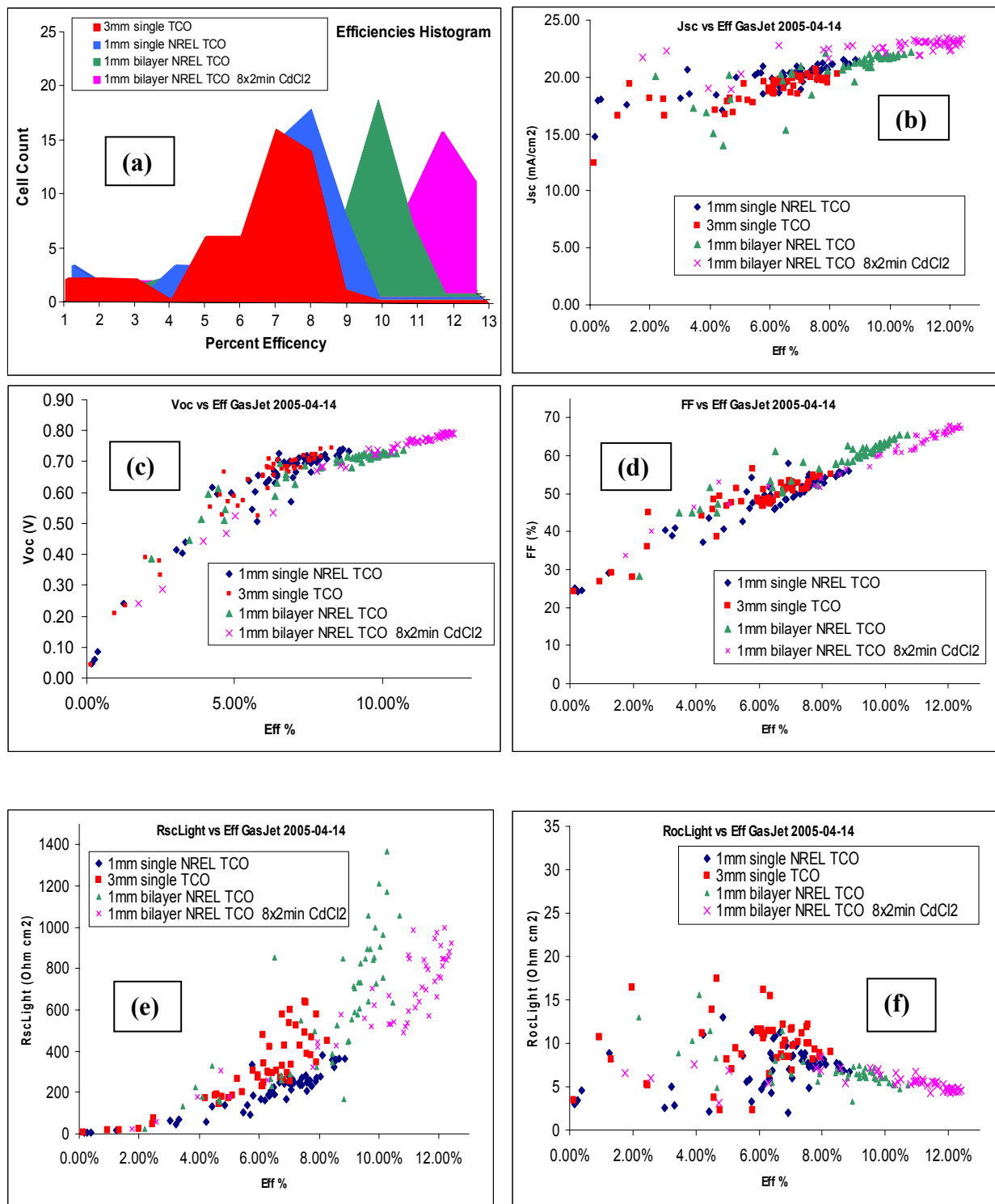
**Figure 6.2** Characteristics of cells grown using GJ-deposition of CdTe on different substrates with different CdCl$_2$ treatments indicated in the figures. (a) Histograms of cell efficiencies. (b), (c), (d), (e), and (f) represent respectively open circuit voltage, short circuit current density, fill factor, "shunt resistance", and "series resistance", versus cell efficiency.

This nonuniformity of the cell parameters over the substrate area correlates with the results of comparative studies of electroluminescence on the single-layer and bi-layer cells (see Sec.1). However those are the non-uniformities in different length scales: tens-hundreds of microns for the EL-detected and millimeters-centimeters for those indicated by Fig. 6.2.

It is clear from the results presented and discussed above that

- Bi-layer substrates are much better than the single-layer ones and with the CdTe GJ deposition technique can provide opportunity cells with efficiency above 12%. By the way, the best CSM ED cell of 12.9% efficiency was grown on bi-layer substrate supplied by the University of South Florida.

- Varying and optimizing $CdCl_2$ treatment may led to higher uniformity of a cell/module parameters hence to higher efficiency [6].

- It is reasonable to expect that further improvement could be reached by optimizing (re-optimizing) not one processing parameter but their combinations. For example, it was shown not once and for different processing technologies that with the bi-layer substrates one can reduce the CdS thickness, hence the Jsc value, without reducing Rsc (shunting) and FF. Since anneal with $CdCl_2$ promotes inter-diffusion and consumption of CdS, we have to adjust to each other and optimize simultaneously thickness of CdS, its postdeposition anneal (with or without $CdCl_2$), and $CdCl_2$ treatment of CdTe/CdS structure.

Some results of our studies, not presented here, have given hints on what processing parameters should be changed/optimized in the first turn. We hope we will have an opportunity to continue and accomplish optimization of processing technology based on GJD.

## 7. SUMMARY

In accordance with our general research approach and specific goals of studies formulated in the Preface, our work upon this project was mostly devoted to making up a deficiency in fundamental knowledge and understanding of some basic issues behind the CdTe/CdS cells performance and stability. Namely, we were focusing on electronic properties of defects that may control the majority carrier concentration, mechanisms of the dopant compensation, recombination processes, distribution of electrostatic potential in a cell, specifics of the electron transport. In particular, we tried to get new information about the grain boundary effect on electrical and optical properties of the cell fine-grain material. To fulfill these tasks we have developed new methods and techniques (or adjusted existing ones) for material characterization as well as modified the approaches to the data analysis and interpretation. The most significant progress in characterization methods was made by developing equipment, measuring procedures, and data analysis for electroluminescence (EL) studies, admittance spectroscopy (AS), capacitance transients (C-Tr) measurements, and also in development of high spatial resolution methods, such as tunneling microscopy (STM) and near field scanning optical microscopy (NSOM). In addition to the development of characterization methods and their application to the defect studying, the Report also presents our activities aimed at development and improvement of the cell processing methods. Main results and accomplishments of our work under this subcontract are summarized below

### Luminescent Studies

- It was found that the spatially resolved measurements of electroluminescence (EL) are easy to perform on CdTe cells at various temperatures ranging from the room temperature to the rather low one (~40 K in our measurements). With a quite available instrumentation, the EL pattern could be resolved on the length scales from several microns to centimeters. Usually EL measurements demanded small current densities of the order of $10^1$ mA/cm$^2$, or even below this, which excluded the cell damaging in the process of measurements.

- EL mean intensity and pattern (bright spots on dark background) vary significantly depending on processing technology variations and cell stress conditions and duration. High sensitivity of EL to the cell degradation makes EL measurements an attractive method for early predictions of the cell/module lifetime.

- Simultaneous measurements of spatially resolved EL and PL from the same cell area allows to separate nonuniformities in carrier transport and in recombination rate as sources of nonuniformity in EL.

- EL measurements have shown that nonuniformity in electron transport are effected by both back and front contacts. Buffer layer between the TCO and CDS significantly reduces the nonuniformity.

- Patterned doping with Cu and patterned CdCl$_2$ treatment proposed and applied in this project demonstrated possibility to reveal nonuniformity in defect distribution. The Cu-related defect signatures in the EL spectra were used to detect these defects; spatial distribution of the defects was studied with the EL scans. A significant influence of CdCl2 was demonstrated on accommodation and manifestation of Cu atoms.

- EL studies have provided and independent evidence of photoconductivity in the CdS layer and revealed long-lasting (hours-days) effect of exposure to laser irradiation with the photon

energy above the CdS bandgap. This provides new options for investigations of the CdS photoconductivity mechanisms, in particular, for identification of defects responsible for the photoeffect, their generation, transformation and migration under illumination.

*Admittance spectroscopy (AS) and capacitance transient (C-Tr) measurements*
- A traditional AS and modified AS were used for detection and studying characteristics of deep electronic states in the absorber CdTe layer. It was found that characteristic time, concentration of this states, distribution over CdTe thickness and over energy depend on deposition technique, postdeposition treatment, and contacting procedure.
- An important result of these studies was a high trap concentration found in cells fabricated at various facilities (FS, NREL, UT, FS/CSM), which exceeded doping level, $N_{C-V}$, determined by C-V profiling. In some cells density of detected trap states was of the order of $10^{16}$ cm$^3$. Experimental data also indicated presence of significant amount of slower traps not detectable with the standard AS equipment.
- The common AS measurement procedures and approaches to the data analysis were revised based on published theory and our own experience of the AS studies on CdTe cells. The common approach used for determining trap characteristics from the AS results is valid only for low trap concentration, much smaller than the doping level ($N_t \ll N$). For CdTe (high trap density) common approach underestimates trap concentration. Our numerical modeling evaluated a correction factor that should be used to make estimates more accurate. The magnitude of this factor is especially high if the traps levels are located close to Fermi level (like for Cu$_{Cd}$ defects in CdTe). On the other hand, the doping level derived from C-V profiling, $N_{C-V}$, can be strongly overestimated if $N_t > N$, which was proved with numerical modeling of apparent doping level, $N_{C-V}$, compared to the real one, $N$, for two trap levels with characteristics close to those determined by AS.
- The technical limitations on the AS method were discussed. Specifically, the characteristic time of traps available for detection with usual LCR meters was considered. As possible solutions to the problem, variation of temperature (though also limited) and measurements of transients (for very slow traps) were discussed.
- The problem of determining trap cross section was analyzed for the case of repulsing potential barrier provided by the collective action of closely spaced traps at the grain boundaries. The latter are considered the most important origin of very slow traps. The trap filling dependence on time is specific for this "collective" trap action, which can be used for the GB states identification.
- The current state of the transient studies in CdTe is unsatisfactory. Studying of capacitance transients (C-Tr) is the most promising method for detection slow/deep states, estimating trap concentration, distinguishing between the majority- and minority-carrier traps. This report contains numerous results of the C-Tr studies in CdTe cells.
- A new measurement system was developed and used for studying the cell admittance, in particular, C-f and C-V dependencies, along with transients in a temperature range from -190$^o$C to +85$^o$C. Measurements can be conducted in dark and under illumination of varying intensity and spectrum. Transients were induced by bias pulses of different polarity and duration, as well as by light pulses of different photon energies, including those lower than the CdTe bandgap.
- Combined AS and C-Tr measurements with this new system were used to study effects of Cu doping and CdCl$_2$ treatment on trap states in CdTe cells. Activation energies and apparent

capture cross sections (trap signatures) were determined for at least five hole traps and two traps for minority carrier electrons. Concentrations of the traps and their changes after stress varied significantly for different combinations of Cu (yes, no) and $CdCl_2$ (yes, no) treatments.

- Some of the traps were attributed to specific defects, such as $V_{Cd}$, ($V_{Cd}$-$Cl_{Te}$) A-centers, $Cu_{Cd}$, $Te_i$. The latter trap with Ea $\approx 0.47$ eV was observed only in cells subjected to NP etch that provided free Te layer on the top of CdTe and excess Te underneath. A deep trap with $E_a \approx 0.8$ eV and concentration exceeding $10^{15}$ $cm^{-3}$ was found only in cells with combined Cu and $CdCl_2$ treatment. It could be suggested that this trap is related to some complex involving Cu an Cl.

## *High spatially resolved measurements*

- A novel technique, charge injection spectroscopy (CIS) with a scanning tunneling microscope (STM) was used to map carrier transport across the interface between CdTe and ZnTe:Cu back contact. The lateral resolution below 20 nm was demonstrated.
- Charge transfer between CdTe and ZnTe was highly non-uniform. A majority of the current flows along the pathways usually localized at grain boundaries. The grain bulk regions show rather uniform, low current, indicating substantially more resistive back contact. However, conducting paths were also found within some grains suggesting that specific intragrain defects also may reduce back contact resistance.
- Near field scanning optical microscopy (NSOM) was used for mapping lateral distribution of photocurrent collection. These measurement were done on CdTe cells of substrate configuration supplied by the University of Toledo. This configuration provided an access of the optical tip to the TCO surface making possible near field measurements. Spatial resolution was better than 100 nm.
- The photocurrent images combined with the topography ones demonstrated unambiguously enhanced current collection from the grain boundaries as compared to the intragrain regions. A similar effect was observed at the CIGS/CdS cells (NREL) of high efficiency.
- In addition to photocurrent mode of NSOM, the photoluminescence mode was developed in this project. First NSOM PL images, both plan-view (UT cells) and cross sectional (CSM cells) confirmed possibility to study nonuniform distribution of the PL intensity on the subgrain size scale. The contrast between the intergrain and intragrain regions varied with the bias application providing the opportunity to control the sensitivity of measurements to spatial variations in recombination rate.

## *Cell processing*

- A new gas jet deposition system (GJD) for the CdTe deposition was developed where the deposited substance or its components are delivered by gas flow to the substrate. The mthod is similar to the VTD used by First Solar, LLC.
- The deposition rate controlled by the source and substrate temperatures reaches 20 μm/min, although in our studies we used more moderate rates of ~4-5 μm/min.
- The studies aimed at optimization of processing procedure are far for completion. The best cells grown on bi-layer substrates with the CBD CdS, GBD CdTe and ZnTe:Cu/Au back contact demonstrated efficiencies of ~12.5%. However recent experiments showed that there is a room for significant further improvement. As more promising directions of studies we see combined optimization of $CdCl_2$ treatment, postdeposition treatment and thinning of CdS, and optimization of the back contact structure, in particular, thickness of ZnTe and content of Cu in it.

## 8. REFERENCES

1. S. Feldman, S. Townsend, R.T. Collins, V. Kaydanov, and T.R. Ohno. "Electroluminescence and Photoluminescence of Stressed and Unstressed CdTe/CdS Cells", *Proceedings of the NCPV Program Review Meeting*, September, 2001, Lakewood, CO.

2. W. Li, M. Ritala, M. Leskela, L. Niinisto, E. Spoinen, S. Sun, W. Tong, and C. J. Summers. "Photo- and electroluminescence of SrS:Cu and SrS:Ag,Cu,Ga thin films," *J. Appl. Phys*, **86** , 5017 (1999).

3. H. Song, X. Bao, N. Li, and J. Zhang, "Relation between electroluminescence and photoluminescence of $Si^+$-implanted $SiO_2$", *J. Appl. Phys.*, **82**, 4028 (1997).

4. M.V. Artemyev, V. Sperling, and U. Woggon,  "Electroluminescence in thin solid films of closely packed CdS nanocrystals" *Appl. Phys.*, **81**, 6975 (1997).

5. N. L. Rowell, J.-P. Noel, S. C. Houghton, and M. Buchanan, "Electroluminescence and photoluminescence from $Si_{1-x}Ge_x$ alloys", *Appl. Phys. Letters*, **58**, 957  (1991).

6. V.G. Karpov, G. Rich, A.V. Subashiev, and G. Dorer, "Shunt Screening and size dependent effects in thin-film photovoltaics", *J. Appl. Phys*. **89**, 4975 (2001); V.G. Karpov, A.D. Compaan and Diana Shvydka, "Effects of nonuniformities in thin-film photovoltaics", *Appl. Phys. Lett* .**80**, 4256 (2002); V.G. Karpov, A.D. Compaan and Diana Shvydka, "Micrononuniformity effects in thin-film photovoltaics", Proc. *The $29^{th}$ IEEE PVSC Conf*., New Orleans, July 2002, p.708-711; V.G. Karpov, Diana Shvydka and A.D. Compaan "Nonuniformity Modeling and Taming", in *National CdTe R&D Team Meeting Minutes*, Golden, CO, July 10-11, 2003.

7. M. J. Romero, D. S. Albin, M. M. Al-Jassim, X. Wu, H. R. Moutinho, and R. G. Dhere, "Cathodoluminescence of Cu diffusion in CdTe thin films for CdTe/CdS solar cells", *Appl. Phys. Letters*, **81**, 2962 (2002).

8. S. A. Galloway, P. R. Edwards and K. Durose, "EBIC and cathodoluminescence studies of grain boundaries and interface phenomena in CdTe/CdS solar cells", *Inst. Phys. Conf. Ser.*, **157**, 579 (1997).

9. R. Harju, V. G. Karpov, D. Grecu, and G. Dorer, "Electron-beam induced degradation in CdTe photovoltaics", *J. Appl. Phys.*, **88**, 1794 (2000).

10. J. Hiltner, "Investigation of Spatial Variations in Collection Efficiency of Solar Cells". (*Ph.D. thesis*, Colorado State University, Fort Collins, CO), 2001.

11. M. K. Herndon, A. Gupta, V. Kaydanov, and R. T. Collins, "Evidence for the grain-boundary-assisted diffusion in polycrystalline CdS/CdTe heterojunctions", *Appl. Phys. Letters*, **75**, 3503 (1999).

12. D. Shvydka, A. D. Compaan, and V. G. Karpov, "Nonlocal response in CdTe photovoltaics", *J. Appl. Phys.*, **91**, 9059 (2002).

13. M. David, "Geostatistical Ore Reserve Estimation", Elsevier Scientific Publishing Co., Amsterdam, 1977, pp. 73-90.

14. A. S. Gilmore, V. Kaydanov, T. R. Ohno, D. Rose, S. D. Feldman, P. Erslev, "Treatment Effects on Deep Levels in CdTe Based Solar cells", *Proceedings of the 29th IEEE PV SC*, May, 2002, New Orleans, LA., p. 604.

15. A.D. Compaan, D. Shvydka, K.J Price, A. Vasko, and V.G. Karpov, "Bias-Dependent Luminescence in CdS/CdTe Cells", *Proceedings of the NCPV Program Review Meeting*, September, 2001, Lakewood, CO, pp.197-198.

16. J. Tang, D. Mao, T. R. Ohno, V. Kaydanov, and J. U. Trefney, "Properties of ZnTe:Cu Thin Films and CdS/CdTe/ZnTe Solar Cells", *Proceedings of the 26th IEEE PV Specialists Conference*, October, 1997,Anaheim, CA, pp. 439-442.

17. Software provided by Diana Svydka, University of Toledo

18. A.S. Jordan and J.M. Ralston, "A diffusion model for GaP red LED degradation", *J. Appl. Phys.* **47**, No.10, pp.4518-4527.

19. T.A. Gessert, M.J. Romero, R.G. Dhere, and S.E. Asher, *Mat. Res. Soc. Symp. Proc*. **763**, 2003, p. B3.4.1.

20. Su-Huai Wei and S.B. Zang, "Chemical trends of defect formation and doping limit    in    II-VI semiconductors: The case of CdTe", *Phys. Rev. B,* **66**, 2002, p.155211.

21. Kenneth Zanio, "Semiconductors and Semimetals, Volume 13, Cadmium Telluride", *Academic Press, New York, San Francisco, London*, Copyright © 1978, p.148

22. D.M. Hofman, P. Omling, and H.G. Grimmeiss, "Identification of the chlorine A    center in CdTe", *Phys. Rev. B*, **45**, 1992, pp.6247-6250.

23. D. Grecu and A. D. Compaan, "Photoluminescence study of Cu diffusion and electromigration in CdTe", *Appl. Phys. Lett*. **75**, 361 (1999); D. Grecu, A. D. Compaan, D. Young, U. Jayamaha and D. H. Rose, "Photoluminescence of Cu-doped CdTe and related stability issues in CdS/CdTe solar cells", *J. Appl. Phys.* **88**, 2490 (2000).

24. S. D. Feldman, R. T. Collins, V. Kaydanov, and T. R. Ohno, "Effects of Cu in CdS/CdTe solar cells studied with patterned doping and spatially resolved luminescence", *Appl. Phys. Lett.* **85**, 2004, pp. 1529-1531.

25. P.R. Thornton, "The Physics of Electroluminescent Devices*" E. & F. N. Spon Limited, London*, 1967,  p. 18.

26. P. Sutter, E. Sutter, and T.R. Ohno, "High-resolution mapping of nonuniform carrier transport at contacts to polycrystalline CdTe/CdS solar cells," *Appl. Phys. Lett.* **84**, No. 12, 2004, pp. 2100-2102.

27. Iris Visoly-Fisher, Sidney R. Cohen, and David Cahen, "Direct evidence for grain-boundary depletion in polycrystalline CdTe from nanoscale-resolved measurements, "*Appl. Phys. Lett.* **82**, No. 4, 2003, pp. 556-558.

28. S. Smith, P. Zhang, T. Gessert, and A. Mascarenhas, "Near-field optical beam-induced currents in CdTe/CdS solar cells: Direct measurement of enhanced photoresponse at grain boundaries," *Appl. Phys. Lett.* **85**, No. 17, 2004, pp. 3854-3856.

29. A. Castaldinin, A Cavallini, and B. Fabroni, "Comparison of electrical and luminescent data for the A center in CdTe," *App. Phys. Lett.* **69**, 1996, pp. 3510-3512.

30  Uwe Rau and Marion Schmidt, "Electronic properties of ZnO/CdS/Cu(In,Ga)Se$_2$ solar cells – aspects of heterojunctions formation", *Thin Solid Films*, **387**, 2001, pp. 141-146.

31. V. G. Karpov, G. Rich, A. V. Subashiev, G. Dorer, "Shunt screening, size effects and I /V analysis in thin-film photovoltaics", *J. Appl. Phys.* **89**, 2001, pp. 4975-4978.

32. D. H. Rose, F. S. Hasoon, R. G. Dhere, D. S. Albin, R. M. Ribelin, X. S. Li, Y. Mahathongdy, T.A. Gessert, and P. Sheldon "Fabrication Procedures and Process Sensitivities for CdS/CdTe Solar Cells", Progr. Photov. Res. Appl. 7, 1999, pp. 331-340.

33. James M. Kestner, Sarah McElvain, Colin A. Wolden, Stephen Kelly, Tim R. Ohno, Lawrence M. Woods, and Rosine Ribelin, "Vapor Transport Deposition and Characterization of Polycrystalline CdTe Solar Absorbers", *Mat. Res. Soc. Symp. Proc.* **763**, 2003, p. B5.22.1.

34. James M. Kestner, Development and Analysis of Vapor Transport Deposition of Cadmium Telluride Thin Films (Ph.D. thesis, Colorado School of Mines, Golden, CO 2003)

35. Iris Visoly-Fisher, Sidney R. Cohen, David Cahen, and Christos S. Ferekides, "Electronically active layers and interfaces in polycrystalline devices: Cross-section mapping of CdS/CdTe solar cells", *Appl. Phys. Lett.* **83**, 2003, pp. 4924-4926.

36. T.A. Gessert, M.J. Romero, S. Johnston, B. Keyes, and P. Dippo, "Spectroscopic Cathodoluminescence Studies of the ZnTe:Cu Contact Process for CdS/CdTe Solar Cells," *Proceedings of the 29th IEEE PVSC*, 2002, New Orleans, LA, pp. 535-538.

37. S. D. Feldman, L. Mansfield, T. R. Ohno, V. Kaydanov, J. D. Beach, and T. Nagle, "Non-uniformity mitigation in CdTe Solar cells: the effects of high-resistance transparent conducting oxide buffer layers," *Proceedings of the 31st IEEE PV Specialists Conference*, January, 2005, Walt Disney World, FL.

38. Hegedus, D. Ryan, K. Dobson, B. McCandless, and D. Desai, "Photoconductive CdS: How Does It Affect CdTe/CdS Solar Cell Performance?" *Mat. Res. Soc. Symp. Proc.* **763,** 2003, p. B9.5.

39. M. Gloeckler and J.R. Sites, "Quantum Efficiency of CdTe Solar Cells in Forward     Bias," *Proceedings of the 19th European PVSEC*, 2004, p. 4AV.1.45.

40. M. Gloeckler, A.L. Fahrenbruch, and J.R. Sites, "Numerical Modeling of CIGS and CdTe Solar Cells:  Setting the Baseline," *Proc. World Conf. on Photovoltaic Energy Conversion*, Osaka, Japan, 2003, p. 2P-D52.

41. Ben G. Streetman and Sanjay Banerjee, Solid State Electronic Devices, (Prentice Hall, Upper Saddle River, NJ, 2000) p. 524.

42. A.S. Gilmore, V. Kaydanov, T.R. Ohno, and D. Rose, "Admittance Spectroscopy of Deep Levels in CdTe Solar Cells", *NCPV Progr. Rev. Meeting 2001*, Oct. 2001, Laikewood, CO, pp. 199-200.

43 . Nollet, M. Burgelman, S. Degrave, and J.Beier, " Importance of Air Ambient during $CdCl_2$ Treatment of Thin Film CdTe Solar Cells Studied through Temperature Dependent Admittance Spectroscopy", *Proceedings of the $29^{th}$ IEEE PV SC*, May, 2002, New Orleans, LA., pp. 704-707.

44. D. Shvydka, U. Jayamaha, V.G. Karpov, and A.D. Compaan, "Capacitance-Frequency Analysis of CdTe Photovoltaics", *ibid.*, pp. 752-755.

45. A.S. Gilmore, V. Kaydanov, T.R. Ohno, "The Study of Deep Levels in CdS/CdTe Solar Cells Using Admittance Spectroscopy and its Modifications", *MRS Spring 2003*, S. Francisco, CA, April 2003, pp.

46. P. Blood and J.W. Orton, "The Electrical Characterization of Semiconductors: Majotity Carriers and Electron States", ACADEMIC PRESS, *Harcout Brace Jovanovich, Publishers, London - San Diego - New York – Boston – Sydney – Tokio – Toronto*, Copiright ©1992.

47. V. Kaydanov, "Capacitance/Conductance Spectroscopy of Deep States and Hole Concentration in CdTe Solar Cells", in *National CdTe R&D Team Meeting Minutes*", Golden, CO, Oct. 31-Nov. 01, 2002.

48. A. Balcioglu, "Characterization of Deep Impurity Levels in Semiconductor Devices", Ph.D. Thesis, Colorado School of Mines, Golden, CO, 2001.

49. T. Walter, R. Herberholz, C. Muller, and H.W. Schock, "Determination of defect distributions from admittance measurements and application to $Cu(In,Ga)Se_2$ based heterojunctions", *J. Appl. Phys.* **80**, 4411 (1996).

50. C.E. Michelson, A.V. Gelatos, and J.D. Cohen, "Drive-level capacitance profiling: Its application to determining gap state densities in hydrogenated amorphous silicon films", *Appl. Phys. Lett.* **47**, 412 (1985).

51. L.C. Kimmerling, "Influence of deep traps on the measurement of free-carrier distributions in semiconductors by junction capacitance techniques" *J. Appl. Phys.* **45**, 1839 (1974).

52. J.H. Scofield, "Effects of series resistance and inductance on solar cell admittance measurements", *Solar Energy Materials and Solar Cells* **37**, 217 (1955).

53. S. W. Johnston, R.S. Crandall, "Evidence of the Meyer-Neldel Rule in InGaAsN alloys: Consequences for Photovoltaic Materials", *MRS Spring 2003*, S. Francisco, CA, April 2003.

54. R.S. Crandall, *J. Electron. Mat.*, 9, 713 (1980)

55. D.L. Young, K. R. Ramanathan, M. Contreras, J. Abushama, R. S. Crandall, "A Barrier To Trap Filling in $CuIn_{1-x}Ga_x Se_2$", *MRS Spring 2003*, S. Francisco, CA, April 2003.

56. L.M. Woods, D.H. Levi, V. Kaydanov, G.Y. Robinson, and R.K. Ahrenkiel, "Electrical Characterization of CdTe Grain-Boundary Properties from As Processed CdTe/CdS Solar Cells", in *Proc. 2$^{nd}$ World Conf. on PV Solar Energy Conversion*, July 1998, Vienna, Austria, pp. 1043-1046; "Electrical Characterization of Etched Grain-Boundary Properties from As-Processed p-CdTe Based Solar Cells", *Proc. NCPV PV Progr. Rev. Meeting*, Denver, CO 1998, AIP CP462, pp.499-504.

57. A.S. Gilmore, V. Kaydanov, U. Laor, T.R. Ohno, B. McCandless, " AC Characterization of Grain Boundary Electronic Properties in CdTe Thin Films", *Proc. NCPV Progr. Rev. Meeting 2000*, Denver, CO, April 2000, pp.259-260.

58. V.I Kaydanov and T.R. Ohno, "Process Development and Basic Studies of Electrochemically Deposited CdTe-Based Solar Cells", Final Technical Report, 15 May 1988-17August 2001, NREL/SR-520-31777, Colorado School of Mines, March 2002.

59. R.A. Sasala and J.R. Sites, "Transient Voltage of Thin-film Polycrystalline Solar Cells", *AP. Conf. Proc.* 268 , *PV Advanced R&D Project*, Denver, CO, 1992, pp.218-227.

60. R.A. Sasala and J.R. Sites, "Time –Dependent Voltage in $CuInSe_2$ and CdTe Solar Cells", *Proc. 23d IEEE PVSC,* p.543 (1993).

61. T.J. MacMahon, "Dark Curernt Transients in Thin-Film CdTe Solar Cells", *Proceedings of the 29$^{th}$ IEEE PV SC*, May, 2002, New Orleans, LA., pp. 768-771.

62. Brian E. McCandless and James R. Sites, in <u>Handbook of Photovoltaic Science and Engineering,</u> edited by Antonio Luque and Steven Hegedus, John Wiley & Sons Ltd, West Sussex, England, p. 633, (2003).

63. A. Niemegeers, M. Burgelman, "Effects of the Au/CdTe back contact on IV and CV characteristics of Au/CdTe/CdS/TCO solar cells", *Journal of Applied Physics,* **81** No. 6 p2881-2886. (1997).

64. Reuven Chen, "Apparent stretched-exponential luminescence decay in crystalline solids", *Journal of Luminescence*, **102-103**, p. 510-518 (2003).

65. A. Castaldini, A. Calvallini, B. Fraboni, P. Fernandez, J. Piqueras, "Deep energy levels in CdTe and CdZnTe", *Journ. of Appl. Physics,* **83** No 4 p212-2126. (1998).

66. D. Albin, R. Dhere, Z. Wu, T. Gessert, M.J. Romero, Y. Yan, S. Asher, "Perturbation of Copper Substitutional Defect Concentration in CdS/ CdTe Heterojunction Solar Cell Devices", *Proceedings of the Materials Research Society Conference, Symposium F*, (San Francisco, California, USA, April 2002).

67. A. Balcioglu, R. K. Ahrenkiel, F. Hasoon, "Deep-level impurities in CdTe/CdS thin-film solar cells", *J. Appl. Phys.,* **88** No 12 p7175-7178. (2000).

68. M. A. Lorenço, W.L. Ng, K. P. Homewood, K. Durose, "A deep semiconductor defect with continuously variable activation energy and capture cross section", *Appl. Phys. Lett.,* **75** No 2 , pp. 277-279. (1999).

69. P. Emanuelsson, P. Omling, B.K. Meyer, M. Weinecke, M Schenk, "Identification of cadmium vacancy in CdTe by electron paramagnetic resonance", *Physical Review B* **47** 15578 (1993).

70. I. Visoly-Fisher, S.D. Cohen, D. Cahen, "High Resolution Characterization of a Single Grain Boundary in CdTe/CdS Solar Cells", *MRS Spring 2003*, S. Francisco, CA, April 2003.

71. V. Kaydanov, P. Meyers, "Some Possible Effects of Grain Boundaries on Thin Film Cell Performance", in "National CdTe R&D Team Meeting Minutes", Golden, CO, January 2000, Appendix 33.

72. S. Smith, P. Zhang, T. Gessert, and A. Mascarenhas"Near-field optical beam-induced currents in CdTe/CdS soar cells: Direct measurement of enhanced photoresponse at grain boundaries", *Appl. Phys. Lett.*, **85**, No. 17, pp. 3854-3856 (2004).

73. A.A. McDaniel, J.W.P. Hsu, A.M. Gabor, "Near-field scanning opticl microscopy studies of Cu(In,Ga)Se$_2$ solar cells", *Appl.Phys. Lett.* **70**, No. 30, pp. 3555-3557 (1997).

74. W. Song, "Development of High Efficiency Polycrystalline CdTe/CdS Solar Cells Using Electrodeposition", Ph.D. Dissertation, Colorado School of Mines, Golden, Colorado, 1999.

# 9. ACKNOWLEDGEMENTS

## 10.  APPENDICES

### 10.1  Personnel

The names, titles, and representative responsibilities of the individuals contributed to this work are summarized below.

- Timothy R. Ohno, Associate Professor of Physics: Photovoltaic Development, Surface Physics, Electroluminescence, Principal investigator

- Victor I. Kaydanov, Research Professor of Physics: Photovoltaic Development, Electron Transport , Studying of the Defect Electronic States, Principal Investigator

- Reuben T. Collins, Professor of Physics: Electronic and Optical Properties of Semiconductors, NSOM, Photo- and Electroluminescence

- Colin Wolden, Associate Professor of Chemical Engineering: Gas Jet Deposition System Design

- Peter Sutter, Associate Professor: Scanning Tunneling Microscopy and Spectroscopy

- Joe Beach, Post. Doc. Fellow, then Research Professor: Cell Processing and Characterization

- Angelo S. Gilmore, Graduate Research Assistant, then Post. Doc. Fellow: Admittance Spectroscopy, Hall effect

- Scott Feldman, Graduate Research Assistant: Cell Electroluminescence and Photoluminescence, Micro-nonuniformity (Defended Ph.D thesis in May 2005)

- James Kestner, Graduate Research Assistant: Developing of GJD System, Cell Processing      (Defended PhD thesis 2003)

- Fred Seymour, Graduate Research Assistant: Studying of Deep Electronic States by means of Admittance Spectroscopy and Transients; Developing of Database

- Lorelle Mansfield, Graduate Research Assistant: Cell Processing and Characterization, AFM Measurements

- John Yarbrough, Graduate Research Assistant: Near Field Scanning Microscopy

## 10.2 Laboratory Improvements

Principal changes at CSM revolved around both processing and characterization during this project.  As detailed in section 6, the electrodeposition method was modified to increase growth rate, decrease bath size and simplify the tellurium supply.  It was decided midway through to focus on the higher growth rate GJD, which more closely resemble processes in use by our industrial partner First Solar.   The GJD deposition system is described in detail in Reference 34, and was developed initially under subcontract ZAK-8-17619-03, with ITN Energy Systems.

The most significant change in equipment for characterization was the development of the temperature controlled admittance measurement system detailed in section 2.4.  The high temperature stability, as well as high sensitivity afforded by the Agilent LCR meters and Keithley source meter, resulted in the excellent quality data reported in section 2.  A very important part of this system is the flexible software written in Agilent VEE that permits automated data acquisition.

Both the EL and PL measurements were enhanced during the project by acquisition of an Acton 300i spectrometer with a Princeton Instruments Spec-10:100BR Si CCD array detector which allows for simultaneous spatial and spectral resolution of EL or PL performed on the exact same spot of a solar cell. As described in Sections 1 and 5, high-speed parallel detection of spectra and in some cases spatial mapping allowed studies of non-uniformities.  Our EL and PL measurements allow for many degrees of freedom. Spatial and spectral changes in luminescence can be seen due to changes in temperature, electrical bias (for both EL and PL), laser power (for PL), and light bias (for EL). By altering these parameters, we can emphasize the signal from different defects.  The combination of this detection with the Ti-sapphire laser from the previous project provided a powerful tool of EL/PL and NSOM.

High spatial resolution techniques showed two developments during this period.  A variety of spectroscopic and spatial mapping techniques were shown in section 4 using STM. These were used during the first half of the project, until PI Sutter relocated to Brookhaven National Laboratory.  The second more promising technique, NSOM, resulted in two new instruments during this project, funded by NSF projects DMI-0340259 and DMR-0103945 (PI Collins).  The system used for cross sections and PL used an inchworm approach and tuning fork force feedback.

**10.3 Publications**

1. F. Seymour, V. Kaydanov, and T.R. Ohno, "Study of Meyer-Neldel rule behavior detected with slow capacitance transients in CdTe solar cells", *Proc. of MRS Spring Meeting*, March 28-April 1, 2005, S. Francisco, CA.

2. F.H. Seymour, V. Kaydanov, T.R. Ohno, and D. Albin, "Cu and $CdCl_2$ influence on defects detected in CdTe solar cells with admittance spectroscopy", submitted to *Appl. Phys. Lett.*, May 2005.

3. S.D. Feldman, L. Mansfield, T.R. Ohno, V. Kaydanov, J.D. Beach, and T. Nagle, "Non-uniformity mitigation in CdTe solar cells: the effects of high-resistance transparent conducting oxide buffer layers", *Proc. 31$^{st}$ IEEE PVSC Conf.*, January, 2005, Orlando, FL.

4. F. Seymour, V. Kaydanov, T.R. Ohno, "Study of deep electronic states in CdTe solar cells through the detection and DLTS treatment of slow transients", *Ibid*

5. S.D. Feldman, T.R. Ohno, R.T. Collins, and V. Kaydanov, Defect studies in CdTe solar cells using spatially and spectrally resolved electro-optical methods", *Solar Energy Technologies Progr. Review. Meeting*, October 2004, Denver, CO.

6. F. Seymour, V. Kaydanov, T.R. Ohno, "Study of deep electronic states in CdTe solar cells with capacitance transient measurements", *Ibid*

7. T. R. Ohno, S. D. Feldman, F. Seymour, J.D. Beach, L. Mansfield, R. T. Collins, and V. Kaydanov "Defect physics and chemistry in thin film CdTe Solar Cells", *Ibid*

8. J. Yarbrough, R.T. Collins, J. D. Beach, V. Kaydanov, and T.R. Ohno , "Multiple Wavelength Near Field Scanning Optical Microscopy Study of Thin Film Polycrystalline Solar Cells", *Ibid*

9. S.D. Feldman, R.T. Collins, V. Kaydanov, and T.R. Ohno, "Effects of Cu in CdS/CdTe solar cells studied with patterned doping and spatially resolved luminescence", *Appl. Phys. Lett.* **85**, 2004, pp.1529-1531.

10. J. M. Kestner, S. McElvain, S. Kelly, L. M. Woods, T. R. Ohno, and C. A. Wolden, "An Experimental and Modeling Analysis of Vapor Transport Deposition of Cadmium Telluride", *Sol. Energy Mater. Sol. Cells* **83**, 2004, pp. 55-65.

11. P. Sutter, E. Sutter, and T.R. Ohno, "High-resolution mapping of nonuniform carier transport at contacts to polycrystalline CdTe/CdS solar cells", *Appl. Phys. Lett.* **84**, No. 12, 2004, pp.2100-2102.

12. A.S. Gilmore, V. Kaydanov, T.R. Ohno, "The Study of Deep Levels in CdS/CdTe Solar Cells Using Admittance Spectroscopy and its Modifications", *MRS Spring 2003*, S. Francisco, CA, April 2003.

13. P. Sutter, P. Zahl, E. Sutter, V. Kaydanov, T. Ohno, "High-Resolution Electron Structure Mapping on Polycrystalline CdTe Solar Cells by Scanning Tunneling Microscopy", *Ibid*

14. S.D. Feldman, T.R. Ohno, V. Kaydanov, and R.T. Collins, "Development of Electroluminescence Imaging Characterization for CdS/CdTe Solar Cells", *Ibid.*

15. J.M. Kestner, Sarah McElvain, and Colin Wolden, "Vapor Transport Deposition and Characterization of Polycrystalline CdTe Solar Absorbers", *Ibid.*

16. S.D. Feldman, F.H. Seymour, T.R. Ohno, V. Kaydanov, and R.T. Collins, "Development and Application of Electroluminescence Imaging for CdS/CdTe Solar Characterization", *NCPV and Solar Progr. Rev. 2003*, Denver, CO, March 24-26, 2003.

17. J. Kestner, S. McElvain. C.A. Wolden, T. Ohno, and Lawrence Woods, " Temperature Dependence of Growth Rate and Morphology of Vapor Transport Deposited CdTe Thin Films", *Ibid.*

18. S. Gilmore, V. Kaydanov, T. R. Ohno, D. Rose, S. D. Feldman, P. Erslev, "Treatment Effects on Deep Levels in CdTe Based Solar cells", *Proceedings of the 29th IEEE PV SC,* May, 2002, New Orleans, LA., p. 604.

19. A.S Gilmore, A. Al-Kaoud, V. Kaydanov, T.R. Ohno, "Mobility in $SnO_2$:F Thin Polycrystalline Films", *Material. Res. Soc. Symp. Proc. Vol. 668,* San Francisco, CA, April 16-20, 2001, pp. F3.10.1-F3.10.6.

20. A.S. Gilmore, V. Kaydanov, T.R. Ohno, D. Grecu and D. Rose, " Impedance Spectroscopy and Hall Measurements on CdTe Thin Polycrystalline Films", *Material. Res. Soc. Symp. Proc. Vol. 668,* San Francisco, CA, April 16-20, 2001, pp. H5.10.1-H5.10.6

21. S.W. Townsend, T.R. Ohno, V. Kaydanov, A.S. Gilmore, J.D. Beach, "The Influence of Stressing at Different Biases on the Electrical and optical Properties of CdS/CdTe Solar Cells", *Material. Res. Soc. Symp. Proc. Vol. 668,* San Francisco, CA, April 16-20, 2001, pp. H5.11.1-H5.11.6

22. T.R. Ohno, E. Sutter, J. Kestner, A.S. Gilmore, V. Kaydanov, C.A. Wolden, P.V. Meyers, L.Woods, M.J. Romero, M.M. Al-Jassim, S.Johnston, "Microscopic Characterization of Polycrystalline APCVD CdTe Thin Film PV Devices", *Material. Res. Soc. Symp. Proc. Vol. 668,* San Francisco, CA, April 16-20, 2001, pp. H6.5.1-H6.5.6

23. A.S. Gilmore, V. Kaydanov, T.R. Ohno, D. Rose, "Admittance Spectroscopy of Deep Levels in CdTe Solar Cells", *NCPV Progr. Rev. Meeting, 2001*, Oct. 2001, Lakewood CO, pp. 187-188.

24. S. Feldman, S. Townsend, R.T. Collins, V. Kaydanov, and T.R. Ohno, "Electroluminescent and Photoluminescent Studies of Stressed and Unstressed CdTe/CdS cells", *NCPV Progr. Rev. Meeting, 2001*, Oct. 2001, Lakewood CO, pp. 199-200.

## 10.4  Presentations

1.  F.H. Seymour, V.Kaydanov, T.R.Ohno, D. Albin, "Cu and $CdCl_2$ Influence on Deep Defects Detected in CdTe Solar Cells", *National CdTe R&D Meeting*, Golden, May 5-6, 2005, Golden, CO.
2.  S.D. Feldman, "Electroluminescence Studies", *National CdTe R&D Team Meeting*. Perrysburg, OH, Feb. 26-27, 2004. Appendix 6 in "Minutes
3.  S.D. Feldman, "Effects of Cu Studied with Non-Uniform Doping and Spatially Resolved Characterization", *Ibid*. Appendix 13 in "Minutes".
4.  T.R. Ohno,  "Defect Chemistry - What do we know?", *Ibid*. Appendix 10 in "Minutes"
5.  F. Seymour, V. Kaydanov, T.R. Ohno, "Transient Studies in CdTe Solar Cells", *Ibid*. Appendix 15 in "Minutes".
6.  V. Kaydanov, "Capture Cross-Section", *Ibid*. Appendix 16 in "Minutes".
7.  F. Seymour, V. Kaydanov, and T.R. Ohno,"Study of Deep Electronic States in CdTe Solar Cells with Capacitance Transient Measurements", Rocky Mountain Chapter AVS symposium August 12, 2004.
8.  S.D. Feldman, V. Kaydanov, and T.R. Ohno,"Study of Deep Electronic States in CdTe Solar Cells with Capacitance Transient Measurements", Rocky Mountain Chapter AVS symposium August 12, 2004.
9.  S.D. Feldman, ", T.R. Ohno, V. Kaydanov, and R.T. Collins, "Back Contact Nonuniformity Studied with Luminescence Technique",  in *"National CdTe R&D Team Meeting Minutes"*, Golden, CO, July 10-11, 2003. Appendix 6 in "Minutes".
10. S.D. Feldman, T.R. Ohno, V. Kaydanov, R.T. Collins, "Electroluminescence Studies",  in *"National CdTe R&D Team Meeting Minutes"*, Golden, CO, Oct. 31- Nov. 01, 2002. Appendix 8 in "Minutes".
11. V. Kaydanov, "Capacitance/Conductance Spectroscopy of Deep States and Hole Concentration in CdTe Solar Cells", *Ibid*. Appendix 32 in "Minutes".
12. Scott Feldman, "Electroluminescence Studies", *National CdTe R&D Team Meeting*, FSEC, Cocoa, Florida, March 14-15, 2002. Appendix 8 in "Minutes".
13. A. S. Gilmore, "Drive Level Capacitance Profiling", *Ibid.* Appendix 34 in "Minutes".
14. Scott Feldman, "Solar Cells and Grad. School. What is not to Love?" (Invited talk) *Colloquium at Colorado College*, Colorado Springs, January 30, 2002.
15. T.R. Ohno " Photovoltaics ", (Invited talk), *Colloquium at the University of Colorado Denver / Metro State University*, Denver, CO, April 5, 2002.

# REPORT DOCUMENTATION PAGE

| 1. REPORT DATE *(DD-MM-YYYY)*<br>February 2007 | 2. REPORT TYPE<br>Subcontract Report | 3. DATES COVERED *(From - To)*<br>16 October 2001 – 31 August 2005 |
|---|---|---|

| 4. TITLE AND SUBTITLE<br>Studies of Basic Electronic Properties of CdTe-Based Solar Cells and Their Evolution During Processing and Stress: Final Technical Report, 16 October 2001 – 31 August 2005 | 5a. CONTRACT NUMBER<br>DE-AC36-99-GO10337 |
|---|---|
| | 5b. GRANT NUMBER |
| | 5c. PROGRAM ELEMENT NUMBER |
| 6. AUTHOR(S)<br>V.I. Kaydanov and T.R. Ohno | 5d. PROJECT NUMBER<br>NREL/SR-520-41129 |
| | 5e. TASK NUMBER<br>PVB75201 |
| | 5f. WORK UNIT NUMBER |

| 7. PERFORMING ORGANIZATION NAME(S) AND ADDRESS(ES)<br>Physics Department<br>Colorado School of Mines<br>Golden, Colorado 80401 | 8. PERFORMING ORGANIZATION REPORT NUMBER<br>ADJ-2-30630-05 |
|---|---|

| 9. SPONSORING/MONITORING AGENCY NAME(S) AND ADDRESS(ES)<br>National Renewable Energy Laboratory<br>1617 Cole Blvd.<br>Golden, CO 80401-3393 | 10. SPONSOR/MONITOR'S ACRONYM(S)<br>NREL |
|---|---|
| | 11. SPONSORING/MONITORING AGENCY REPORT NUMBER<br>NREL/SR-520-41129 |

**12. DISTRIBUTION AVAILABILITY STATEMENT**
National Technical Information Service
U.S. Department of Commerce
5285 Port Royal Road
Springfield, VA 22161

**13. SUPPLEMENTARY NOTES**
NREL Technical Monitor: Harin S. Ullal

**14. ABSTRACT** *(Maximum 200 Words)*
This report describes basic issues behind CdTe/CdS cell performance and stability, such as the nature and electronic properties of impurities and defects that control the majority carrier concentration, mechanisms of dopant compensation, recombination processes, their nature and properties, migration and transformation of defects under various processing, stress, and operating conditions. We believe that a better basic understanding of the specific influence of grain boundaries, especially for fine-grain materials such as those making up CdTe-based cells, is now one of the most important issues we must address. We need to clarify the role of grain boundaries in forming the film electronic properties, as well as those of the p-n junction. This report presents studies relevant to the problems mentioned above that were carried out at Colorado School of Mines during this Thin Film PV Partnership subcontract.

**15. SUBJECT TERMS**
Grain boundaries; electroluminescence; photoluminescence; charge injection spectroscopy; scanning tunneling microscopy; electrodeposition; admittance spectroscopy; capacitance transients; deep electronic states; chemical-bath deposition; post-deposition annealing; gas-transport deposition; Gas-Jet system; optimization;

| 16. SECURITY CLASSIFICATION OF: | | | 17. LIMITATION OF ABSTRACT | 18. NUMBER OF PAGES | 19a. NAME OF RESPONSIBLE PERSON |
|---|---|---|---|---|---|
| a. REPORT<br>Unclassified | b. ABSTRACT<br>Unclassified | c. THIS PAGE<br>Unclassified | UL | | 19b. TELEPHONE NUMBER *(Include area code)* |

F1146-E(12/2004)